

FLUID-STRUCTURE IMPACT MODELING AND RISK ASSESSMENT

By

Kenneth Ned Mitchell

Dissertation

Submitted to the Faculty of the

Graduate School of Vanderbilt University

in partial fulfillment of the requirements for

the degree of

DOCTOR OF PHILOSOPHY

in

Civil Engineering

August, 2009

Nashville, Tennessee

Approved:

Professor Sankaran Mahadevan

Professor Eric. J. Barth

Professor P. K. Basu

Professor Carol A. Rubin

To my wife, Mary Beth,

and

To my parents

ACKNOWLEDGEMENTS

Completion of this dissertation would not have been possible without the guidance and encouragement of my advisor, Dr. Sankaran Mahadevan. His mentoring, instruction, and patience have all been critical, and I am grateful for the many opportunities my education has presented me. This work was originally funded through the NASA Graduate Student Researchers Program (GSRP) at the Marshall Space Flight Center (MSFC) in Huntsville, Alabama. The project manager was Dr. John Townsend. I am particularly grateful for the assistance and guidance received from Mr. Jeff Peck of MSFC.

Support for this research was also received from the National Science Foundation's Integrated Graduate Engineering Research and Training (IGERT) program. I am grateful for the collaboration, friendship, and encouragement received from other IGERT students, especially Ramesh Rebba, Candice Griffith, Natasha Smith, Robert Guratzsch, Audrey Copeland, Marcus Knight, and John McFarland. I would also like to thank Ms. Mary Jean Morris, Mr. John Fellenstein, Dr. John Veillette, and Ms. Jennifer Rakes for their assistance with securing laboratory space and experimental equipment. Dr. Eric Barth provided crucial assistance with design of the circuitry components needed for data acquisition.

I would like to thank the Coastal and Hydraulics Laboratory at the U.S. Army Engineer Research and Development Center in Vicksburg, Miss. for giving me invaluable experience as an engineering researcher, and an outstanding start to my professional career. I am especially thankful for the support and encouragement that I have received from Dr. Rose Kress, Dr. Nick Kraus, and (soon-to-be Dr.) Edmond Russo. Also, Ms. Holly Messing and Ms. Brittany Kolb provided excellent assistance with formatting and editing of the final dissertation draft.

TABLE OF CONTENTS

	Page
DEDICATION	ii
ACKNOWLEDGEMENTS	iii
LIST OF TABLES	vii
LIST OF FIGURES	viii
Chapter	
I. INTRODUCTION	1
1.1 Overview	1
1.2 SRB Problem Background	4
1.3 Research Objectives and Scope	7
II. FLUID-STRUCTURE IMPACT MODELING AND SOLID ROCKET BOOSTER SPLASHDOWN	10
2.1 Introduction	10
2.2 Fluid-Structure Impact Modeling	11
2.2.1 Early Approaches	11
2.2.2 Potential Flow Theory	15
2.3 Commercial Finite Element Codes	19
2.3.1 MSC.Dytran	21
2.3.2 LS-Dyna	22
2.4 Modeling of Solid Rocket Booster Splashdown	24
2.4.1 SRB Rigid-Body Model	25
2.4.2 SRB Stress Prediction Model	32
2.4.3 Risk Assessment of SRB Splashdown	34
2.4.4 SRB Risk Assessment Challenges	37
2.5 Concluding remarks	38
III. MODEL ERROR QUANTIFICATION FOR FLUID-STRUCTURE IMPACT ANALYSIS	40
3.1 Introduction	40
3.2 Discretization Error Quantification	42
3.3 LS-Dyna Fluid-Structure Impact Methodology	46
3.3.1 Independent Mesh Refinement	47
3.3.2 Richardson Extrapolation Implementation	49
3.3.3 Finding an Error Estimator	51

3.4 Summary and Conclusions	59
IV. EXPERIMENTAL VALIDATION OF FLUID-STRUCTURE IMPACT MODEL	62
4.1 Introduction.....	62
4.2 Experimental Setup.....	63
4.2.1 Aluminum Cylinder	63
4.2.2 Drop Mechanism.....	65
4.2.3 Water Tank.....	68
4.2.4 Determination of Impact Velocities.....	69
4.3 Data Acquisition System.....	72
4.3.1 Measuring Deformation Strain	73
4.3.2 Strain Gages Used for Stress Analysis.....	74
4.3.3 Multi-Channel Dynamic Strain Measurement	79
4.3.4 Measurement Software and Signal Processing.....	82
4.3.5 Experimental Uncertainty	87
4.3.6 Tuning Parameters	89
4.4 Qualitative Cylinder Model Validation	90
4.5 Quantitative Validation Under Uncertainty	98
4.5.1 Classical Hypothesis Testing	100
4.5.2 Bayesian Hypothesis Testing.....	105
4.6 Summary and Conclusions	110
V. SRB SPLASHDOWN FAILURE ANALYSIS	114
5.1 Introduction.....	114
5.2 Buckling Overview and Background.....	117
5.2.1 Buckling Theories and Experiments.....	118
5.2.2 SRB Splashdown Buckling.....	124
5.3 Fundamental Shell Buckling Equations.....	126
5.3.1 von Karman Plate Equilibrium Equations	130
5.3.2 Donnell Equilibrium Conditions for Cylinders.....	131
5.4 Numerical Buckling Analysis.....	131
5.4.1 Quasi-Static Cylinder Example.....	133
5.4.2 SRB Forward Skirt Buckling.....	137
5.4.3 SRB Risk Assessment.....	151
5.5 Summary and Conclusions	155
VI. VALIDATION INFERENCE EXTRAPOLATION TO SRB PROBLEM.....	157
6.1 Background and Overview	157
6.2 Bayesian Network Methodology	159
6.3 Confidence Extrapolation for Experimental Cylinder and SRB Problem.....	162

6.3.1 Experimental Cylinder: Measured Quantity to Unmeasured Quantity	163
6.3.2 Experimental Cylinder: Gaged Location to Non-Gaged Location.....	166
6.3.3 Extrapolation to SRB Splashdown.....	168
6.4 Summary and Conclusions	177
VII. CONCLUSIONS AND FUTURE WORK.....	179
7.1 Overview.....	179
7.2 Future Work	182

LIST OF TABLES

Table	Page
3.1 Mesh details for hinged cylinder discretization exercise.....	50
4.1 Rotational impact velocities of cylinder from high-speed camera tests	72
4.2 Peak von Mises stress (psi) results from 10 cylinder drop tests	100
4.3 Sample statistics and LS-Dyna peak stress prediction for multiple locations	101
4.4 95% confidence bounds for mean peak stress based on experimental results.....	102
4.5 Peak von Mises stress measurements for five drop tests at four new locations	103
4.6 Observed sample and model prediction statistical parameters	104
4.7 Model validation via classical tests for mean and variance.....	104
4.8 Model validation metric, B and confidence, C	109
5.1 Sensitivity of SRB p_f to horizontal velocity at splashdown.....	154
6.1 Results of BN simulation for unmeasured quantity, t_{max}	166
6.2 Results of BN simulation for non-gaged location.....	168
6.3 Potential dimensional matrix for cylinder impact problem	170
6.4 Null set vectors for potential cylinder impact formulation.....	171
6.5 Scaling ratios between SRB and experimental cylinder	173

LIST OF FIGURES

Figure	Page
1.1	Diagram of SRB splashdown sequence5
1.2	Damaged SRB forward skirts6
2.1	Schematic of parameters and coordinate system for wedge impact problem12
2.2	SRB splashdown Dytran coarse model.....26
2.3	Initial impact phase of SRB splashdown27
2.4	Maximum penetration phase of SRB splashdown28
2.5	Rollover phase of SRB splashdown.....28
2.6	Slapdown phase of SRB splashdown.....29
2.7	SRB splashdown sequence phases (Clayton and Craft 1995)30
2.8	Large slapdown-induced acceleration spike STS-89 (McFadden 1999)31
2.9	Acceleration spike predicted with Dytran rigid-body model.....32
2.10	SRB stress model in Dytran simple drop simulation33
3.1	Hinged-cylinder FEM geometry schematic47
3.2	Selected meshes from discretization error exercise50
3.3	Rigid-body displacement of cylinder wall with Lagrangian mesh refinement; Eulerian mesh index held at 352
3.4	Observed order of convergence for RBD of cylinder wall following impact.....53
3.5	Rigid-body displacement of cylinder wall with Eulerian mesh refinement; Lagrangian mesh index held at 354
3.6	Time-integrated kinetic energy for cylinder wall and fluid55
3.7	Stress history for Eulerian refinement using Lagrangian mesh 356
3.8	Stress history for Lagrangian refinement using Eulerian mesh 457
3.9	Still image from LS-Dyna Animation showing poor coupling.....58
3.10	Comparison of LS-Dyna Prediction using mesh index 4 to experimental data60
4.1	Experimental testing assembly for cylinder-water impact.....67
4.2	Experimental drop tank and hinged cylinder setup.....69
4.3a	Still frame from high-speed camera footage.....70

4.3b	High-speed camera footage showing instant of water impact	71
4.3c	Impact +6 milliseconds, with water splashing visible	71
4.4	Wheatstone quarter bridge schematic	73
4.5	Strain gage rosette and alignment	75
4.6	Cylinder schematic and strain rosette locations	77
4.7	Schematic of circuitry design for strain measurement	81
4.8	Wire-wrapped circuitry components for multi-channel strain measurement	83
4.9	Raw V_I voltage differentials recorded at Station 6_CL	84
4.10	Raw V_I voltage differentials recorded at Station 15_CL	84
4.11	Measured time histories of von Mises stress at Station 6_CL	86
4.12	Measured time histories of von Mises stress at Station 15_CL	86
4.13	Al 3003 sample loaded to failure in elastic modulus test	90
4.14a	Initial stress concentration on cylinder wall at initial water impact	92
4.14b	Stress wave moving along leading edge as cylinder penetrates free surface	93
4.14c	Stress wave moving along leading edge as cylinder penetrates free surface	94
4.15	Stress time histories measured with experimental cylinder	95
4.16a	LS-Dyna prediction and measured water impact data for Sta6_CL	96
4.16b	LS-Dyna prediction and measured water impact data for Sta9_CL	97
4.16c	LS-Dyna prediction and measured water impact data for Sta12_CL	97
4.16d	LS-Dyna prediction and measured water impact data for Sta15_CL	98
4.17	Tuning effect for model parameter, E	111
4.18	Tuned LS-Dyna prediction and measured water impact data for Sta_9_CL	112
4.19	Tuned LS-Dyna prediction and measured water impact data for Sta_12_CL	112
5.1	SRB forward skirt splashdown-induced damage	115
5.2	Representative stress history prediction by Dytran	116
5.3	Schematic for buckling in pressure-impulse plane	120
5.4	Schematic of plate element for bending analysis	126
5.5	Mid-surface normal before and after deformation	128
5.6	Output locations used to monitor von Karman and Donnel stability conditions	132
5.7	Cylinder geometry and elastic buckling due to quasi-static compressive loading	135

5.8	von Karman stability conditions (Eqs. 4.7a-c) during compressive buckling.....	136
5.9	Three damaged SRB forward skirts.....	138
5.10	Original mesh of SRB forward skirt FEM.....	139
5.11	Plastic yielding predicted from initial splashdown modeling.....	140
5.12	Buckled SRB forward skirt from compressive loading.....	141
5.13	Hypothetical loading of original forward skirt mesh.....	142
5.14	Remeshed SRB forward skirt.....	143
5.15a	SRB prior to impact with the free water surface.....	144
5.15b	SRB impacting with the free water surface.....	145
5.15c	Contours showing free water surface profile as result of SRB impact.....	146
5.16	Diagonal plastic yielding bands in SRB forward skirt.....	147
5.17	Relative lateral displacement of nodes in forward skirt.....	148
5.18	Buckled patterns on SRB forward skirt.....	148
5.19	Time-dependent von Karman equilibrium condition evaluated for damage and no-damage impact sequences.....	150
6.1	Sample Bayesian network.....	161
6.2	Updated Bayesian network with additional node.....	162
6.3	Bayesian network for quantifying confidence for unmeasured quantity, t_{max}	164
6.4	BN created with WinBUGS software.....	165
6.5	Linking function (Eq. 6.8) plotted through FE model predictions for peak stress.....	175
6.6	Bayesian network for extending confidence quantification to SRB splashdown.....	176
6.7	Prior and posterior density functions for peak stress in the SRB forward skirt.....	177

CHAPTER I

INTRODUCTION

1.1 Overview

One of the challenges presented to engineers in all disciplines is the quantification and management of uncertainty in both analysis and design of engineering systems. It is widely known and well understood that virtually all conditions encountered in natural environments are governed by inherent variability. Furthermore, even the most carefully designed engineering systems are prone to random behavior due to such factors as material variation and design deviations during construction. This inherent uncertainty, due to both random loadings and random system responses, can lead to system failure if not properly considered and understood during the design phase. Smaller, relatively inexpensive engineering systems can be designed for uncertainty through full-scale failure testing, in which many actual systems are subjected to real-world conditions and the failure rate recorded. However, for most real-world engineering systems, failure testing quickly becomes prohibitive due to monetary and/or time constraints. As a result, engineers spend a great deal of time and effort developing mathematical models of engineering systems in order to avoid the costly alternative of testing actual systems for failure.

Modeling of engineering systems can range from simple, closed-form mathematical equations to large, complex computer simulations that require hours or even days to solve. In practical engineering situations where a model needs to be developed for subsequent uncertainty analysis of the system in question, it is important that the computational time required be manageable. Otherwise the monetary and time constraints that make full-scale failure testing

prohibitive again become a factor. Because of these constraints, engineers are forced to contend with still other forms of uncertainty when attempting system modeling. These forms of uncertainty can be referred to generally as informational uncertainty and modeling error. Informational uncertainty is introduced due to a lack of knowledge concerning the statistics of the random variables in the system. Even with a model that perfectly duplicates the actual engineering system, a lack of knowledge concerning the statistics of the random variables in the system will lead to statistical distributions for the output quantities of interest that do not reflect the true random nature of the system. Model error leads to the same problem, for even with complete knowledge concerning the random variables, a model that does not accurately reflect the true behavior of the engineering system will also lead to output statistics that incorrectly represent the system's random behavior. These two additional forms of uncertainty must be carefully managed and understood in order for the benefits of system modeling to be fully realized. Failure to properly take them into account during an uncertainty analysis of an engineering system could lead to non-conservative designs and actually make failure more likely.

The advances in computing power made in recent years have allowed engineers to focus more on modeling of systems in order to make uncertainty analysis more affordable. One area in particular that has seen a recent increase in attempts at computational modeling is fluid-structure impact analysis. In a departure from empirical closed-form equations developed over the years from laboratory experiments and field data, recent attempts at modeling have expanded to include the finite element approach as computing power has become more affordable. The primary drivers in this effort have been engineers working in the aeronautical and aerospace fields (Seddon and Moatamedi 2006), as well as designers of oceangoing vessels (Aquelet et al.

2006). Engineers have shown interest in the ability of helicopters and other aircraft to survive emergency water landings. Designers of ship hulls and offshore oil platforms have also shown interest in modeling the effects of wave impact on their structures. The National Aeronautics and Space Administration (NASA) witnessed damage to the solid rocket booster (SRB) during splashdown in the ocean following space shuttle launches in the 1990s. As a result they too have investigated modeling tools for fluid-structure impact scenarios. All of these investigations have pursued numerical modeling of fluid-structure impact events because full-scale testing of the systems they design— oceangoing vessels, helicopters, and space shuttles, is prohibitively expensive.

Even with the recent advancements in computing power, modeling of fluid-structure impact, particularly with the finite element method, remains a costly undertaking. Commercially available software packages that use FEM for fluid-structure impact such as MSC.Dytran and LS-Dyna use separate Eulerian and Lagrangian solvers for the fluid and structural analyses, respectively. The coupling of the two separate solvers combined with the explicit (i.e. very small time steps) time integration schemes can lead to very long run times even for short-duration impact events. Additionally, the complicated physics involved with fluid-structure impact scenarios as well as the numerical discretization involved in finite element analysis call for close scrutiny of the accuracy of such models. This raises the issue of model validation and verification (V&V), or the systematic quantification and management of modeling uncertainty mentioned previously. Verification and validation under uncertainty present new challenges that must be confronted. Even under very carefully controlled laboratory conditions, it is difficult to get identical results from two experiments conducted in the same way and with the same input conditions. Furthermore, for large systems for which laboratory testing is not possible,

information concerning their behavior often comes in the form of field data for which the exact input conditions are not even known, only the underlying statistical distributions. In short, a practical methodology for model validation must account for the uncertainty which will inevitably be encountered.

As mentioned previously, full-scale testing of many of the systems subjected to fluid-structure impact scenarios is impossible due to economic constraints. However, without full-scale test results to compare directly with computer model predictions, it becomes difficult to assign high confidence to the model results. Therefore, extrapolation techniques must be incorporated to quantify the confidence in inferences made concerning the suitability of a model for an application domain for which test data is not available.

It is the purpose of this research to develop and validate a numerical methodology for the analysis of stochastic fluid-structure impact problems. The analysis framework will include validation of numerical models through laboratory experimentation. Model verification will focus on the necessary resolution required by the finite element model to produce accurate results. Finally extrapolation concepts will be studied in order to gage the applicability of fluid-structure codes to scenarios for which real-world data is unavailable and robust validation therefore impossible. These objectives are discussed in more detail in Section 1.3.

1.2 SRB Problem Background

Two Solid Rocket Boosters (SRBs) are used during each space shuttle mission to help propel the assembly into orbit. After separation from the external tank, each booster falls back through the atmosphere before being parachuted down into the Atlantic Ocean. Splashdown occurs approximately 140 miles from the launch site with a vertical velocity of approximately 75 fps

(United Technologies USBI 1989). Each SRB and the three main parachutes used to slow it down are recovered and reused on future missions. The parachutes are attached to the forward skirt (i.e., upper region) of the SRB, and therefore the assembly impacts the ocean surface in the same vertical orientation in which it is launched. The flared aft skirt of the SRB impacts the water first, and horizontal momentum causes the booster to roll over into a position roughly parallel to the water surface. Fig. 1.1 shows a diagram of the splashdown sequence.

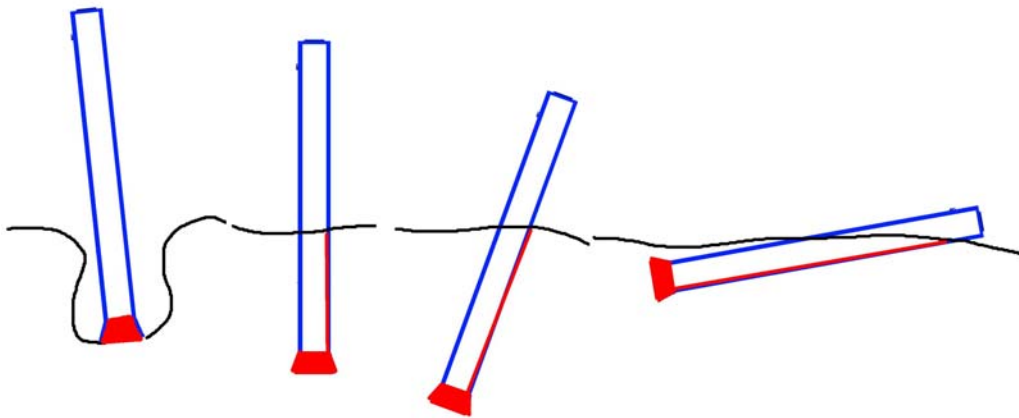


Fig.1.1 – Diagram of SRB splashdown sequence

The rocket is kept from sinking by trapped air located in the burnt out solid propellant motor casing, and eventually the booster settles into a vertical orientation in the water with approximately the top 30 ft rising above the water line.

Prior to the *Challenger* accident, the parachute cords were left attached to the forward skirt during the entire splashdown sequence. However, NASA recovery crews reported difficulties untangling the parachute lines from around the SRB prior to tow back. This frequently resulted in recovery times of several hours, which had potential for exposing the recovery crews to dangerous sea state conditions in the open ocean. In order to reduce the

recovery times, a device was installed that would detach the parachute cords within milliseconds of the aft skirt first impacting the ocean surface. The sudden release of tension in the parachute cords would cause them to spring clear of the SRB and eliminate the tangling problem. The device was first used on the return-to-flight mission following the post-*Challenger* moratorium and performed as designed. However, beginning with STS-37 in May 1991, unexplained damage to the forward skirt of the SRB was observed upon recovery. Another instance of forward skirt damage occurred later that year, and STS-63 in 1995 saw damage to the forward skirts of both boosters. One of the skirts was damaged so severely that it broke free from the motor casing during tow back and was lost (McFadden 1999). The forward skirt is constructed of Al 2219 and is mated to the steel dome on top of the motor casing which holds the solid propellant. Fig. 1.2 shows how the damage is confined to the area just above the interface between the steel motor casing and the aluminum forward skirt.



Fig. 1.2 – Damaged SRB forward skirt

Upon review of ocean surface conditions during previous recovery operations, NASA investigators observed a correlation between cases of damage and high surface wind speeds in the recovery area. They theorized that the damage was resulting from a hard slapping effect as the booster rapidly rolled over from the initial vertical orientation and impacted the ocean surface (McFadden 1999). Later accelerometer data seemed to confirm the “slapdown” theory, showing a large acceleration spike in the forward skirt approximately two seconds after initial impact. Leaving all three main parachutes attached during rollover helped slow down the angular velocity of the SRB, but the new parachute-release mechanism allowed for the SRB to fall freely after initial impact. Eventually a redesigned release mechanism was installed which does not disconnect the cords until after the rollover sequence is complete. Since the implementation of this device no further cases of forward skirt damage have been observed; however, NASA engineers would prefer to have a more complete understanding of the causes of the SRB splashdown issue. Recently conducted tests on an even larger set of parachutes designed for the next-generation Ares I rocket program (NASA 2009) indicate that water splashdown of aerospace vehicles will remain a relevant topic for the foreseeable future.

1.3 Research Objectives and Scope

In light of the preceding discussion, the research objectives and scope of this work are summarized as below:

1. *Development of a finite element-based computational methodology for risk assessment of fluid-structure impact analysis:* risk analysis of the SRB forward skirt damage problem should utilize an appropriate model for the splashdown event, since full-scale testing is prohibitively expensive and available flight data is limited. Therefore in Chapter 2 a review

of fluid-structure impact analysis methodologies is presented, with particular attention given to commercially-available finite element codes that have been recently developed. Two software packages, MSC.Dytran and LS-Dyna, are introduced, and subsequently employed for rigid-body analysis and stress analysis, respectively.

2. *Development of a finite element model verification methodology for fluid-structure impact problems involving two independent meshes (fluid and structure):* the finite element approach to fluid-structure impact modeling introduces numerical uncertainty that will affect the risk assessment. An investigation into the effects of both the fluid and structural mesh discretizations on the finite element predicted is presented in Chapter 3. This approach will build upon single-mesh approaches that utilize Richardson extrapolation in order to quantify discretization error.
3. *Model validation using laboratory experimental data for comparison to a corresponding finite element model of fluid-structure impact:* in the case of the SRB, full-scale tests are infeasible and extensive field data unavailable, therefore validation of the finite element model will be based on small-scale laboratory testing using a thin-walled cylinder that still captures the physics of fluid-structure impact. As presented in Chapter 4, the validation framework will be expanded to account for experimental uncertainty in an effort to determine the significance of model error.
4. *SRB forward skirt failure analysis to correctly characterize and model the failure mechanism that occurs during the splashdown sequence:* the SRB forward skirt damage has been described as “buckling,” yet there has been no investigation into whether this term is truly applicable. As a result, in Chapter 5 a numerical investigation using nonlinear finite element analysis is conducted to determine the true structural failure mechanism causing the forward

skirt damage. As a result of this study, a revised structural failure limit state is developed for use in risk analysis.

5. *Improved SRB forward skirt risk assessment:* the results of the model verification and validation investigations and the forward skirt failure analysis are used to develop a revised risk assessment for the SRB forward skirt as a result of splashdown. The results of the updated risk assessment are presented at the end of Chapter 5.
6. *Extrapolation methodology for quantifying confidence in model predictions for an untested problem domain:* there is little data available concerning SRB splashdown, and failure testing is prohibitively expensive, therefore in Chapter 6 a Bayesian networks methodology is investigated for quantifying any increased confidence in the SRB splashdown model predictions based on the validated laboratory cylinder model and test data.

CHAPTER II

FLUID-STRUCTURE IMPACT MODELING AND SOLID ROCKET BOOSTER SPLASHDOWN

2.1 Introduction

In recent years the complex interactions between impacting structures (such as oceangoing vessels and aerospace vehicles) and fluid volumes have begun to be affordably modeled through detailed numerical simulations. The real-world case that has motivated the research presented here is the solid rocket booster (SRB) splashdown problem experienced by NASA in the 1990s. The variability in the observed damage from one launch to another prompted NASA investigators to seek a risk assessment of the splashdown event. Because full-scale testing of the splashdown scenario is prohibitively expensive, and because available flight data and failure instances are insufficient to accurately estimate the true probability of failure, a risk assessment of SRB splashdown must rely upon a suitable physics-based model of the impact event. This chapter will present background into the field of fluid-structure impact analysis, and will also give an overview of the two commercial finite element codes utilized as part of this study for the risk assessment of SRB splashdown. Details of the risk assessment will be presented, and the needs for model verification, model validation, and a buckling failure definition, topics covered in subsequent chapters, will be highlighted.

2.2 Fluid-Structure Impact Modeling

2.2.1 Early Approaches

The physics of fluid-structure impact are complex, and modeling of such events requires proper understanding of both fluid dynamics and structural mechanics. Numerical approaches for modeling of fluid-structure impact have been investigated extensively in recent years, but experimental and analytical research into the field goes back many decades. Prior to the advent of desktop computing, modeling of fluid-structure impact and resulting engineering designs were based upon analytical equations derived from careful observation and experimentation.

The impact of a structure with fluid was first investigated by von Karman in his study of seaplane floats (1929), in which the concept of added mass was used to explain observations. Wagner (1932) followed with an approximation for a flat plate impacting a free surface. As described by Engle and Lewis (2003), Wagner's approximation for the maximum pressure acting on a wedge impacting water is based on the formula:

$$P_{max} = \frac{1}{2} \rho V^2 (1 + \frac{\pi^2}{4} \cot^2 \theta) \quad (2.1)$$

where P_{max} is the maximum impact pressure, V the initial impact velocity, θ the deadrise angle of the wedge, and ρ the density of water. Much of the subsequent work has extended upon Wagner's approach, with the impacting structure considered to be a rigid body (Lu et al. 2000).

Dobrovol'skaya (1969) first derived similarity solutions for wedges of any deadrise angle impacting and moving through the fluid with a constant velocity, but only showed results for $\alpha \geq 30^\circ$. The wedge velocity is assumed to be constant throughout, and gravity effects are ignored. Though Dobrovol'skaya's solution is valid for any deadrise angle, it cannot be applied to arbitrary shapes (Mei et al. 1999). Zhao and Faltinsen (1993) revisited the wedge problem

using a boundary element method (BEM) and found excellent agreement with Dobrovol'skaya's results.

Armand and Cointe (1986), Cointe (1991), and Howison et al. (1991) all build upon Wagner's theory to include time-dependent effects using matched asymptotic expansions to solve the impact problem for wedges with small deadrise angles. Fig. 2.1 shows a useful schematic containing relevant parameters and coordinate systems for the wedge impact problem.

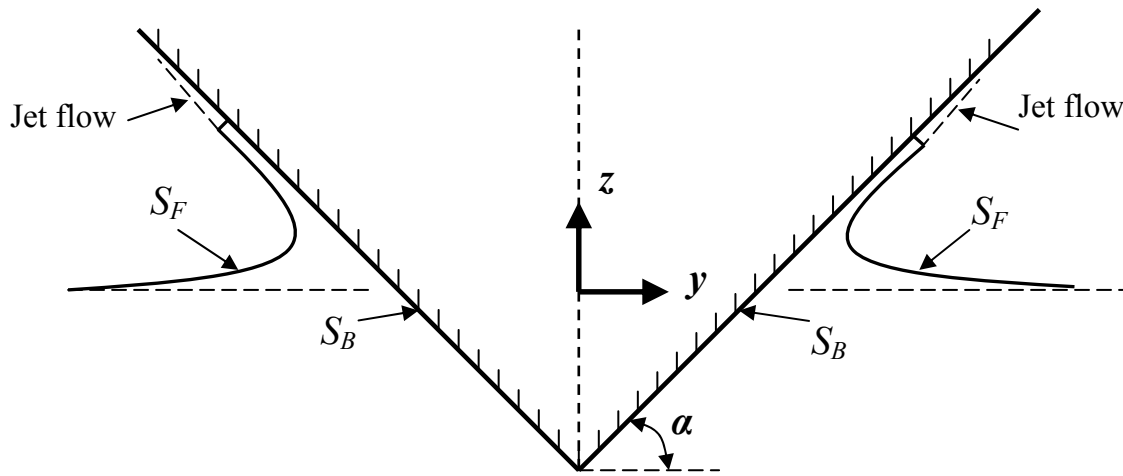


Fig. 2.1 – Schematic of parameters and coordinate system for wedge impact problem

As summarized by Zhao and Faltinsen (1993) the fluid is divided into an inner and outer flow region, with the separation between the two regions determined to be a horizontal distance $y = \pm c(t)$, with $c(t)$ being a function unique to the cross-sectional form of the impacting body. For wedges, $c(t) = 0.5\pi Vt(\cotan \alpha)$, and the pressure acting on the inner flow region is approximated by:

$$p_{in} - p_0 = 2\rho \left(\frac{dc}{dt} \right)^2 |\tau|^{\frac{1}{2}} (1 + |\tau|^{\frac{1}{2}})^{-2} \quad (2.2)$$

Where p_0 is the ambient pressure acting on free surface S_F . The $|\tau|$ term varies from 0 to 1 on the surface of the impacting body S_B , and the maximum pressure acting on the inner surface p_{in} occurs at $y = c(t)$, where $|\tau| = 1$. Therefore, $|\tau|$ is related to the horizontal distance y via:

$$y - c = (\delta / \pi)(-\ln|\tau| - 4|\tau|^{\frac{1}{2}} - |\tau| + 5) \quad (2.3)$$

With $\delta = \pi V^2 2c[4dc/dt]^{-2}$ being the jet thickness, found by matching the inner and outer flow region pressure solutions. The pressure acting on the impact wedge in the outer flow region is given by:

$$p_{out} - p_0 = \rho V c \left(\frac{dc}{dt} \right) (c^2 - y^2)^{\frac{1}{2}} \quad \text{for } |y| < c(t) \quad (2.4)$$

Combining of the inner and outer pressure equations gives a final composite solution for the pressure acting on the impacting body given by:

$$p - p_0 = \rho V c \frac{dc}{dt} (c^2 - y^2)^{\frac{1}{2}} - \rho V c \frac{dc}{dt} [2c(c - y)]^{\frac{1}{2}} + 2\rho \left(\frac{dc}{dt} \right)^2 |\tau|^{\frac{1}{2}} (1 + |\tau|^{\frac{1}{2}})^{-2} \quad (2.5)$$

It is worth noting that in all the above cited work, the velocity of the impacting wedge is assumed to be constant throughout the analysis. In reality this is rarely the case, particularly for structures impacting as a result of free fall. Wu et al. (2004) consider varying velocity (though gravitational effects are still ignored) during impact in their analysis of a wedge in free fall using BEM and an analytical solution based on the shallow water equations. A second consideration of the analytical methods described above is that the impacting structure is considered to be rigid, and the elastic response resulting from impact is not considered. Carcaterra and Ciappi (2004) present findings based upon theoretical and experimental work concerning the hydrodynamic shock induced in elastic, wedge-shaped structures during water impact. Peseux et al. (2005) present experimental results for impact pressures on both rigid and elastic cone-

shaped samples, and compare to predictions from a finite element formulation. Yettou et al. (2006) describe an experimental study for wedges of various deadrise angles, mass, and drop heights, with results compared to theoretical predictions that assume constant entry velocity.

Within the offshore structures field, wave forces on circular members have been computed using drag and inertia forces through Morison's equation:

$$F_L(t) = 0.5\rho DC_d U|U| + 0.25\rho\pi D^2 C_m du/dt \quad (2.6)$$

where $F_L(t)$ is the force per unit length, U is the flow velocity, and C_d and C_m are drag and inertia coefficients, respectively. For impact situations (e.g. waves breaking near mean water level), where the circular member penetrates the free surface and an additional slamming force is registered, the additional load can be accounted for by increasing the drag coefficient, C_d (Garrison 1996). The drag coefficient C_d is conservatively estimated at 3.1 at initial impact and then rapidly decreases as the cylinder penetrates the free surface. However, it has been observed (Kaplan and Silbert 1976) that this simplified approach does not correlate well with experimental data, presumably because it does not include the dynamic response of the structural member. In light of this, Faltinsen et al. (1977) conducted time-dependent numerical analysis of several different elastic beams, with impact forces derived from potential flow theory (see §2.2.2), however poor agreement with experimental data was again observed. Garrison (1996) proposes a new approach to the cylinder impact problem based upon energy principles, with results that are claimed to compare favorably with test data.

Some more recent experimental work has also been conducted concerning the cylinder impact problem. Lin and Shieh (1997) used a digital imaging system and a high-speed data acquisition system to measure the fluid pressure field and fluid flow field simultaneously during cylinder impact with the free fluid surface. Engle and Lewis (2003) performed drop tests for

wedge-shaped solid sections and compared the results to Wagner's theory as well as numerical boundary element and finite element solutions. Additionally, in the aforementioned work of Wu et al. (2004), experimental results for a wedge in free fall impacting a water surface were presented and compared to numerical predictions.

2.2.2 Potential Flow Theory

The theoretical basis for most numerical approaches to modeling of a fluid domain or free surface is known as velocity potential flow theory. This approach assumes the fluid to be incompressible and inviscid, and the fluid region is therefore governed by the Laplace equation:

$$\nabla^2\phi = \frac{\partial^2\phi}{\partial x^2} + \frac{\partial^2\phi}{\partial y^2} + \frac{\partial^2\phi}{\partial z^2} = 0 \quad (2.7)$$

where the velocity potential $\phi(x,y,z,t)$ is a continuous, differentiable, scalar function analogous to the force potential in a gravitational field (Sarpkaya and Isaacson 1981). For a solid body moving through inviscid fluid, the general boundary condition states that the normal component of the velocity vector of the solid boundary must be applied to the fluid adjacent to the boundary:

$$\frac{\partial\phi}{\partial n} = \begin{cases} V_n & \text{on the solid surface} \\ 0 & \text{on the fluid region boundaries} \end{cases} \quad (2.8)$$

where V_n is the normal component of the surface velocity. In the case of a free fluid surface, as with fluid-structure impact problems, both the kinematic and dynamic boundary conditions must also be satisfied. The kinematic condition states that a particle on the free surface must always remain on the free surface.

$$\frac{Dx}{Dt} = \frac{\partial\phi}{\partial x}, \quad \frac{Dy}{Dt} = \frac{\partial\phi}{\partial y}, \quad \frac{Dz}{Dt} = \frac{\partial\phi}{\partial z} \quad (2.9)$$

where (x, y, z) lies on the free surface. Note that in Eq. 2.9 the components of the flow velocity in the fluid region $D(\cdot)/Dt$ are given by the corresponding partial derivatives of the velocity potential, $\partial\phi/\partial(\cdot)$. This illustrates the basis for using potential flow theory to describe the flow in a fluid region. The dynamic boundary condition states that the atmospheric pressure acting on the free surface equals the hydrodynamic pressure within the fluid at the surface.

$$\frac{D\phi}{Dt} = \frac{1}{2} \left[\left(\frac{\partial\phi}{\partial x} \right)^2 + \left(\frac{\partial\phi}{\partial y} \right)^2 + \left(\frac{\partial\phi}{\partial z} \right)^2 \right] \quad (2.10)$$

where (x, y, z) again lies on the free surface.

Solving the Laplace equation yields the velocity distribution in the fluid region. There are many known functional forms that offer a solution to the Laplace equation. In the approach of Zhao and Faltinsen (1993), Green's function is employed to solve for the flow inside the fluid domain. With an expression available for the velocity field components within the fluid, the dynamic forces $F(t)$ applied to the impacting body as it moves through the fluid domain may be found using Bernoulli's equation:

$$\frac{1}{2}(u^2 + v^2 + w^2) + \frac{\partial\phi}{\partial t} + \frac{p}{\rho} + gh = F(t) \quad (2.12)$$

Where again, the flow velocity components are given by the partial derivatives of the flow potential, $\phi(x, y, z)$:

$$u = \frac{\partial\phi}{\partial x}, \quad v = \frac{\partial\phi}{\partial y}, \quad w = \frac{\partial\phi}{\partial z} \quad (2.13)$$

For practical fluid-structure impact problems, potential flow theory and the necessary assumptions concerning cross-sectional form, impact velocity, and structural rigidity can rarely if ever be used to produce an exact solution. However, in recent years many new applications of numerical solutions to fluid-structure impact problems have been developed, and this has

allowed for modeling of both elastic structures and impact configurations that would not be possible using previously described methods.

Battistin and Iafrati (2003) extended the boundary element approach to more arbitrary shapes such as cones, spheres, and cylinders. They compared their predictions for an impacting cylinder to the experimental work of Campbell and Weynberg (1980) as well as to the asymptotic approximation of Armand and Cointe (1986). They found good agreement of their solution with the experimental results, while the asymptotic approach tended to overestimate the hydrodynamic load.

All of the work mentioned so far, and most of the research presented in the literature, treats the impacting body to be rigid. However, the elastic response of the structure could have a significant effect on the pressure loads applied to it by the fluid region. Therefore, attention must also be given to the dynamic behavior of the structure. It is preferable to consider the elastic nature of the structure and couple the two analyses in order to achieve a truly accurate analysis (Maity and Bhattacharyya 2003). Iterative methods can be implemented at each time step during the analysis to ensure that the changing shape of the structure as a result of loading from the fluid is in agreement with the boundary of the fluid. Some non-iterative methods (Lu et al. 2000) have been developed for coupling the solvers in order to avoid the computational expense of iterations. When separate solvers are alternately used to integrate the fluid and structural regions in time, the method is said to be partitioned. Monolithic methods move both the fluid and structural regions forward in time simultaneously (Michler et al. 2002).

Lu et al. (2000) coupled the boundary element approach with FEM analysis of the impacting structure. By using some terms from the preceding time step to effectively linearize Bernoulli's equation, the authors obtain a single structural equilibrium equation for both the fluid

and structure. Concerning wave formation and pressure distributions, they found good agreement with their results and those obtained previously by Zhao and Faltinsen (1993).

Broderick and Leonard (1995) use a coupled approach to study the response of deformable membranes (floating breakwaters, storage bladders) to ocean waves. The coupling of the fluid domain solution and finite element solution is conducted with another iterative scheme in which the hydrodynamic loads are used to update the structural shape and motion, thereby inducing a response in the fluid.

As computing resources have become more widely available, full finite element approaches have been developed in which the fluid domain is modeled fully, not just the free surface. Many finite element approaches to fluid-structure impact modeling use a Lagrangian solver for structural responses and an Eulerian solver for calculations pertaining to fluid motion. In fluid mechanics, there are two ways to consider fluids in motion. The Lagrangian viewpoint considers each individual particle of fluid separately over the entire time period in question (Roberson and Crowe 1997). Since the motion of one particle can affect the motion of others, every single particle must be considered at every time step in order to fully describe the motion of the fluid. This is an enormous computational task when dealing with fluids in motion. However, when applied to structures, the Lagrangian approach often proves quite sufficient. The other approach to fluid dynamics is the Eulerian approach. This method considers only one fixed point in space and calculates the motion of particles passing that point over time (Roberson and Crowe 1997). Similar calculations at other points in the flow field can result in an adequate description of the fluid motion with much less computational effort than the Lagrangian approach. Solid hexagonal volume elements are used to define the region in the model containing fluid. In contrast to traditional structural solids, these elements are fixed in space and

serve as a container for the Eulerian fluid. Elements within the grid may be specified as either containing fluid or being void at the start of the analysis. The fluid is confined by the boundaries of the Eulerian mesh. Flow can be permitted to flow through certain faces of the Eulerian grid, but once fluid passes from the mesh it may not reenter and all data concerning that fluid is lost.

Two different time-integration schemes are used for transient finite element analysis of fluid-structure impact. Implicit time integration schemes remain stable regardless of the size of the time step used, though larger time steps will lead to decreased solution accuracy. Explicit schemes require a time step smaller than the natural period of every element in the problem domain in order to remain stable. For this reason, explicit scheme time steps are usually 100 to 1000 times smaller than implicit time steps. This leads to larger computational expenses, but these are offset somewhat by the fact that explicit codes do not require computationally expensive mass matrix inversion during each iteration (Dytran Theory Manual 2002). Explicit codes are often employed specifically for short-duration, high-frequency impact events such as bird strikes on aircraft (Dobyns 1998) and helicopter impacts on water (Clarke and Shen 1998).

2.3 Commercial Finite Element Codes

As described in §1.2, the physics of the SRB splashdown event are quite complex, and modeling of the sequence must account for the rigid-body motion of the SRB, the deformation of the ocean surface and flow beneath the surface, and the dynamic structural response of the SRB. During the rollover phase of SRB splashdown, drag forces act upon the aft segment of the SRB that has penetrated the ocean surface. The magnitude of these drag forces is dependent upon the depth of penetration and the horizontal velocity of the SRB. Therefore it is necessary for the computational model chosen for the SRB splashdown event to be able to compute these drag

forces. This rules out the use of boundary element approaches (at least for capturing the rigid-body motion of the SRB) since they only model the free fluid surface and would not be able to accurately describe the rollover phase of splashdown. Presumably in such a formulation the SRB would simply penetrate the free surface (with pressures applied to the aft section) while remaining in the initial vertical orientation.

A second consideration for selection of the splashdown model is the structural complexity of the SRB. Though it may seem that a simple idealized cylindrical structure could be used, the SRB contains many different material types as well as internal structural stiffeners. Furthermore, the observed damage has been confined to one particular region of the forward skirt, implying that the dynamic structural response that is unique to the SRB must be accurately modeled in order to predict the slapdown damage. In short, it is believed that idealized structures such as the cylinders and wedges used in the analytical approaches discussed in §2.2.1 are insufficient for accurate prediction of the forward skirt damage. Because the model selected for SRB splashdown will need to be analyzed repeatedly for the purposes of the risk assessment (whether for simulation purposes or for iterative approximation techniques such as FORM), it is preferable from a data-management point of view to have the fluid and structure domains of the model solved at the same time. This avoids potentially cumbersome sequential analyses of the fluid and structural domains, as well as the need for iterations for solution convergence.

For complex, multi-phase loading situations such as that encountered in the SRB splashdown case, it is not uncommon to use piecemeal analysis wherein, for example, pressure loads are generated with a time domain analysis and then applied separately to a static structural model of the impacting entity. Such an approach was applied by Kross et al. (1983) when analyzing the aft sections of the SRB during splashdown. However, one result from this work

was the observation that using an equivalent static analysis under predicted the observed impact damage. Therefore the analysis code chosen for SRB splashdown should employ transient analysis so as to capture the effects of structural dynamics.

In light of all these considerations, a finite element approach such as that described in §2.2.4 that couples a Lagrangian structural solver with an Eulerian fluid region appears to be suited for efficient analysis of the SRB splashdown problem. The FEM approach models the entire three-dimensional volume of fluid and can therefore capture the drag effects acting on the aft segment of the SRB. Additionally, the complex structural features of the SRB assembly can be modeled through the use of beam, shell, and solid structural elements. Two such finite element codes are commercially available for modeling of fluid-structure impact problems: MSC.Dytran and LS-Dyna. The following sections will give background on these two commercial FEM codes and their respective applicability to the fluid-structure impact analysis.

2.3.1 MSC.Dytran

MSC.Dytran is a product of the MacNeal-Schwendler Corporation and has been used previously for analyzing a wide range of impact scenarios, such as bird strikes on aircraft wings and helicopter impacts with water (Dobyns 1998; Clarke and Shen 1998). The Dytran analysis code employs an iterative coupling algorithm for handling of the separate Lagrangian and Eulerian solvers (Dytran Theory Manual 2002). Initially the two solvers are completely independent, and no interaction takes place unless specified by the user. Dytran employs an explicit time integration scheme to perform transient analysis and is best suited for short-duration events involving high-frequency structural responses (Dytran User's Guide 2002). The input data, analysis details, and output options are established with the Patran user interface.

One distinct feature of Dytran is the need for a coupling surface to define the boundary between the fluid and structural regions. The coupling surface must form a closed volume, and fluid in the Eulerian region is not allowed to penetrate. The coupling surface is constructed by specifying the surfaces of either shell or solid structural elements, and it will deform with the structure throughout the analysis. Without the coupling surface, the Lagrangian and Eulerian elements would pass straight through one another with no interaction whatsoever. The coupling surface allows for forces created during the impact to be passed into the structure and also propagated through the fluid. It is sometimes necessary to employ dummy shell elements to achieve a closed volume. One feature of note concerning Dytran is the fast-coupling algorithm that can be invoked during analysis. This feature allows for significantly faster analysis times, but can only be used when the Eulerian grid is in alignment with the three axes of the global coordinate system.

2.3.2 LS-Dyna

The finite element code known as LS-Dyna originated as DYNA3D at the Lawrence Livermore National Laboratory in the 1970s (LSTC 2006). It was developed specifically for and has been widely used in modeling of structural impact problems. LS-Dyna is a nonlinear finite element package for modeling of both large displacements and material nonlinearity. Like MSC.Dytran, LS-Dyna can model the structural components in a Lagrangian formulation while using an Eulerian mesh for the fluid region. However, one feature of LS-Dyna that distinguished it from Dytran is the automatic coupling of shell, brick, and beam elements with the Eulerian region. This eliminates the sometimes cumbersome task of defining a closed-volume coupling surface. Another distinguishing feature of LS-Dyna is the smooth particle hydrodynamic (SPH)

capability. This technique allows both the fluid and structural regions to be modeled with the Lagrangian approach (Fasanella et al. 2003). Unlike Dytran which uses the Patran user interface, LS-Dyna has its own graphical interface for pre- and post-processing. LS-Dyna also features a very useful translator feature that allows models created with other FEM codes (such as MSC.Nastran) to be imported and converted into the appropriate element type. The fluid-structure impact formulation within LS-Dyna is invoked using the following commands or “cards” in the bulk input file:

The *CONTROL_ALE card is used to specify the global analysis formulation. By setting the “DCT” parameter = 3, the user specifies an Arbitrary Lagrangian-Eulerian (ALE) formulation. The “NADV” parameter specifies the number of time steps to perform between advection cycles, which are the iterative steps taken by LS-Dyna to couple the fluid boundary with the deforming structure. The “METH” parameter is used to specify the advection method, with a value of 2 specifying a 2nd order accurate scheme. Various smoothing parameters can also be specified with this card.

The *CONSTRAINED_LAGRANGE_IN_SOLID keyword is used to specify which geometric regions comprise the “slave” and “master” components of the ALE formulation. The Lagrangian structural mesh is designated the “slave” part, while the Eulerian fluid region is designated as the “master” part. This card also contains parameters concerning the coupling locations of the two meshes, as well as the type of coupling algorithm to be employed.

The *SECTION_SOLID_ALE keyword is used to define the solid elements that make up the Eulerian fluid region. The ELFORM parameter is set to 12 to indicate a single integration point for the element (for fast computation), with void regions possible as material moves

through the mesh. The *MAT_ELASTIC_FLUID card defines water as an isotropic elastic material, with the fluid density ρ and bulk modulus K being the only required parameters.

These are by no means the only components of the bulk input file needed for the LS-Dyna analysis. They are shown here only to give the reader a general sense of how the ALE formulation for fluid-structure impact problems is invoked within LS-Dyna. Recall the *CONSTRAINED_LAGRANGE_IN_SOLID keyword mentioned previously. This and the *CONTROL_ALE keyword both contain parameters specifying the type of coupling procedure for LS-Dyna to perform during the course of the analysis.

2.4 Modeling of Solid Rocket Booster Splashdown

In previous studies of the SRB splashdown sequence (Mitchell et al 2003; Mitchell and Mahadevan 2004), two separate finite element models are developed with MSC.Dytran in order to bring computational times down to a manageable level. The time step is governed by the single element in the model with the highest natural frequency, therefore overall run times are controlled largely by this one element. Even if the model is otherwise coarsely meshed, a single high-frequency element will reduce the time step and result in longer run times. The SRB splashdown sequence (see Fig. 1.1) takes between 2-5 seconds from the time of initial impact until the forward skirt impacts the water surface, depending upon the initial horizontal and vertical impact velocities. The original finite element model of the SRB provided to the author by NASA contains approximately 12,000 structural elements, the smallest of which requires a time step of 1.558E-06 seconds. This small time step, combined with the additional Eulerian elements needed to model the ocean water makes analysis of the full SRB splashdown sequence

using this model impractical from a computational time perspective. As a result two separate models are used for modeling the entire splashdown sequence:

1. The first model simulates only the rigid-body behavior of the SRB during splashdown and is used to predict the impact velocity of the forward skirt following rollover.
2. The second model is the finite element model originally provided by NASA, used here to predict the actual stresses in the SRB forward skirt resulting from a blunt impact with the free water surface at varying impact velocities.

Previously, it was mentioned that prior piecemeal approaches used for analysis of the SRB impact had proven inadequate for predicting observed damage levels (Kross et al. 1983). However, the work cited referred specifically to using equivalent static analysis in tandem with a loading history generated from a prior analysis. The approach employed here is only used to transfer impact velocities from the coarsely-meshed rigid-body model to the high-resolution stress model. Both stages of the modeling approach employ the exact same transient analysis, and there is no transfer or approximations of pressure fields, deflections, or stresses. In the subsequent sections, both the rigid-body and stress models are described in more detail, along with the results obtained using each.

2.4.1 SRB Rigid-Body Model

The coarse model consists of 732 shell elements and is used to predict the rigid-body behavior of the SRB as it impacts the water and rolls over into the horizontal orientation. So as to accurately capture the drag forces acting on the lower segments of the SRB once they have penetrated the water surface, the model is given the same outer dimensions as the actual SRB.

Also, the thicknesses of the shell elements in the various sections are varied until both the overall mass and the location (along the central vertical axis) of the center of gravity both match those for the actual SRB. The water region is modeled using 1782 rectangular Eulerian solid elements, with increased resolution near the free surface. Using this coarse model, the entire splashdown sequence from initial impact to forward skirt slapdown can be modeled in approximately 2 hours on a 2.4 GHz desktop workstation. It should be noted that these analysis times are achieved by invoking the fast coupling algorithm mentioned previously in §2.3.1. Fig. 2.2 shows the coarse model developed with Dytran to model the rigid-body behavior of the SRB during splashdown.

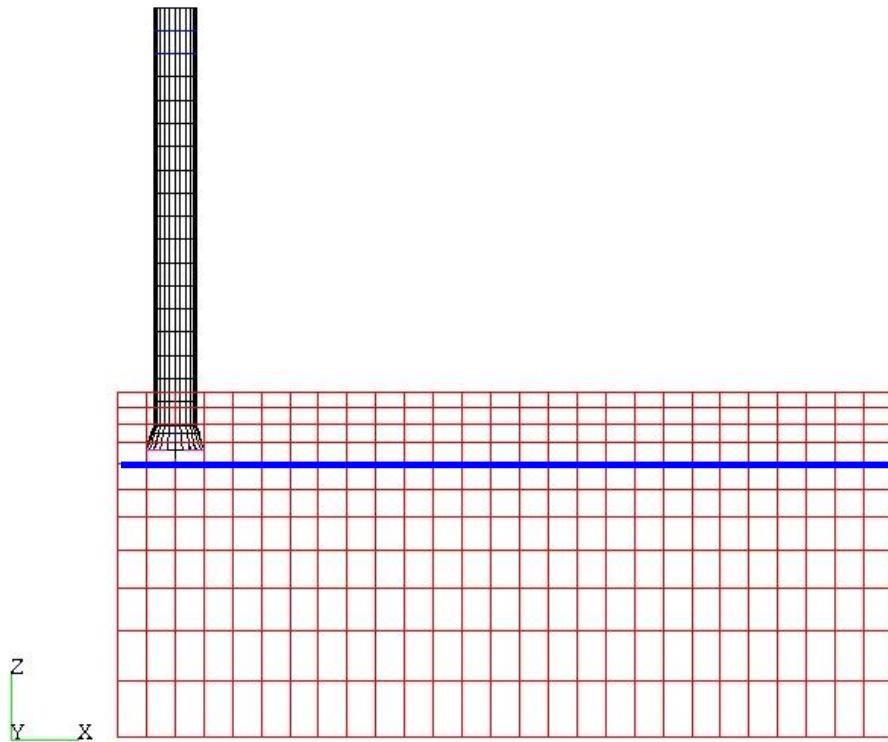


Fig. 2.2 – SRB splashdown Dytran coarse model

The blue horizontal line represents the free water surface, established by specifying the four uppermost Eulerian layers of elements as being empty. The elements below the surface are

specified as containing a fluid with the same density as water. The Eulerian elements remain stationary throughout the analysis, but the modeled water is free to move around within the region.

The Lagrangian grid points defining the SRB are given an initial velocity containing both a horizontal (+X) and vertical (-Z) component in order to simulate the impact trajectory of the falling SRB. This allows the velocity at which the forward skirt impacts the ocean surface (during the “slapdown” phase) to be defined as a function of the two components of the initial impact velocity. Additionally, an acceleration field is applied in the -Z direction to simulate the effects of gravity.

The results of the Dytran analysis can be visualized using animation features included with the software. For clarity, only the free fluid surface separating the water from the empty region on the Eulerian mesh is shown in the animations, though the entire volume below the surface indicated by the blue line in Fig. 2.2 is modeled. Figures 2.3-2.6 show screen captures from an animation produced from a typical Dytran analysis.

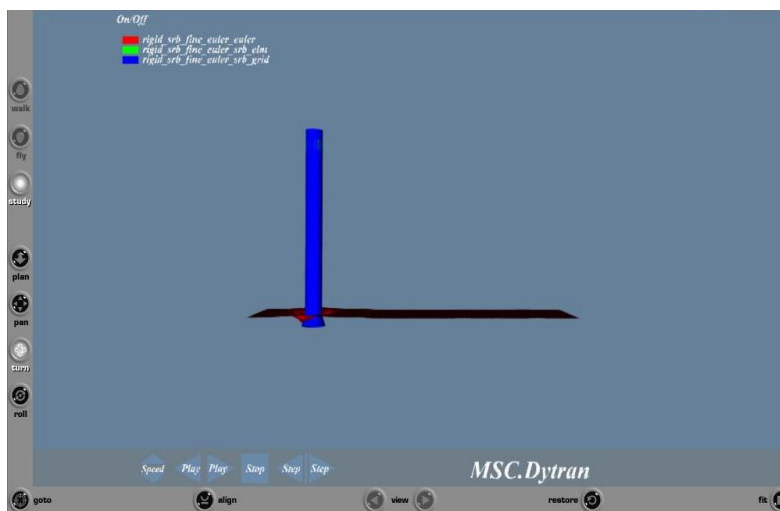


Fig. 2.3 – Initial impact phase of SRB splashdown

As the flared aft segment of the SRB penetrates the ocean surface, horizontal momentum results in drag forces acting on the portions below the surface.



Fig. 2.4 – Maximum penetration phase of SRB splashdown

A fraction of a second later, the SRB has penetrated as far beneath the ocean surface as it will go. Horizontal momentum has carried the SRB forward through the water, briefly forming a cavity behind the aft portion.



Fig. 2.5 – Rollover phase of SRB splashdown

During the rollover phase, the cavity that had formed previously behind the SRB has collapsed, and drag forces acting on the submerged sections are forcing the entire assembly over towards a second impact with the ocean surface.



Fig. 2.6 – Slardown phase of SRB splashdown

During the slardown phase, the forward portion of the SRB experiences a blunt impact with the free water surface. The lateral velocity of the SRB sections at impact increases the farther from the center of rotation, and therefore impact forces are greatest at the forward end of the SRB (the same portion that has experienced damage).

There is very little actual flight data concerning the SRB response to water impact available to the author, and therefore comparisons with the splashdown sequence as modeled with the Dytran rigid-body model can only be done qualitatively. With that qualification, the four phases of SRB splashdown shown in Figs. 2.3-2.6 compare favorably with those shown in Fig. 2.7 (Clayton and Craft 1995):

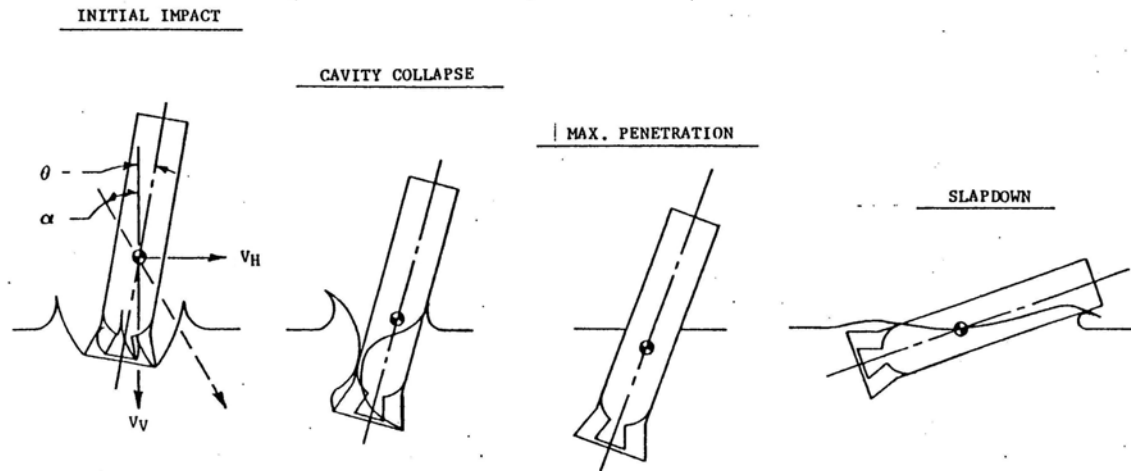


Fig. 2.7 – SRB splashdown sequence phases (Clayton and Craft 1995)

In addition to capturing the overall rigid-body behavior of the SRB during splashdown as it has been observed during actual flight missions, the coarse model developed with Dytran also registers increased loadings acting upon the forward skirt segment during the slapdown phase (Fig. 2.6). A space shuttle mission from January of 1998 (STS-89) included data acquisition systems onboard the SRBs for recording of accelerations encountered during launch, reentry, and splashdown. STS-89 sustained damage to the forward skirt as a result of splashdown. The recorded data shows a dramatic acceleration spike roughly 2 seconds after initial impact of the aft skirt with the ocean surface, as shown in Fig. 2.8 (McFadden 1999). The Dytran coarse model predicts this same sort of acceleration spike for the SRB forward skirt during the slapdown phase.

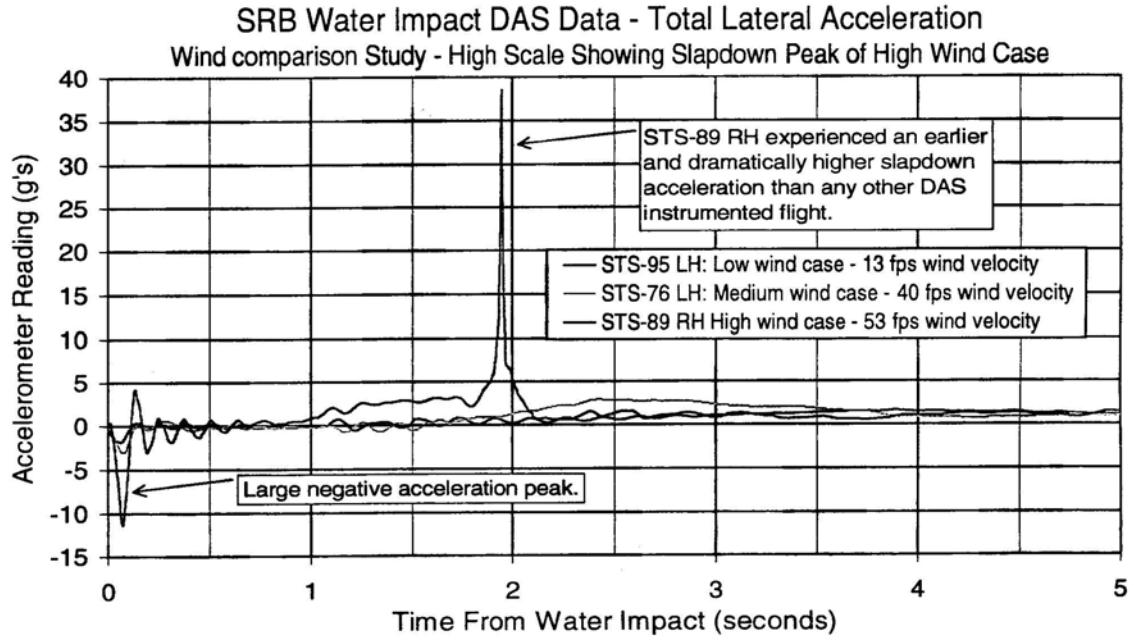


Fig. 2.8 – Large slapdown-induced acceleration spike, STS-89 (McFadden 1999)

Fig. 2.9 shows the vertical (-Z direction in Fig. 2.2) acceleration levels predicted for the SRB forward skirt. A low pass digital filter set to 10 Hz was used to smooth out the predicted time series, since the small time step used in explicit analyses often produce high frequency oscillations in the predicted response. In addition to moderate variations in the impact conditions for the two cases, the signals shown in Figs. 2.8 and 2.9 are also not directly comparable due to fact that the flight data accelerations are relative to the actual body of the SRB, while the Dytran prediction is based on a fixed Cartesian coordinate system. The sustained oscillations in the Dytran prediction are due to under-damping of the system when the default damping parameters are invoked.

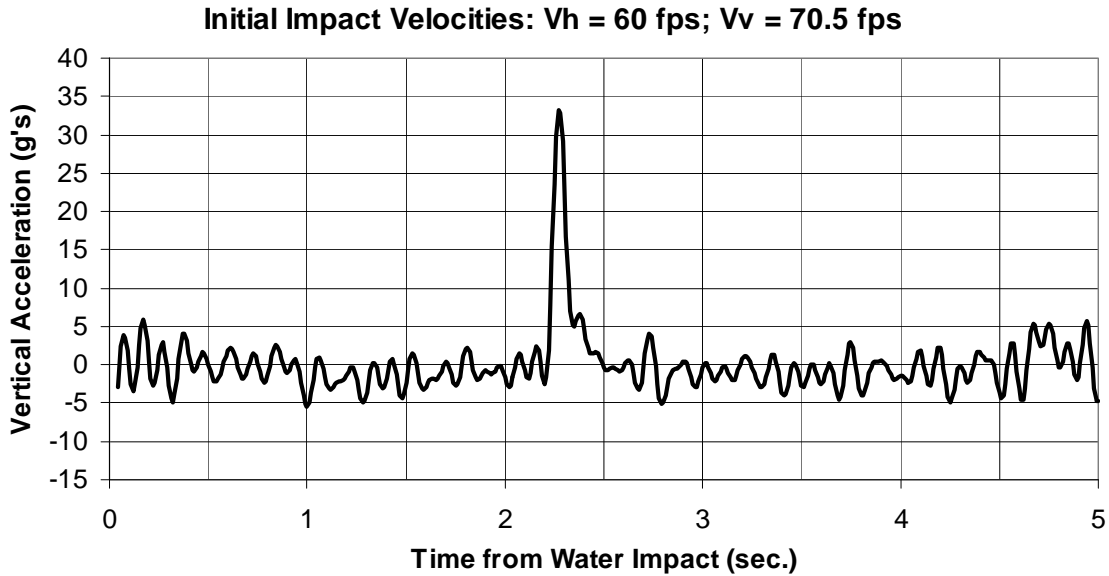


Fig. 2.9 – Acceleration spike predicted with Dytran rigid-body model

Note that in the actual SRB flight data plot in Fig. 2.8 the signal is dampened as a result of energy dissipation through the sea water and from structural damping. The dramatic acceleration spike predicted by the Dytran model for impact conditions comparable to those of STS-89 indicate that overall the physics of the splashdown sequence are being adequately captured.

This section has described the Dytran finite element model used to model the rigid-body behavior of the SRB during the splashdown sequence. Qualitative results compare well with the limited available observations. The slapdown velocities predicted by the rigid-body model for the forward segment of the SRB are next used as initial conditions for the high-resolution model used for stress analysis. The details of this approach are described in the next section.

2.4.2 SRB Stress Prediction Model

The second model used for the SRB splashdown analysis is of a much higher resolution, and it is used to directly predict stress time histories in the forward skirt resulting from blunt

water impact during slardown. The slardown velocity taken from the rigid-body model prediction is used as an initial condition in a straightforward vertical drop configuration using this stress model. An Eulerian region is defined adjacent to the SRB, such that the SRB is parallel to the free fluid surface representing the ocean water. Fig. 2.10 shows the vertical drop configuration used to model the slardown phase with Dytran.

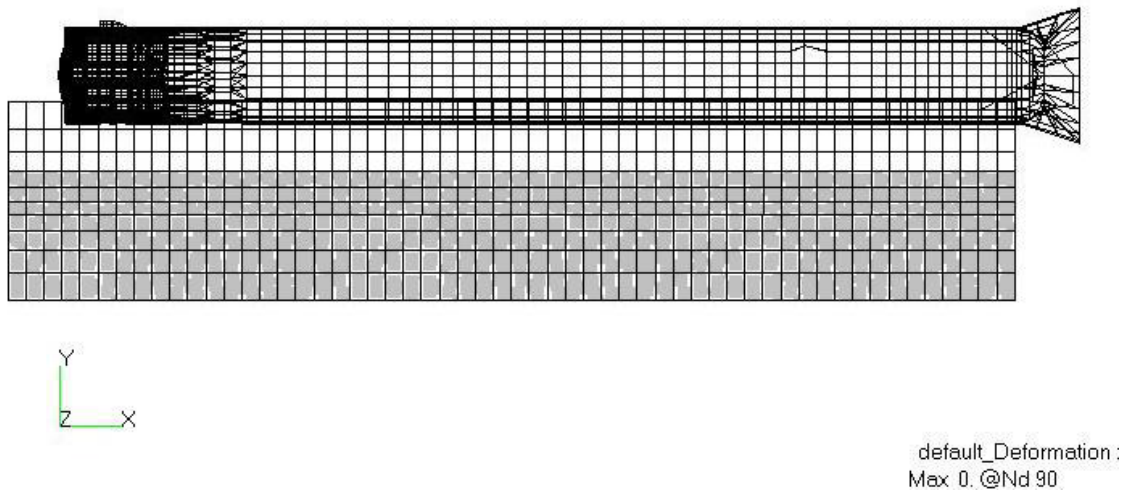


Fig. 2.10 – SRB stress model in Dytran simple drop simulation

A gravity field is defined (-Y direction) and the entire structure is given an initial velocity equal to the slardown velocity predicted using the rigid-body SRB model. The assembly impacts the fluid region in the same blunt, horizontal orientation with which it experiences the slardown effect. Dytran allows for multiple fluid densities within the Eulerian region, and so a layer of air is included on top of the water region, since previous studies have shown that the inclusion of air in such models can have a significant effect of the impact forces generated (Bereznitski 2001).

The structural finite element model of the SRB contains roughly 12,000 beam, shell, and solid elements, and over 150 different material types, while the Eulerian fluid mesh contains

5,600 solid rectangular elements. As can be seen in Fig. 2.10, the resolution is greater in the forward skirt section of the SRB so as to better capture the stresses generated by the impact event. This increased resolution necessitates a smaller time step for the explicit transient analysis, and combined with the larger number of nodes this leads to model run times on the order of 16 hours for 0.5 seconds of analysis time.

It should be noted that the forward skirt is not a uniform structure about its circumference. The side of the forward skirt closest to the external tank and space shuttle during launch contains a reinforced connection point to transfer the thrust to the rest of the assembly. This side of the forward skirt contains additional stiffeners and supports and is therefore stronger than the outer facing, non-reinforced side. In all instances of damage to the forward skirt, such as that seen in Fig. 1.2, the yielded region has been located on this outer, weaker side. This seems to imply that the axial orientation of the SRB at impact plays a role in whether or not damage occurs. In order to investigate this notion further, multiple impact tests are conducted using the stress model in which different sides of the SRB act as the leading edge. The details of this approach, along with the procedure used in previous risk assessment studies of SRB splashdown are presented in the next section.

2.4.3 Risk Assessment of SRB Splashdown

The precise conditions under which the SRB impacts the ocean surface are different from mission to mission due to random variation among several parameters. The horizontal velocity of the SRB at impact is perhaps the most widely varying parameter, with NASA records showing a range of horizontal impact velocities varying from less than 10 fps up to 59 fps (STS-63, when both forward skirts sustained damage). The nominal vertical velocity of the SRB at impact of

75 fps (Rodier et al. 1984) could also vary depending upon random atmospheric conditions and parachute behavior. A third random variable to consider is the axial orientation of the SRB at impact, for reasons discussed previously. Other random conditions which could play a role in the occurrence of the forward skirt damage include surface wave conditions such as wave height and length. These conditions are obviously closely correlated with the surface wind speed, and there is speculation that the forward skirt damage could result from the impact of the forward skirt with the crest of a wave (Clayton and Craft 1995). However, due to the difficulty of modeling wave conditions with Dytran as well as the added computational expense, the only random parameters considered for this study include the impact velocity components and the axial orientation of the SRB.

Use of the piecemeal (i.e., coarse rigid-body model and high-resolution stress model) modeling approach for the SRB splashdown sequence results in manageable model run times that would not be achievable otherwise. However, these analysis times are still on the order of hours and therefore cannot be used directly in a simulation approach to risk assessment, in which hundreds or thousands of model evaluations are required. Iterative approximation methods for risk assessment (such as FORM and SORM) also require multiple model evaluations, and may encounter convergence problems for large, complex models that lack smooth, continuous response domains. Therefore, for this study a response surface approach will be used to predict the velocity at which the forward skirt strikes the ocean surface as a function of the two velocity components (horizontal and vertical) of the entire SRB at initial impact. So as to thoroughly cover the input domain for the horizontal and vertical velocity components at initial impact, a battery of 45 model runs are conducted with the horizontal velocity varying between 20 fps and 60 fps, and the vertical velocity varying between 66 fps and 84 fps. This range of inputs is

chosen so as to provide loading trends for the SRB forward skirt and to give insight into initial velocity thresholds above which damage is possible. Flight data from previous shuttle missions is used to provide a statistical distribution for the horizontal velocity of the SRB at initial impact. The vertical velocity is assumed to follow a normal distribution, with 75 fps taken as the mean value.

The limit state used to define damage (i.e. structural failure) to the SRB forward skirt is given in Eq. 2.14:

$$\sigma_y - \sigma_{vm} \leq 0 \quad (2.14)$$

where σ_y is the yield stress of Al 2219 (57.3 ksi) and σ_{vm} is the maximum von Mises stress in the forward skirt as calculated by Dytran. The high-resolution model of the forward skirt returns different stress levels depending on which side of the SRB leads during the impact with the water. As mentioned previously, stress levels are higher when the non-reinforced side impacts the water first. Therefore, in order to gain an accurate picture of the response of the forward skirt to impact at a particular velocity, multiple analyses are conducted with different sides of the SRB serving as the leading edge. For this study, the SRB is rotated 90° between each drop in order to gage the stress response as the leading edge changes. This creates four separate limit states for use in the probabilistic analysis. The stress model is used to find the minimum velocity at which yielding in the forward skirt takes place for each of the four impact orientations. Each of these velocity values serves as the failure threshold in a Monte Carlo simulation based on the rigid-body model response surface previously described. Since there is no information available to suggest that one side of the SRB is more prone to serving as the leading edge at impact, it is assumed that the axial orientation is a uniform random variable. The four Monte Carlo simulations return failure probability estimates for each of the four impact orientations. The

overall damage probability of the SRB forward skirt is then computed through the union of the four failures.

The results of the risk assessment were heavily dependent upon assumptions made concerning the failure definition of the forward skirt. Using the von Mises yield criterion alone ignores additional considerations such as number of failed elements needed to produce the observed damage, as well as the duration of the time those elements exceed the yield stress. Depending upon assumptions made concerning these points, the predicted risk ranges from 14.1% to 20.2%. Both of these estimates are considerably higher than the observed failure rate, which has produced 4 damage cases out of 108 splashdown events, for a nominal rate of 3.7%.

2.4.5 SRB Risk Assessment Challenges

The lack of a clear failure definition for the forward skirt buckling damage causes difficulty when attempting to predict the forward skirt damage rate for SRB splashdown. The observed damage has been termed “buckling” by NASA investigators, but there is not stress or deflection data available from actual shuttle missions that would confirm or dispel this designation. The observed failure patterns represent the only available evidence for comparison to model predictions.

In addition to the challenge of finding an appropriate failure definition, there is very little actual SRB flight data available to the author, making it impossible to validate the Dytran finite element models beyond simple, qualitative comparisons. Furthermore, the Dytran stress model is hindered by numerical instabilities that cause many of the analyses to terminate abruptly. Depending on the impact velocity, the stress model evaluations return results for anywhere from 0.05-0.15 seconds following impact before unbounded deflections form and the analysis

terminates. These instabilities could be the result of improper connections within the model or insufficient mesh resolution for capturing of the buckling failure mechanism. The instabilities could also be the result of hour-glassing susceptibilities inherent to the reduced-order elements frequently used in explicit time integration algorithms. As a result of these issues, the finite element model verification and validation investigations presented in subsequent chapters are conducted using LS-Dyna.

2.5 Concluding remarks

The initial attempt at conducting a risk assessment for the SRB forward skirt during splashdown using finite element analysis has raised several issues which must be confronted in order to produce more accurate risk estimates for fluid-structure impact problems of this nature. Though more affordable computing resources have allowed for commercial finite element software packages to be applied to fluid-structure impact problems, there still exists a need to understand the applicability and limitations of these codes, and to ensure that the information obtained from them is properly interpreted and used for risk analysis. Each of the remaining chapters will present research conducted in order to improve upon the SRB risk assessments.

Chapter 3 will discuss ways of estimating discretization error in the finite element results so that an optimal mesh resolution can be obtained. Discretization error is inherent to numerical formulations, and the SRB risk analysis would benefit from careful examination of this error source. The goal is to produce optimal mesh resolutions for both the fluid and structural domains such that accuracy and model evaluation times are appropriately balanced.

Validation of these finite element models is needed to confirm (or refute) that they capture the true physics of the impact scenario with a suitable degree of accuracy. However,

since no full-scale SRB response data is available for a quantitative comparison, scaled experimental testing described in Chapter 4 will be performed in order to gage the accuracy of similarly constructed finite element models for a specific impact scenario under controlled laboratory conditions.

In addition to the fluid-structure coupling issue, and whether impact forces are adequately simulated and applied to the structural domain, the finite element model needs to capture the failure mechanism leading to the SRB forward skirt buckling damage. Chapter 5 discusses several potential modes of buckling failure for cylindrical structures and covers previous work where similar numerical codes have been implemented for failure modeling. The lack of flight data pertaining to the SRB splashdown means that the true mode of failure is unknown, and it is hoped that the FEM simulations used in this study will shed insight into this area of concern. The improved failure definition will then serve as a means for revising the previous risk assessments for SRB splashdown damage discussed previously.

Finally, Chapter 6 will present a framework for quantifying confidence in the SRB forward skirt splashdown model (using the updated failure definition) based upon the validation results of Chapter 4. A Bayesian network methodology is presented for established a mathematical link between the laboratory experimental cylinder domain and the real-world SRB splashdown sequence.

CHAPTER III

MODEL ERROR QUANTIFICATION FOR FLUID-STRUCTURE

IMPACT ANALYSIS

3.1 Introduction

This chapter discusses the issue of model uncertainty in risk assessments of fluid-structure impact problems such as the SRB splashdown sequence discussed in Chapter 2. As noted in Chapter 2, previous efforts concerning risk analysis of SRB splashdown (Mitchell 2003; Mitchell and Mahadevan 2004) have resulted in predictions that differ significantly from the observed failure rate, due in part to the presence of model uncertainty in the finite element predictions used in the probabilistic formulations. Model verification and validation (V&V) is the systematic management of modeling error, and it is described here in the context of fluid-structure impact problems. Since full-scale experimental testing of the SRB is prohibitively expensive, this research effort employs a simplified experimental framework utilizing a simple hinged aluminum cylinder in laboratory experimentation. The objective of this small-scale testing is to provide insights into the required model form (validation) as well as the required numerical resolution (verification). Results from the verification exercise are presented and discussed in this chapter, while the validation framework and application is presented in Chapter 4. Such information could provide improved confidence for real-world reliability predictions of fluid-structure impact events such as SRB splashdown.

In recent years engineers have begun to simulate complex real-world systems using numerical models and to attempt to quantify the uncertainty in model predictions. However,

even with these advancements, modeling of fluid-structure impact problems remains a computationally expensive endeavor, particularly by means of the finite element method. Commercially available software packages that use FEM for fluid-structure impact typically use separate Eulerian and Lagrangian solvers for the fluid and structural analyses, respectively. The complex physics involved with fluid-structure impact scenarios as well as the numerical discretization involved in finite element analysis call for close scrutiny of the accuracy of such models. Therefore modeling uncertainty becomes a significant issue when attempting to use finite element methods as a basis for probabilistic assessments of fluid-structure impact scenarios.

By their nature, fluid-structure impact events include random variation, since both to the structural response characteristics as well as the impact trajectories will vary from one impact scenario to another. The SRB forward skirt damage (Fig. 1.2) is one such example, since damage occurred in only four instances out of more than one hundred splashdowns. The sequence involves complex interactions between the impacting SRB and the ocean surface, with the initial impact trajectory influencing the subsequent rollover characteristics and ultimate slapdown loading on the forward skirt. Risk analyses of such complex physical systems therefore require a framework for quantification of numerical error. For the reasons outlined above, this chapter focuses on numerical model error estimation for fluid-structure impact analysis.

It is helpful to consider modeling error as arising from two primary sources: model form error, ε_f , and numerical error, ε_n . Model form error ε_f is the result of the theory underlying the chosen model only partially capturing the physics of the real-world system being investigated.

The numerical error ε_{num} can be attributed to any computational approximations made during model evaluation, such as rounding and domain discretization.

Comparison of model prediction with observed data is needed to systematically quantify and reduce model form error ε_f , and it will be covered further in Chapter 4. This chapter focuses on numerical error, ε_n , through model verification, defined here as the process of determining whether the mathematical steps taken during a model implementation are performed correctly and in keeping with the underlying theory. Verification is of particular importance when dealing with transient finite element schemes, since the spatial and temporal discretizations employed introduce approximations into the model by necessity.

3.2. Discretization Error Quantification

Roy (2005) provides an excellent overview of discretization error estimation methods. Such methods can generally be classified as either *a priori* or *a posteriori* methods. *A priori* methods are more analytical in nature, and seek bounds on the discretization error before the analysis is conducted. However, this often presents challenges for practical problems, so most research is focused on *a posteriori* methods.

Ainsworth and Oden (2000) offer extensive coverage of *a posteriori* methods. These approaches can be subdivided further into finite element-based methods and extrapolation techniques (Roy 2005). Finite element-based methods include the *ZZ* error estimator (Zienkiewicz-Zhu 1992; Ainsworth and Oden 2000), which looks at the gradients of the solution in neighboring elements. However, error estimates are limited to the global energy, and extension to other quantities of interest is problem-dependent. Extrapolation techniques come in two forms: *h*-extrapolation where a given mesh (spatial or temporal) is refined and reanalyzed

and p -extrapolation where the same mesh is solved with successively higher orders of accuracy (i.e., higher order shape functions). h -extrapolation is more widely used due to its ease of use and versatility, and is based upon Richardson extrapolation (RE). The RE approach relies on certain key assumptions, chiefly that the solutions converge asymptotically as the mesh resolution increases, and it involves describing the solution to the discretized problem as a function of the grid spacing. This is an asymptotic expansion approach to quantifying discretization error, since the ideal solution is extrapolated for $n \rightarrow \infty$ after conducting a few analyses at various mesh sizes (Stetter 1973). It should be emphasized that Richardson extrapolation assumes the chosen meshes are sufficiently resolved so as to be within this asymptotic range, but for most practical FEM applications, there is no way of knowing in advance whether this critical resolution has been reached. Richardson extrapolation expresses the discretization error (DE) for a particular mesh k with element edge length h_k as a series expansion:

$$DE_k = f_k - f_{exact} = g_1 h_k + g_2 h_k^2 + g_3 h_k^3 + \dots + \text{H.O.T.} \quad (3.1)$$

with g_i being the coefficient of the i th error term in the series and H.O.T. representing the higher order error terms, which are assumed to be small in the asymptotic range. Standard Richardson extrapolation assumes 2nd order accuracy for the numerical scheme being used, and so the coefficient g_1 becomes zero. For two different mesh sizes, say h_1 (fine) and h_2 (coarse), two different solutions f_1 and f_2 are obtained. Then a new expression for f_{exact} can be given:

$$f_{exact} = \frac{h_2^2 f_1 - h_1^2 f_2}{h_2^2 - h_1^2} \quad (3.2)$$

Standard Richardson extrapolation also assumes a grid refinement factor $r = h_2/h_1 = 2$, which allows f_{exact} to be simplified into:

$$f_{exact} = f_1 + \frac{f_1 - f_2}{3} \quad (3.3)$$

In this manner, the solution obtained from the fine mesh can be adjusted to more accurately reflect the true solution.

Here it is important to address the two primary limitations of standard Richardson extrapolation, that being the assumption of 2nd order accuracy for the numerical scheme, and the requirement that the grid refinement factor r be equal to 2. In many practical FEM formulations, maintaining a grid refinement of $r = 2$ for several meshes is difficult due to computational cost issues, particularly in cases involving 4-node quadrilateral and 8-node solid elements (like the hinged-cylinder problem used in this paper) where halving the element edge length h results in a fourfold and eightfold increase respectively in the number of elements needed for coverage of a given model geometry.

To address this issue, a more generalized form of standard Richardson extrapolation is available for grid refinement factors r and orders of accuracy p other than 2 (Roy 2005). For a generalized p -th order accurate numerical scheme:

$$f_{exact} \cong f_1 + \frac{f_1 - f_2}{r^p - 1} \quad (3.4)$$

This greatly enhances the flexibility of the Richardson extrapolation approach for practical FEM problems. However, it introduces the issue of solving for the observed order of accuracy p . For most problems where the exact solution is not known, three solutions using different meshes are needed to calculate the observed order of accuracy:

$$p = \frac{\ln\left(\frac{f_3 - f_2}{f_2 - f_1}\right)}{\ln(r)} \quad (3.5)$$

with f_3 being the solution for the most coarse grid spacing. This assumes uniform mesh refinement, that is $r = h_2/h_1 = h_3/h_2$. For cases where the uniform refinement factor requirement cannot be met ($r_{12} \neq r_{23}$), an alternate expression is available (Roache 1998):

$$\frac{f_3 - f_2}{r_{23}^p - 1} = r_{12}^p \left(\frac{f_2 - f_1}{r_{12}^p - 1} \right) \quad (3.6)$$

where the observed order of accuracy p can be found iteratively.

Roy (2005) provides a framework for expressing the discretization error using generalized Richardson extrapolation. With f_{exact} found as described previously, the relative discretization error (RDE) can be expressed as:

$$\text{RDE}_1 = \frac{f_1 - f_{\text{exact}}}{f_{\text{exact}}} \quad (3.7)$$

which can then be restated as:

$$\text{RDE}_1 = \frac{f_2 - f_1}{f_{\text{exact}} (r^p - 1)} \quad (3.8)$$

Successive mesh solutions are used to provide an indication of whether the asymptotic convergence region has been reached. This is done by noting that within the asymptotic convergence region, the RDE should go down as a function of $1/r^p$. It is worth mentioning that the RDE_i is affected not only by the relative difference between the exact solution and the i -th mesh solution, but also by the order of convergence p , as well as the grid refinement factor r .

In the model verification exercise presented in this study, the simplified cylinder model mentioned previously is analyzed using the commercial finite element code LS-Dyna, a general-purpose explicit transient code designed for analysis of high-frequency, short-duration events involving impact and contact. As mentioned previously, the computational time required for explicit analysis is largely driven by the time step used, which must be smaller than the natural

period of every element in the model. This increased importance of the highest frequency element in the model forces a change in thinking when considering the computational expense of a particular mesh resolution. Whereas in implicit time integrations the overall number of degrees of freedom (a function of the number and types of elements used) governs the overall model run times, with explicit integration schemes the additional consideration of the smallest elemental dimension (and the density and stiffness of that element) must be included as well.

This discussion of the nature of explicit transient finite element codes is important in relation to the Richardson extrapolation approach outlined above. The assumptions upon which it is premised mean that extreme care should be taken when applying Richardson extrapolation to fluid-structure impact problems. Along these lines, Stewart et al. (2006) discuss the difficulty of applying Richardson extrapolation to transient analysis problems. Their work showed the difficulty of achieving asymptotic convergence in problems involving contact, friction, and other dynamic issues often encountered in practical engineering problems. Their study used the hourglass energy as an indicator of the discretization error in a particular mesh. Hourglass modes are frequently encountered in explicit finite element analysis due to reliance on reduced-order shell elements, creating spurious oscillations that must be countered with an appropriate damping scheme.

3.3 LS-Dyna Fluid-Structure Impact Methodology

The fluid-structure impact formulation within LS-Dyna is conducted using an Arbitrary Lagrangian-Eulerian (ALE) approach. The structural geometry to be discretized consists of a 3-in. diameter cylinder, with a 10:1 length-to-diameter ratio. The thickness of the cylinder wall is 0.025 in., and the two circular end caps are 0.25" thick. The fluid region consists of a

rectangular solid 6" in width, 4" in depth, and 32" in length. The hinged end of the cylinder is aligned with one end of the rectangular fluid region, leaving 2" of clearance between the forward end of the cylinder at impact and the boundary of the fluid region. The height of the cylinder hinge is adjusted so that when in the horizontal position, the leading edge of the cylinder is perfectly aligned with the fluid surface. This configuration is thought to maximize slamming loads as a result of impact. In order to minimize the amount of simulated run time prior to impact, the cylinder is rotated only 1° from horizontal. The symmetry condition is exploited so that only half of the described geometry is actually modeled. Appropriate nodal constraints are placed on the boundary nodes of the cylinder to ensure the validity of the symmetry assumption. Fig. 3.1 shows a schematic of the hinged-cylinder geometry used in this study.

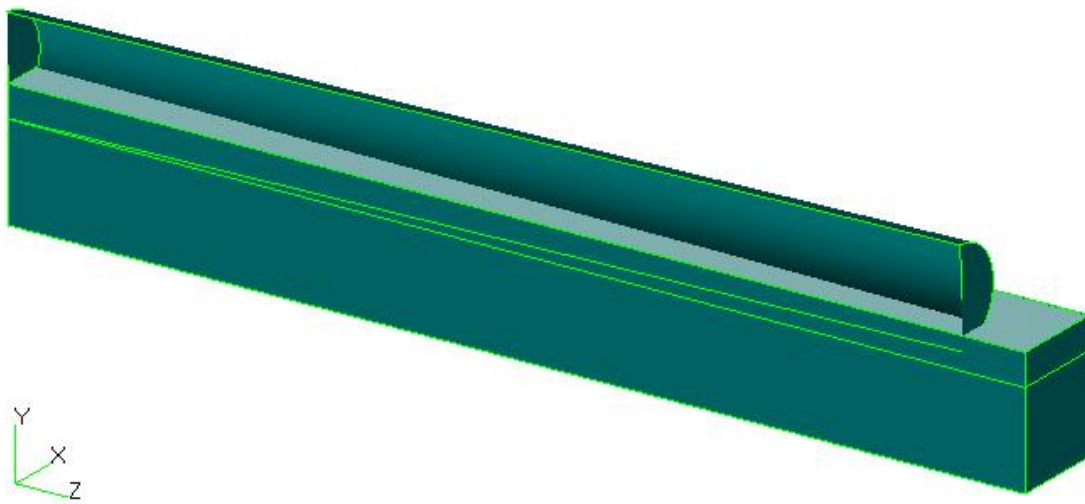


Fig. 3.1 Hinged-cylinder FEM geometry schematic

3.3.1 Independent Mesh Refinement

Roy (2005) discusses mesh refinement along independent coordinate axes in space. Here we will apply this strategy for the independent meshes of the fluid-structure impact analysis:

$$f_k = f_{\text{exact}} + g_{Lag} (\Delta Lag_k)^p + g_{Eul} (\Delta Eul_k)^q + \text{H.O.T.} \quad (3.9)$$

With p and q being the order of accuracy in the Lagrangian mesh and Eulerian regions, respectively. This approach appears to be well-suited for the independent fluid and structural meshes used in this study. For example, if one increases the resolution in the Lagrangian structural mesh only by a factor of r_{Lag} , then instead of solving for f_{exact} , one must solve for $f_{\text{exact}, Lag}$:

$$f_{\text{exact}, Lag} = f_1 + \frac{f_1 - f_2}{r_{Lag}^p - 1} \quad (3.10)$$

With the $g_{Lag}(\Delta Lag)^p$ error term from above given by:

$$g_{Lag} (\Delta Lag)^p = \frac{f_2 - f_1}{r_{Lag}^p - 1} \quad (3.11)$$

It follows then that the Eulerian region could also be refined while the Lagrangian mesh is fixed, and a third solution f_3 obtained. Then the $g_{Eul}(\Delta Eul)^q$ term could be solved for:

$$g_{Eul} (\Delta Eul)^q = \frac{f_3 - f_2}{r_{Eul}^q - 1} \quad (3.12)$$

Comparing the sizes of these two error terms will indicate which mesh has a greater influence on the total discretization error. This formulation for independent mesh refinement gives us a method for systematically analyzing the discretization error contributions from the Lagrangian and Eulerian regions. In this exercise, we use a constant grid refinement factor of $r = 2$. Also, the refinement is carried out uniformly over the entire geometric domain.

Adaptive mesh refinement is the process by which only certain areas of interest within the finite element model are refined. Various methods are available for conducting adaptive mesh refinement, including approaches for explicit nonlinear, dynamic problems (see for example (Radovizky and Ortiz 1999; Mathisen et al. 1999; and Bessettee et al. 2003)). Such

methods typically involved discretization error estimation for all elements within the model based on several refinements. Areas of the structure showing higher levels of discretization error are refined further, while the rest of the model is left unrefined. The idea behind adaptive mesh refinement is to optimize model analysis time by not increasing the number of degrees of freedom more than is necessary. However, it should be noted that for explicit time integration codes many of the computational efficiency gains from adaptive refinement may be canceled out by smaller time steps. Also, practical considerations pertaining to the geometry of the problem can pose difficulty for adaptive refinement approaches, such as skewed elements with extreme aspect ratios. Therefore, in this study, adaptive approaches are not considered.

3.3.2 Richardson Extrapolation Implementation

This particular model uses 4-node quadrilateral shell elements to model the cylinder wall, 3-node triangular shell elements for the thick end caps, and 8-node solid elements for the Eulerian fluid region. Since each mesh can be resolved independently, different combinations of mesh resolutions (e.g., a fine cylinder mesh coupled with a more coarse fluid mesh) could be paired and analyzed. For the discretization exercise presented here, 13 different combinations of fluid and structural meshes are analyzed. Due to extremely long run times, the 4th refinement of the cylinder mesh is run only once in combination with fluid mesh #4. Table 3.1 summarizes the details of the respective mesh resolutions, with the number of elements and element edge lengths specified. It should be pointed out that the values in Table 3.1 refer only to the cylinder wall, comprised of 4-node quadrilateral shells. Additional shell elements are needed for the end caps, and these are modeled with triangular shell elements so that the element governing the time step remains within the cylinder wall and does not increase overall run times.

Table 3.1 – Mesh details for hinged cylinder discretization exercise

Mesh Index	Cylinder Wall	Fluid Region
1	$h = 0.5236$ in 513 elms	$h = 1.0$ in 384 elms
2	$h = 0.2618$ in 2,052 elms	$h = 0.5$ in 2,688 elms
3	$h = 0.1309$ in 8,208 elms	$h = 0.25$ in 21,504 elms
4	$h = 0.06545$ in 32,832 elms	$h = 0.125$ in 172,032 elms

Note also that for this mesh refinement exercise, a grid reduction factor of $r=2$ is used throughout the problem domain. Fig. 3.2 shows selected meshes analyzed as part of this study.

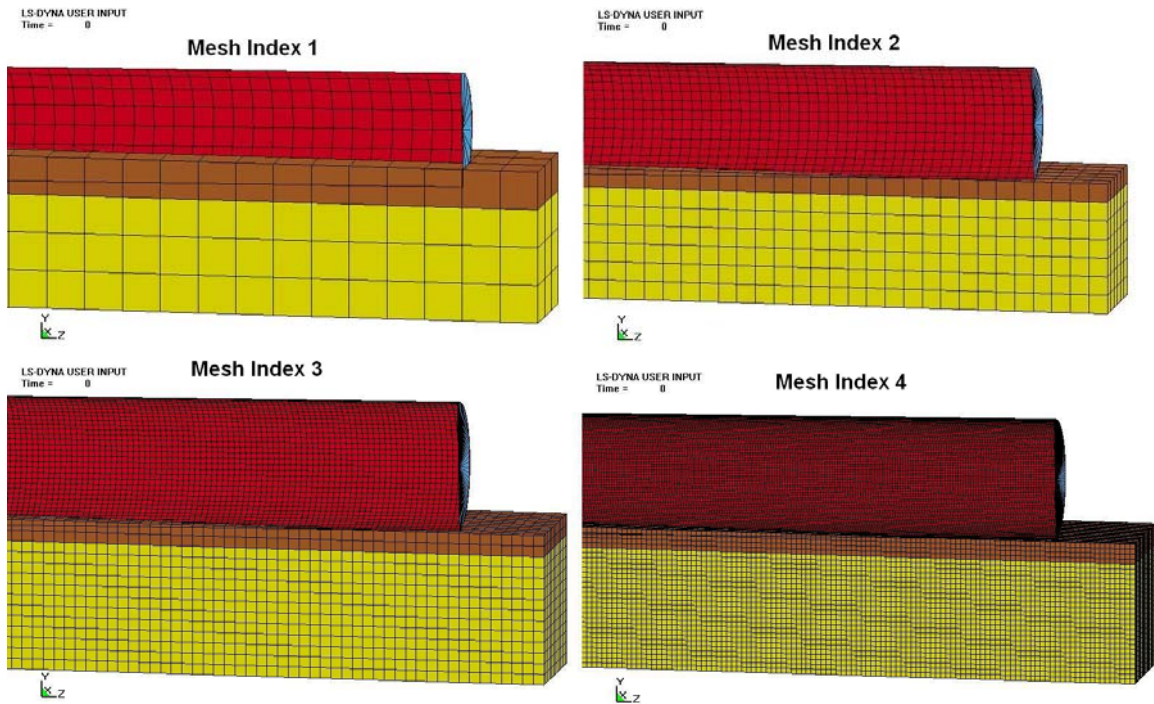


Fig. 3.2 – Selected meshes from discretization error exercise

Note also that Fluid Region Mesh 1 contains 1" of void region depth above the free fluid surface, while subsequent meshes contain only 0.5" of void region. This is done for computational savings, since initial simulations showed that while contributing to the overall analysis time, these void elements had negligible effect on the model results. Since the grid reduction factor was held at $r = 2$ throughout, in practical terms, this means that each refined mesh contains 4 times as many shell elements, and 8 times as many solid elements as the previous mesh.

3.3.3 Finding an Error Estimator

Stewart et al. (2006) present a very clear example of the care which should be used when using mesh refinement as a discretization error indicator for explicit, time-dependent problems. For their work, it was found that an iterative contact algorithm used to generate the contact forces for screw failure was heavily dependent upon the mesh, and that convergence of various quantities of interest was difficult to obtain. Specifically the authors looked at the deflection to failure (DTF) quantity output by the finite element code as well as the internal and kinetic energy present within the system.

In this study a similar approach is adopted, and for each mesh realization the output quantities to be analyzed include the rigid-body displacement (RBD) of the cylinder wall, and the cumulative kinetic and internal energy of the cylinder wall and fluid region. The eventual quantity of interest, the effective surface stress, will be shown as well. Using the independent mesh formulation described earlier (Eqs. 3.9-3.12), the results of the simulations conducted with the various refinement levels are examined. Fig. 3.3 shows the RBD of the cylinder wall for various refinement levels of the Lagrangian mesh defining that wall. The Eulerian region mesh is held constant at level 3 (see Table 3.1).

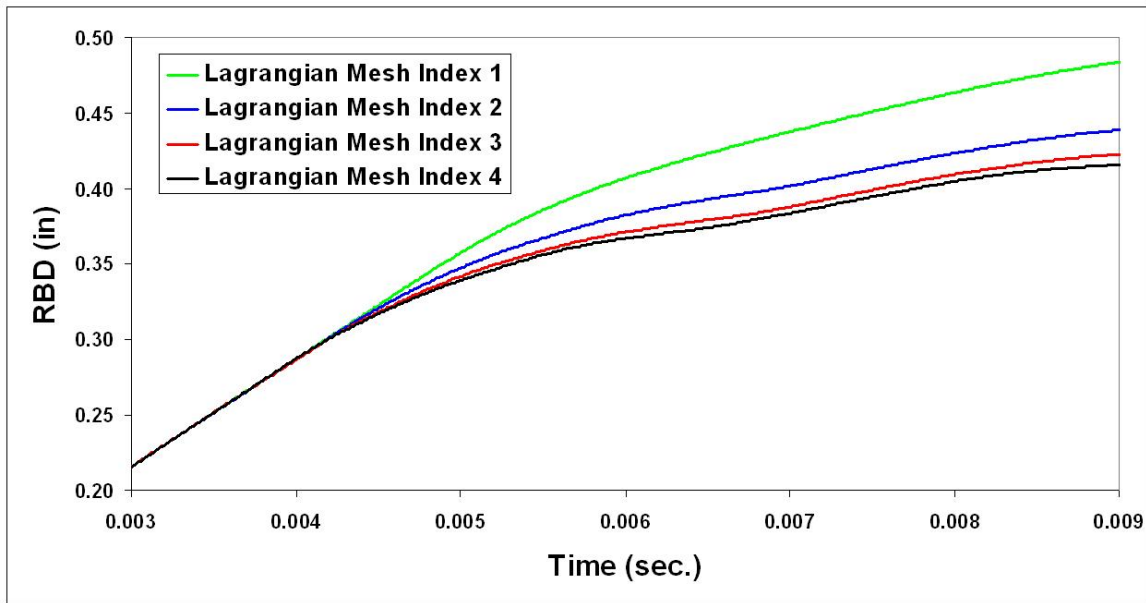


Fig. 3.3 – Rigid-body displacement of cylinder wall with Lagrangian mesh refinement; Eulerian mesh index held at 3

One can see from the plot that the RBD is nearly constant for all four meshes prior to impact with the fluid surface (just after 4.0 msec.) and that after impact the predictions for RBD decrease with the element size. A simple visual inspection would seem to indicate that the curves are converging with increased mesh resolution, and the transient nature of these problems presents an interesting opportunity to view the observed order of accuracy p for the RBD quantity as a function of time. Since four different mesh realizations were solved, two different values for p can be computed. Fig. 3.4 shows p for the RBD of the cylinder wall varying with time following the impact of the cylinder with the fluid surface.

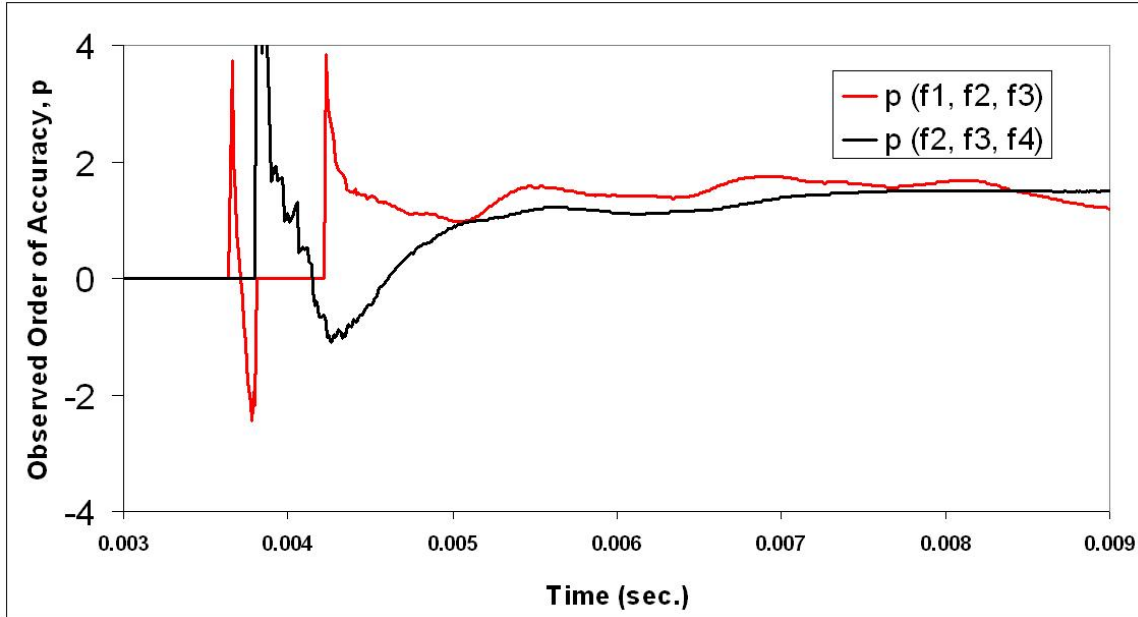


Fig. 3.4 – Observed order of convergence for RBD of cylinder wall following impact

Looking at Fig. 3.4, it is obvious that p varies significantly during the course of this analysis. Of particular note is the manner in which p diverges drastically, taking on negative values, at the instant of impact with the fluid surface. This is the most critical time of the analysis in terms of desired accuracy, and the behavior of p suggests that the RBD quantity is not within the asymptotic range during impact for this set of mesh resolutions. Though p does appear to settle to about 1.5 eventually, the RBD values post-impact are of little interest since the peak stresses will be induced near the instant of impact. So even though the RBD curves in Fig. 3.3 were smooth and appeared to be converging, it is clear that for this impact problem, even the very general quantity of RBD (which is expected to be smooth since it is averaged over the entire cylinder wall), is not within the asymptotic range.

Fig. 3.5 also shows the RBD with time for the cylinder wall, this time with the Lagrangian mesh held constant at level 3 (see Table 3.1), while the Eulerian mesh is refined.

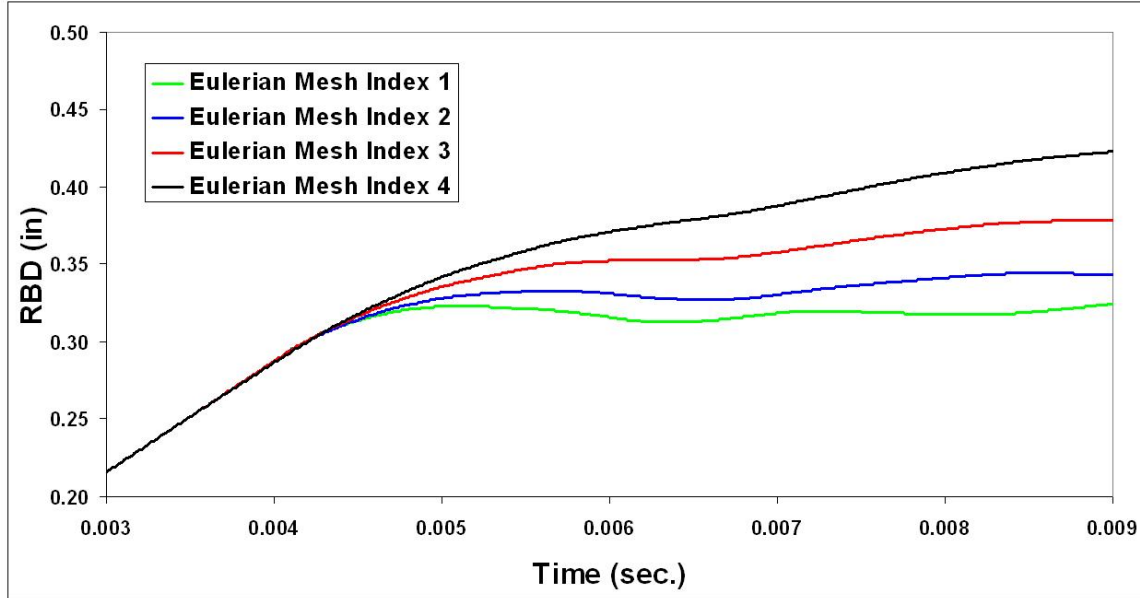


Fig. 3.5 – Rigid-body displacement of cylinder wall with Eulerian mesh refinement; Lagrangian mesh index held at 3

Comparing to Fig. 3.3, it appears that in this case the RBD increases with mesh refinement. Note the similarity of the Eulerian Index 4 curve to the Lagrangian Index 4 curve in Fig. 3.3. Once again, visual inspection seems to indicate smooth, converging values for RBD, however if one were to plot p for this series of mesh refinements as was done in Fig. 3.4, one would see similar behavior.

Notice that in this exercise we are attempting to quantify the error terms $g_{Lag}(\Delta Lag)^p$ and $g_{Eu}(\Delta Eu)^q$ described earlier in Eqs. 3.11 and 3.12, respectively, for independent mesh refinement with the RBD being the quantity of interest. The idea is to achieve asymptotic convergence for global quantities before moving onto specific locations on the structure. However, the results thus far seem to indicate that even the global quantity of RBD does not converge with mesh refinement at the moment of impact.

Next several non-transient output quantities are considered, specifically the time-integrated kinetic and internal energy of the cylinder wall and fluid region. This approach returns single values for each analysis, with the expectation that these even more generalized values might converge asymptotically. Fig. 3.6 shows the time integrated kinetic energy for the cylinder wall and fluid region for various mesh refinements.

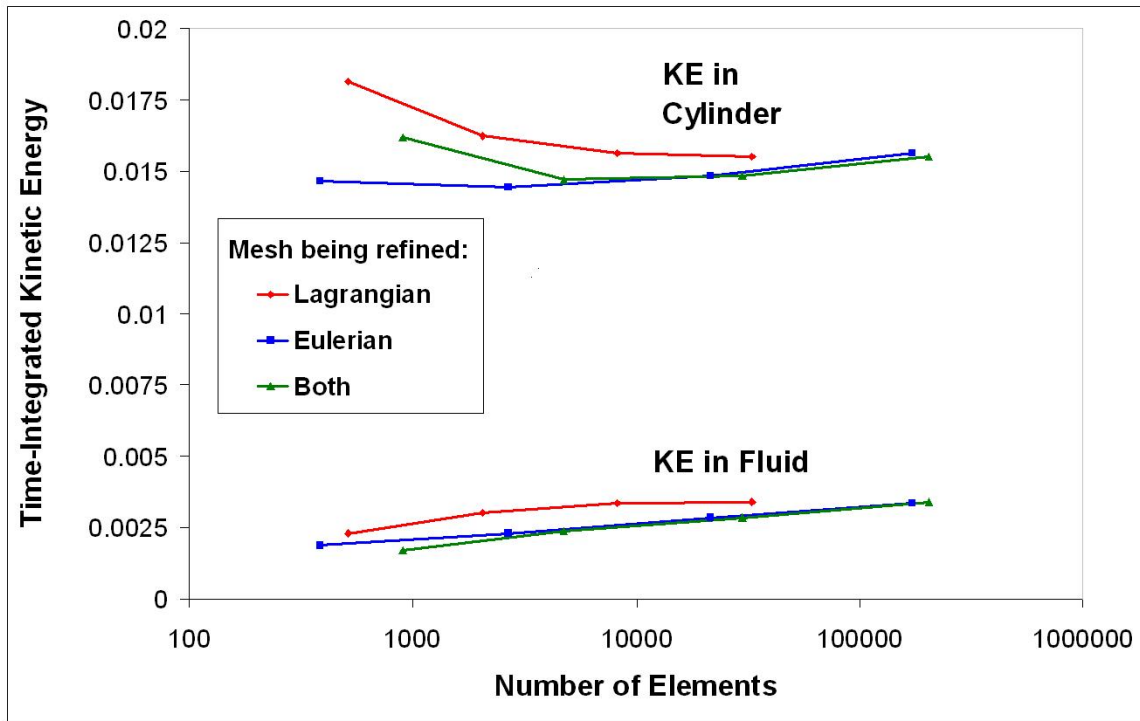


Fig. 3.6 – Time-integrated kinetic energy for cylinder wall and fluid

For the red curves, the Eulerian region was held at refinement index 4 (see Table 3.1) as the four Lagrangian meshes were solved. Likewise, for the blue curves the Lagrangian mesh was held at index 3. The x-axis shows the log-scaled number of elements in each mesh over the course of the refinements. It can be seen from Fig. 3.6 that with the possible exception of the Lagrangian refinement curves, convergence does not appear to be achieved for the time-integrated kinetic

energy. Similar behavior is observed for time-integrated internal energy: though definite trends are present with mesh refinement, there does not appear to be clear asymptotic convergence

These results give the reader a sense of the difficulty of quantifying discretization error for complex, transient finite element problems. Here we have shown very general results for both transient and cumulative outputs, and yet convergence does not appear to be obtained. Mesh refinement does not appear to be having the desired effect, despite models with over 200,000 elements. One indication concerning the cause of this problem can be seen in Fig. 3.7, where a stress history plot of several mesh realizations is shown.

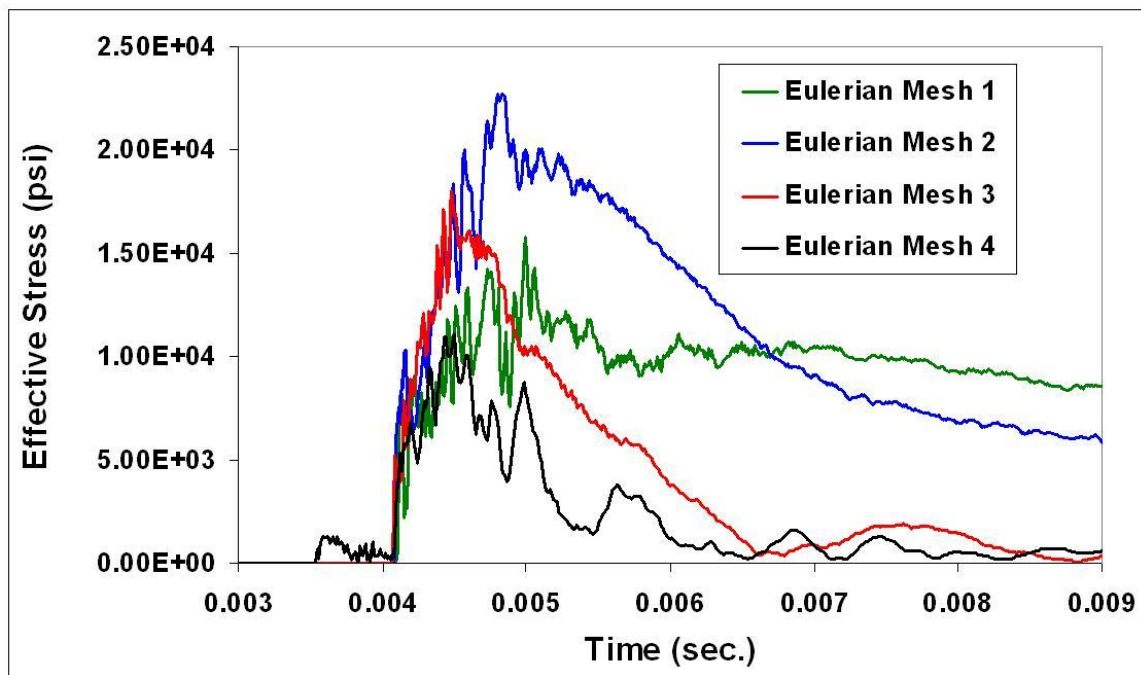


Fig. 3.7 – Stress history for Eulerian refinement using Lagrangian mesh 3

Each curve in Fig. 3.7 is taken from the same location along the leading edge of the impacting cylinder. One notices significant differences from curve to curve, depending upon the refinement level of the Eulerian region. Note that just prior to impact, the curve representing

Eulerian mesh 4 shows a small disturbance. None of the other curves show this characteristic. This curve also happens to be the only curve for which the Eulerian region is more finely meshed than the Lagrangian (cylinder) mesh. These results imply that when the structural mesh is under-resolved (i.e. larger element edge lengths) relative to the Eulerian region, the coupling algorithm employed by LS-Dyna does not reconcile the two meshes in a realistic manner.

The plot in Fig. 3.8 provides further evidence that coupling discrepancies arise when the Lagrangian structural mesh is under-resolved relative to the Eulerian mesh.

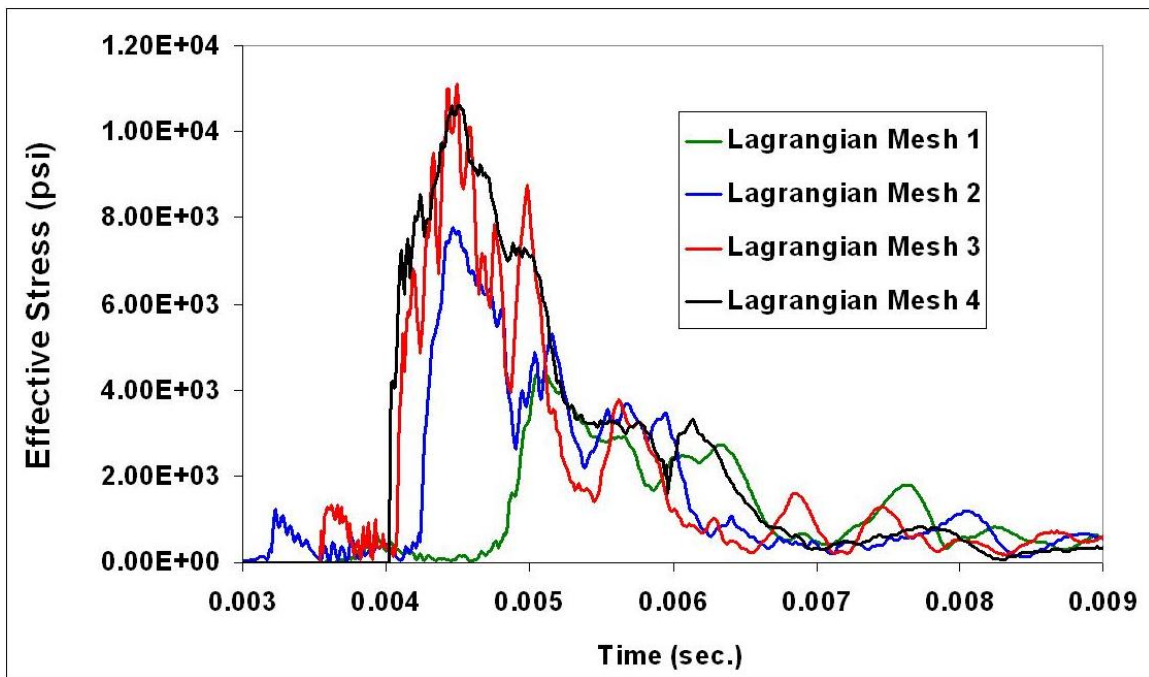


Fig. 3.8 – Stress history for Lagrangian refinement using Eulerian mesh 4

Note here that all curves show a disturbance prior to full impact, except for the curve for Lagrangian Mesh 4. As before, this curve is the only one for which the Lagrangian edge lengths are finer than the Eulerian elements. Also, post-analysis animations of the cylinder impact provide still further evidence of this, showing a distinct lack of agreement between the moving

cylinder and the fluid surface for cases where the cylinder is under-resolved relative to the fluid mesh. Fig. 3.9 shows an example of this behavior.

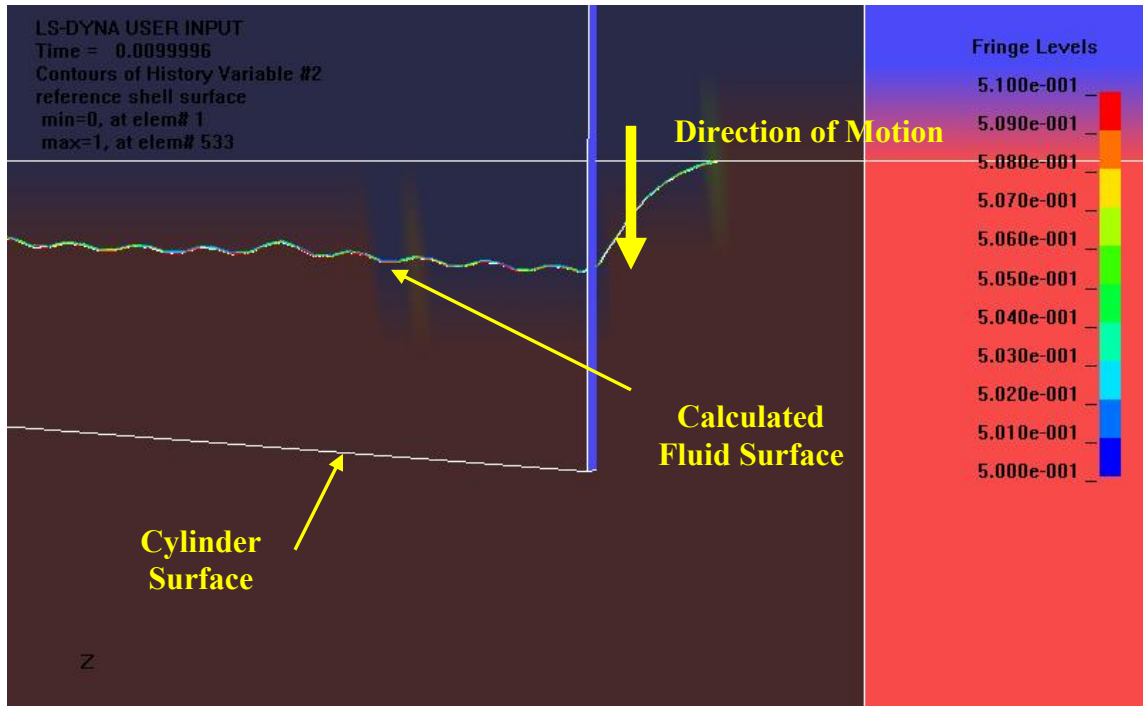


Fig. 3.9 – Still image from LS-Dyna animation showing poor coupling

When the cylinder is finely discretized, the moving fluid boundary maintains close contact with the cylinder, even for instances where the fluid region is very coarsely meshed. This makes the point that finite element analysis of transient, complex problems involving contact and/or multiple mesh regions must depend on internal, iterative algorithms to perform the analysis. The results shown here imply that such procedures are highly mesh-dependent, not only on the resolution of the respective meshes, but the resolutions relative to one another.

3.4 Summary and Conclusions

This chapter has presented investigations of approaches to quantify the discretization error for a class of finite element problems concerning fluid-structure impact. Several different output quantities are observed in an effort to determine whether the asymptotic convergence region has been reached. The results show a lack of convergence, even for general, global output such as rigid-body displacement and time-integrated internal energy. Output quantities of practical interest, such as effective stress history, show significant variation, both in terms of magnitude and overall curve shape.

Careful inspection of the various analyses points to the iterative coupling algorithm used by the LS-Dyna code to reconcile the fluid boundary with the moving structural mesh as one likely reason for the lack of convergence. Particularly, poor coupling behavior (and therefore wildly varying stress data) is observed when the structural mesh is under-resolved (i.e., larger element edge lengths) relative to the fluid mesh. For now, the results indicate that increased model resolution is usually preferable, provided the structural mesh does not become under-resolved relative to the fluid region. In each simulation, the required time step needed for the explicit formulation is governed by structural elements in the cylinder. Therefore the overall run times are most sensitive to refinement in the structural mesh. Lagrangian Mesh 4 pushes the limits of the available computational capabilities (single desktop PC, 2.4 GHz processor, 2.0 GB RAM), requiring 30+ hours of analysis time for only .01 seconds of simulated time. Therefore any subsequent mesh refinement will likely take place using a grid reduction factor less than the $r = 2.0$ used throughout this exercise.

Adaptive approaches have not been investigated for this problem due to a variety of practical considerations, namely the skewed aspect ratios that result for elements away from the

refined regions. Another approach for managing numerical uncertainty in transient analyses involving contact is proposed by Stewart et al. (2006). Absent model output that appears to converge with successive grid refinements, their proposed framework calls for mesh refinement until the mesh sensitivity (not necessarily asymptotic convergence) for some quantity of interest is within the error bounds of a corresponding experimental procedure. Chapter 4 will present details of the experimental procedure used in this study, but here a preliminary application of this approach is taken using the LS-Dyna prediction obtained using mesh index 4 for both the Lagrangian and Eulerian domains. The comparison is plotted in Fig. 3.10.

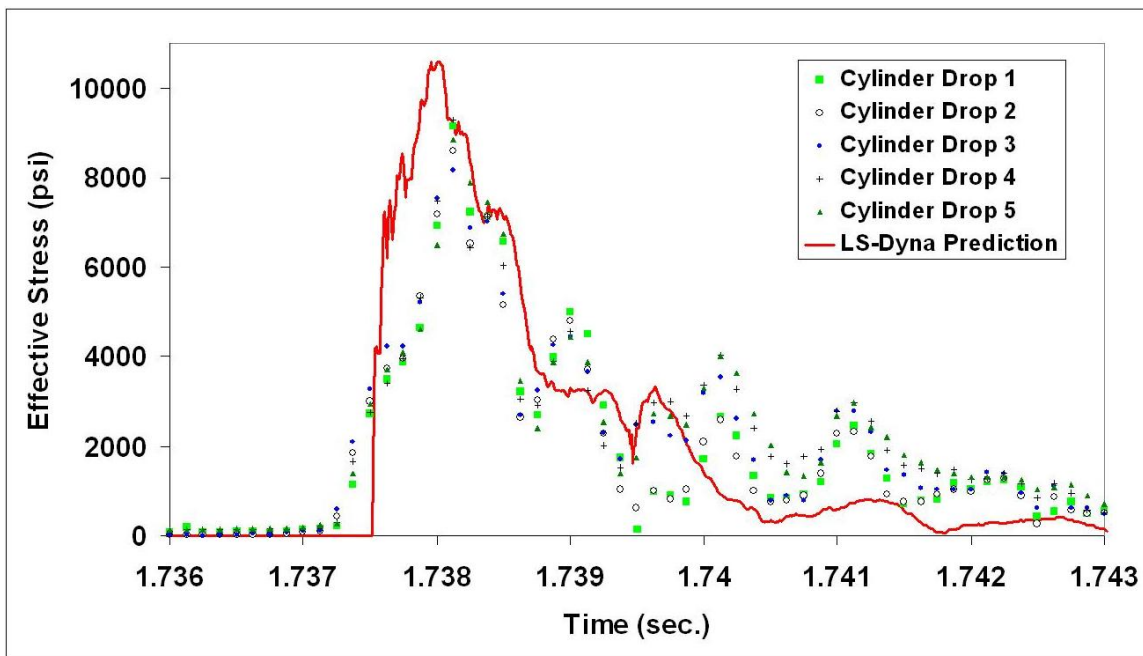


Fig. 3.10 – Comparison of LS-Dyna prediction using mesh index 4 to experimental data

Though the overall form of the stress history curve predicted by LS-Dyna roughly matches the trends recorded from five separate experimental cylinder drop tests, the model prediction overestimates the range of peak stresses at the measured location on the cylinder wall. However,

it is also clear that the increased model resolution used to obtain the LS-Dyna prediction in Fig. 3.10 is in much better agreement with the experimental test data than those produced by the coarser meshes (see Figs. 3.7 and 3.8). That said, the peak stress predicted by the LS Dyna model using Lagrangian mesh index 3 and Eulerian mesh index 4 (black curve in Fig. 3.7; red curve in Fig. 3.8) is seen to compare similarly to the test data as the prediction shown in Fig. 3.10. The successive LS-Dyna predictions for peak stress are similar (and much closer together than previous runs with coarser grids), and are also in proximity to the range of measured peak stresses in laboratory testing. This indicates that additional refinements to the finite element mesh will likely not improve the accuracy of the prediction enough to warrant the considerable increase in computational expense. Recall that the time needed to run a single analysis using mesh index 4 for both model domains is already on the order of 30 hours with the available resources.

Engineers engaged in risk and reliability analysis often confront complicated numerical models like those involving fluid-structure interaction presented here. The issue of discretization error in model verification is therefore of importance. Here we have shown some of the practical considerations which must be made when attempting to quantify this error for fluid-structure impact. The issue is complicated significantly when one includes random variation into the input parameters of the problem, since discretization error also then becomes random. The work presented here shows that for complex, transient numerical schemes often utilized for fluid-structure impact analysis, arbitrary mesh refinement does not necessarily result in decreasing discretization error. Estimates for numerical error in such analyses based upon traditional extrapolation procedures should therefore be used with caution.

CHAPTER IV

EXPERIMENTAL VALIDATION OF FLUID-STRUCTURE IMPACT MODEL

4.1 Introduction

This chapter presents an investigation into suitable model validation procedures for fluid-structure impact analysis, with the goal of increasing confidence in numerical models of the SRB splashdown problem. Validation is defined as the process of determining how accurately a chosen model represents the corresponding real-world system. Validation of any model requires real-world data from either field or experimental measurements. However, in the case of the SRB splashdown event, flight data concerning stress and displacements are not available (Mitchell et al. 2003), and full-scale experimental data is prohibitively expensive to obtain. Therefore, in this study we conduct validation efforts concerning a general fluid-cylinder impact problem scenario with reduced scale and structural complexity. Increased confidence gained from this exercise must be extrapolated into the domain of the SRB splashdown problem, and a proposed methodology for doing so will be discussed in Chapter 6.

The experimental setup needed for this validation exercise requires that the same general physics as those governing the SRB splashdown sequence be captured using components of a manageable scale and cost. It is worth noting that the experimental facilities and resources used in this study are relatively modest, though every effort has been made to keep the physics of the experimental system as close to the real-world scenario as possible. Along these lines, an experimental rig using a thin-walled cylindrical structure impacting a free water surface was

constructed and used to conduct a validation exercise with the finite element fluid-structure impact modeling approach discussed in Chapter 2.

4.2 Experimental Setup

As described in Clayton and Craft (1995), the SRB splashdown sequence consists of four phases: 1) initial entry, 2) maximum penetration, 3) cavity collapse, and 4) rollover and slapdown. At least one flight data set obtained from accelerometers shows the slapdown portion to be the critical phase (McFadden 1999), with large loadings placed on the structure as it breaks the free water surface and its rotational inertia is suddenly arrested. Therefore the investigation into the design of a suitable experimental setup was based on the assumption that slapdown is indeed the critical phase of the SRB splashdown sequence.

There are several considerations to be made in designing the experimental setup: 1) the dimensions of the aluminum cylinder, 2) the drop mechanism, 3) the dimensions of the required water tank, and 4) the data acquisition system and physical quantities to be measured. Each of the various aspects has to be weighed simultaneously, since a decision concerning any one feature also affected the range of options available for the other two.

4.2.1 Aluminum Cylinder

It should be stated at the outset that although efforts have been made in this study to keep various proportions of the experimental aluminum cylinder similar to those of the full-scale SRB, this work should not be interpreted as an attempt at scaled physical modeling of the SRB splashdown event. Such an effort would be prohibitively expensive given the available resources. However, it is believed that the laboratory data can be used to perform validation on a

finite element model of the hinged cylinder impact, and thereby increase confidence in the finite element modeling approach. Provided the experimental setup captures the same general physics as that governing the SRB impact problem, then it is possible that confidence can also be increased in the finite element model of the SRB splashdown event. This concept is expanded upon in Chapter 6.

To keep the experimental setup manageable in terms of size and cost, the dimensions of the experimental rig are kept relatively small. Tests need to be performed in an indoor laboratory setting, without benefit of heavy equipment or machinery. The primary dimensional relation factoring into cylinder selection is the thickness-to-radius (t/r) ratio. In order to achieve the desired splashdown characteristics, balance is needed between the total mass and structural stiffness of the cylinder. If the t/r ratio is too small, the cylinder will not register a significant structural response at impact owing to its lack of momentum. The cylinder will stop abruptly at the water surface, but the shock effect of splashdown will be small. Similarly, if the t/r ratio is too large, then the cylinder will break the water surface and not register a significant response owing to its high structural stiffness. During this study, considerable investigation has been done into commercially available thin-walled, seamless aluminum cylinders, however very few options were found due to the limited practical applications of such cylinders.

A second challenge faced in cylinder sizing was the desire to retain the same 10:1 length-to-diameter ratio seen on the actual SRB. This requirement limited the pool of available options even further, since aluminum cylinders meeting all of the requirements just described are simply too weak to have any practical structural application. Taken together, these issues led to the decision to have the cylinders specially fabricated.

Even with the flexibility offered by specialty fabrication, options for cylinder dimensions are still limited due to the size limits on commercially available sheet aluminum. Specialty-made, seamless aluminum cylinders were beyond the capabilities of the machine shop used for fabrication, and so the decision was made up front to craft the cylinders from widely-available, rolled sheet aluminum. The range of thicknesses considered included sheets of standard 3003 aluminum available commercially at .017", .02", and .025". However, these sheets are only readily available with a maximum edge length of 36", thus limiting the length of cylinders that could be fabricated using them. So that the 10:1 length-to-diameter proportion could be maintained, the final cylinder design called for a length of 30" and a diameter of 3.0". A sheet of each of the three thicknesses mentioned above was procured, and three cylinders were initially fabricated by rolling the sheet around a circular mold. It is not practical to attempt welded seams with aluminum for the thicknesses used here, and so the overlap seam formed down the length of each cylinder was sealed by applying industrial epoxy. Clamps held the assembly together for 24 hours to give the epoxy sufficient time to set. Upon removal from the mold, circular end caps were fitted to both ends of the open cylinder and also affixed with epoxy. The end caps provide needed mass and structural stiffness to the cylinder, and also provide buoyancy to ensure the impact with the free water surface generates a significant structural response..

4.2.2 Drop Mechanism

With the cylinder dimensions established, attention is given to the drop mechanism needed to give the cylinder suitable velocity such that water impact registers a significant structural response. To obtain useful experimental results, the drop mechanism must provide controlled impact conditions, such that the cylinder strikes the water with consistent velocity

(both in terms of magnitude and direction) and reasonably repeatable results are possible. One option includes a dual-release mechanism that supports the cylinder at either end in a horizontal configuration and releases both ends simultaneously. This allows for measurement of the cylinder structural response owing to horizontal water entry. By varying the timing of the two release triggers, the angle of impact can be varied for further experimental readings.

A second option for the drop mechanism is to give the cylinder both horizontal and vertical velocity components in a manner similar to the actual SRB splashdown event. Such a system would require a guide rail of some form down which the cylinder could be propelled before release. The forward velocity of the cylinder at impact would necessitate a larger tank of water due to the increased splash area.

Both of the systems described above present concerns with regards to repeatability of impact conditions and consistency of the measured data. Given the available laboratory facilities, it does not appear feasible to employ a system in which the cylinder experiences actual free fall during the drop tests. In contrast, a system in which the cylinder is merely hinged at one end and allowed to fall over into water shows some immediate advantages. Fig. 4.1 shows a schematic of the proposed experimental assembly. This simplified setup allows for the blunt water impact (i.e. slapdown) believed to be responsible for the damage to the SRB forward skirt to be captured, and it greatly simplifies the drop mechanism. Insofar as the horizontal and vertical velocity components of the SRB at initial impact are translated into rotational inertia leading to the structure breaking the surface during slapdown, reducing the experimental rig down to a single rotational degree of freedom appears to be a suitable course of action.

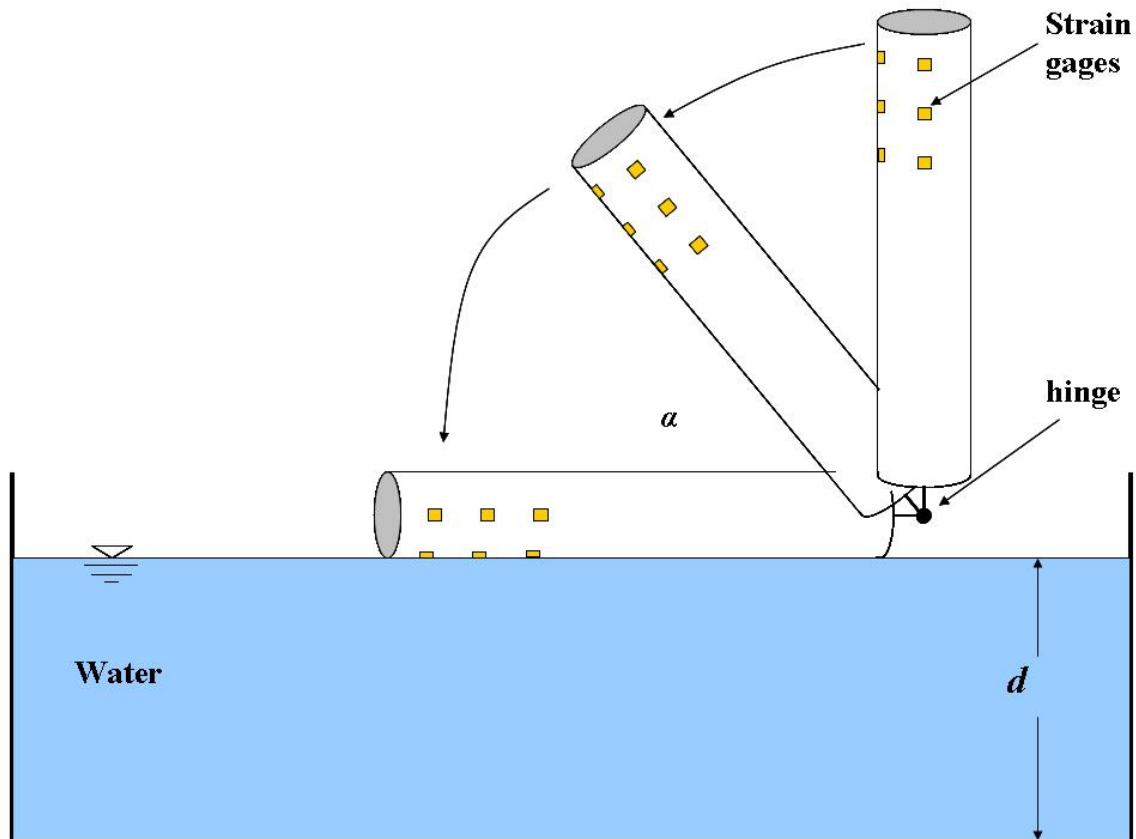


Fig. 4.1 – Experimental testing assembly for cylinder-water impact

Given these considerations, the hinged-end approach is used in order to avoid further complexities that would be needed to give the cylinder horizontal and/or vertical velocity as it breaks the water surface.

The cylinder is attached to a mounting plate via a bolt that goes through the center of the aft end cap. This mounting plate is attached to two extender arms that pivot about a circular horizontal bar 1.5" below the bottom of the cylinder. The horizontal bar is supported at either end by a bracket that is clamped to the side of the holding tank (to be discussed further in the next section).

4.2.3 Water Tank

The water tank used in this study is specially fabricated for this experimental application, since there were no permanent facilities readily available. Given the fair amount of additional equipment involved (cylinders, drop mechanism, data acquisition system), the decision was made to construct a portable tank of manageable dimensions that could be easily placed within the laboratory and quickly filled and drained. The tank needed to be large enough to accommodate the 30" cylinder, but the decision was made to make the tank somewhat larger than required to provide flexibility for any future investigations of a similar nature. The final consideration involved the need to visually observe the impact sequence. Often in experimental work of this nature, a transparent tank wall is used so that the splashdown can be filmed with high-speed cameras for later analysis (see for example Lin and Shieh 1997).

The tank designed for this work was made from 72" × 36" pieces of ½" transparent acrylic. The pieces were cut to construct a tank 72" long, 23" wide, and 24" deep. The pieces were joined together using a solvent which fused the edges together forming a watertight seal. Finally, the tank was placed upon a large plywood platform with rollers underneath. This allowed the entire assembly to be easily moved into and out of position near the laboratory water supply and drain. The tank could be filled to the desired depth of roughly 12" in about 15 minutes using a standard water hose and spigot. One end wall of the tank contained a drain valve, and a connector hose was used at the end of each testing session to run the water directly into the floor drain. Fig. 4.1 shows the experimental setup consisting of the aluminum cylinder, hinged drop mechanism, and acrylic tank.



Fig. 4.2 – Experimental drop tank and hinged cylinder setup

4.2.4 Determination of Impact Velocities

The key parameter of interest in the experimental drop tests is the radial impact velocity of the aluminum cylinder as it breaks the free water surface. To keep this parameter consistent between experimental trials, just prior to release the hinged cylinder is balanced on end in the vertical position so that only a very slight force is needed to cause to the cylinder to fall over into

the tank. This simple approach produces consistent impact velocities without the need for complex release mechanisms.

To confirm this, and to determine the radial impact velocity of the cylinder at the instant of impact, a series of drop tests are conducted with a high-speed video camera capturing a detailed record of the splashdown. The camera is set to record at 1,000 frames/sec. and is focused upon the location of impact within the clear-walled acrylic tank. Using the horizontal axle that supports the cylinder as the center of rotation, single degree markings are indicated on the outside of the tank, and a marking on the cylinder is then used in frame-by-frame analysis to determine the radial velocity. Figs. 4.3a-c show three still frames from one of the recorded drop tests, in which the cylinder is allowed to fall 90° from the original vertical orientation.

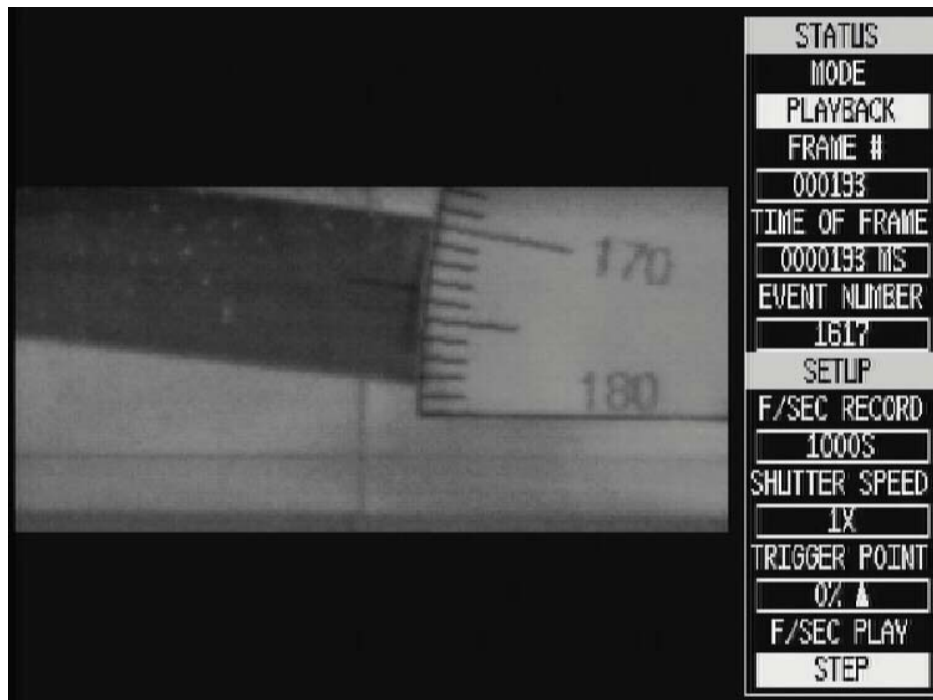


Fig. 4.3a – Still frame from high-speed camera footage

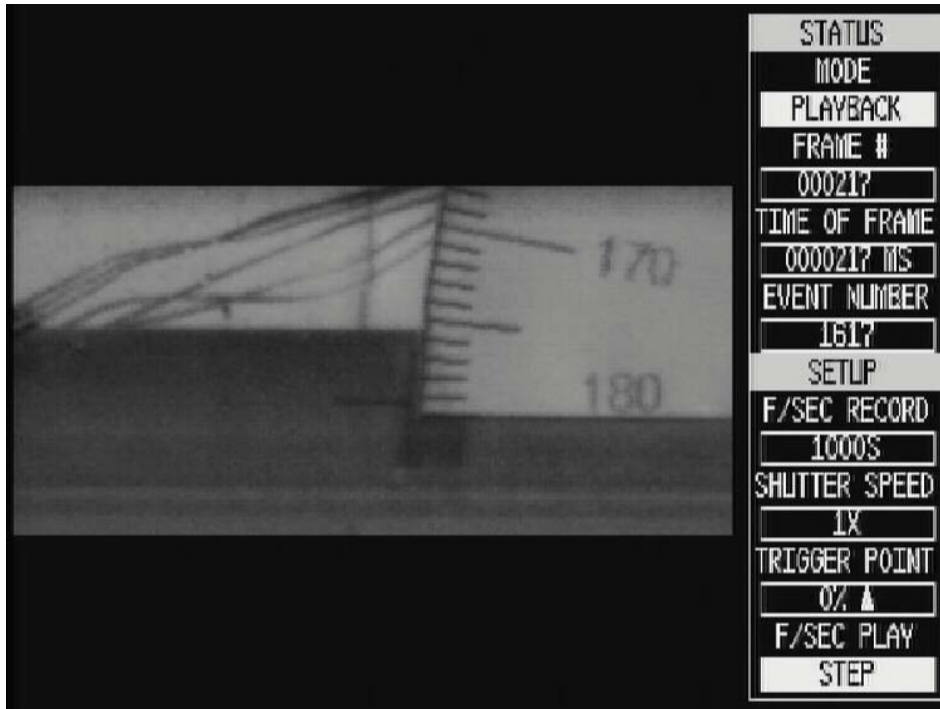


Fig. 4.3b – High-speed camera footage showing instant of water impact

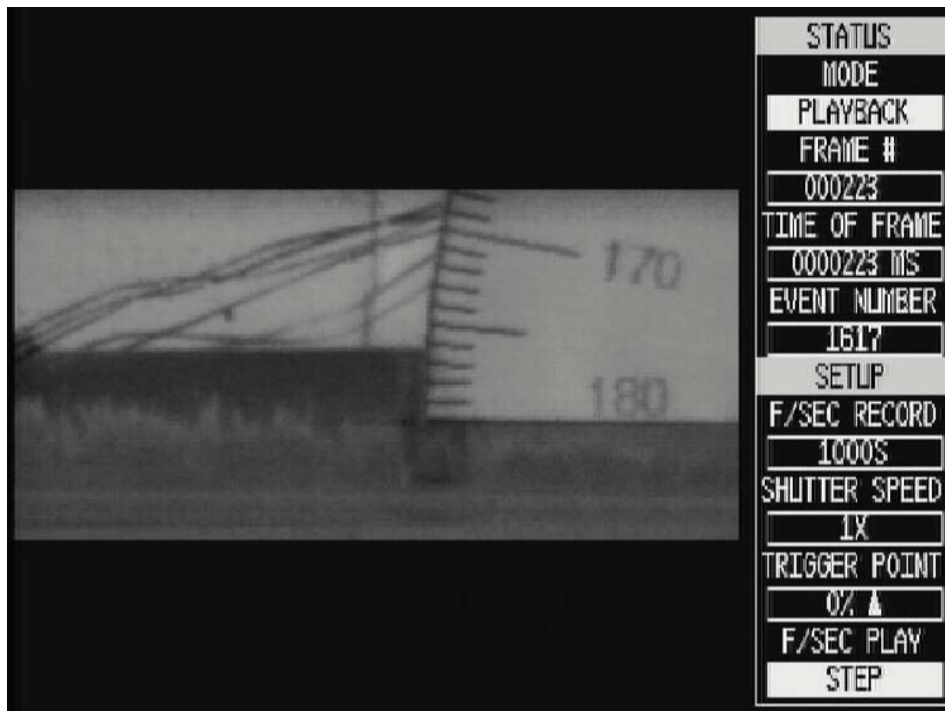


Fig. 4.3c – Impact +6 milliseconds, with water splashing visible

Still frames such as those shown in Figs. 4.3a-c, are used to observe the cylinder from an angle of roughly 10° above the still water level. The time stamps on each frame show that the final 10° is covered in 40 frames, or .04 seconds. Similar tests are conducted for three additional drop angles and the rotational impact velocities computed. Table 4.1 summarizes the nominal rotational velocities of the cylinder at impact for the various release angles.

Table 4.1 – Rotational impact velocities of cylinder from high-speed camera tests

Release Angle from Water Surface	Rotational Velocity at Impact (rad/sec)
90°	4.36
60°	4.15
45°	3.88
30°	3.35

4.3 Data Acquisition System

There are many physical quantities that can be measured directly or inferred from experimental observation. Factors to consider include the usefulness of the measured quantity and taking care to ensure that the necessary instrumentation does not significantly affect the behavior of the system. This can be a real concern in a structural dynamics work such as that described here, since any sensor mass added to the structural system will affect the frequencies of vibration. For this reason, measuring devices such as accelerometers and pressure transducers are not used in this study. Most commercially available options for these devices are large relative to the experimental cylinder, and their use would affect the structural dynamics of the water impact problem causing additional modeling complexities. In contrast, there are many commercial

strain gage options available with insignificant added mass. Therefore, deformation strain is the physical quantity of interest for this experimental study. The next subsections present the details of the data acquisition system (DAS).

4.3.1 Measuring Deformation Strain

The deformation strain in a structural system can be measured at discrete points by affixing strain gages to locations of interest on the structure. The strain gages are actually indirect sensors in that they technically do not record physical deformation of the structural system. Rather, the deformation strain is inferred from slight changes in the electrical resistance of the strain gage caused by physical deformation. The gages are calibrated by the manufacturer and given a gage factor F that relates change in electrical resistance to physical deformation. This change in resistance is detected by measuring the voltage differential in the well-known Wheatstone Bridge configuration. Fig. 4.4 shows a schematic of a Wheatstone Quarter Bridge, in which three electrical resistors and a strain gage R_g are arranged in two parallel circuit arms.

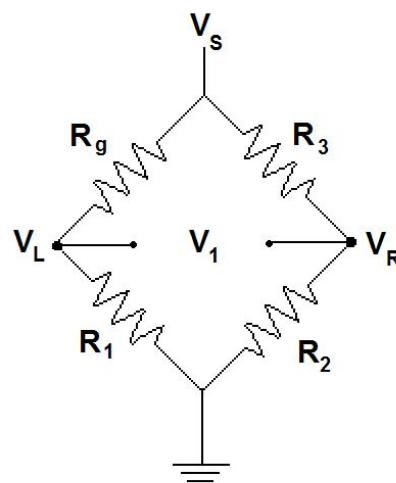


Fig. 4.4 – Wheatstone quarter bridge schematic

The resistors R_1 and R_2 are of known and equal electrical resistance. The strain gage also has a known resistance R_g set by the manufacturer. The final resistor R_3 is a variable resistor and is used to balance the two parallel circuit arms so that the voltage differential V_I between V_L and V_R is zero.

With this balanced circuit, the instantaneous resistance of the strain gage R_g can be computed by monitoring the voltage V_I . Because the circuit arms are in parallel, the voltage drop across each will both be equal to V_S . The voltages V_L and V_R determined from the ratios $R_1/(R_1+R_g)$ and $R_2/(R_2+R_3)$, respectively.

$$V_I = V_L - V_R = \frac{R_1}{(R_1 + R_g)} V_S - \frac{R_2}{(R_2 + R_3)} V_S \quad (4.1)$$

After some consolidating and rearranging, the resistance of the strain gage can be stated as:

$$R_g = \frac{V_S R_1 R_3 - V_I R_1 R_2 - V_I R_1 R_3}{V_I R_2 + V_I R_3 + V_S R_2} \quad (4.2)$$

This resistance is compared to the nominal resistance of the strain gage R_{nom} set by the manufacturer in order to find ΔR . This quantity is related to the inferred deformation strain ε via:

$$\varepsilon = \frac{\Delta R}{R_{nom} F} \quad (4.3)$$

where F is the gage factor set by the manufacturer.

4.3.2 Strain Gages Used for Stress Analysis

For this experimental work, foil strain gages (FSG) are chosen for their ease of use and wide commercial availability. FSGs are the most common type of sensor used in experimental stress analysis. Often, 3-gage rosette configurations are used in practical engineering

applications where the directional alignments of the principal stress components are not known *a priori*. It has been shown (Ueda and Umeda 1997) that the gage factor quantity F is accurate for FSGs even at high frequency measurements exceeding 10 kHz. For a further discussion concerning the suitability of FSGs to impact-induced stress analysis, see Knapp, et al. (1998).

Rosette gages employ three individual strain gages aligned at certain angles relative to one another. For this work, a rectangular rosette pattern was chosen, in which a center gage is set between two additional gages at $+45^\circ$ and -45° , respectively from the orientation of the long axis of the center gage. Each of the three gages comprising the rosette requires a Wheatstone Quarter Bridge in order for the signal to be interpreted and strain recorded. Fig. 4.5 shows a diagram of a rectangular rosette pattern.

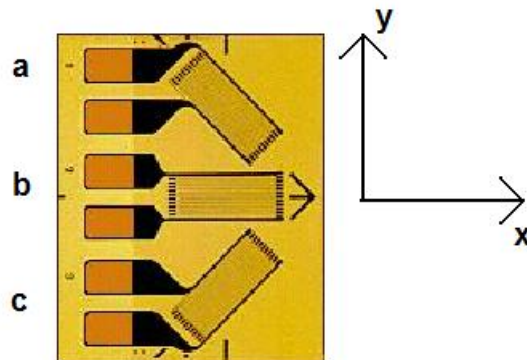


Fig. 4.5 – Strain gage rosette and alignment

Based on the arrangement shown in Fig. 4.5, the x , y , and shear component strains in the surface of the structure can be computed from (Ugural and Fenster, 1995):

$$\epsilon_x = \epsilon_b \quad (4.4a)$$

$$\epsilon_y = \epsilon_a - \epsilon_b - \epsilon_c \quad (4.4b)$$

$$\gamma_{xy} = \varepsilon_a - \varepsilon_c \quad (4.4c)$$

In turn, the x , y , and xy shear stress components can be calculated from generalized Hooke's Law, assuming the plane stress (i.e. $\sigma_z = 0$) condition, using:

$$\sigma_x = 2G\varepsilon_x + \lambda(\varepsilon_x + \varepsilon_y + \varepsilon_z) \quad (4.5a)$$

$$\sigma_y = 2G\varepsilon_y + \lambda(\varepsilon_x + \varepsilon_y + \varepsilon_z) \quad (4.5b)$$

$$\tau_{xy} = G\gamma_{xy} \quad (4.5c)$$

With all z -components of stress $\sigma_z, \tau_{xz}, \tau_{yz} = 0$, and where the z -component of strain ε_z is found from:

$$\varepsilon_z = -\frac{\nu}{E}(\sigma_x + \sigma_y) = -\frac{\nu}{1-\nu}(\varepsilon_x + \varepsilon_y) \quad (4.6)$$

with ν and E representing Poisson's ratio and elastic modulus respectively of the material to which the gage is affixed, and the Lamé constants, shear modulus G and quantity λ , are found from:

$$G = \frac{E}{2(1+\nu)} \quad (4.7a)$$

$$\lambda = \frac{\nu E}{(1+\nu)(1-2\nu)} \quad (4.7b)$$

Finally, the von Mises effective stress is calculated from the stress components:

$$\sigma_{vm} = \left[\frac{1}{2} \left((\sigma_x - \sigma_y)^2 + \sigma_y^2 + (-\sigma_x)^2 + 6\tau_{xy}^2 \right) \right]^{\frac{1}{2}} \quad (4.8)$$

For this work, the effective stress is sought at multiple locations along the hinged cylinder. In keeping with the real-world SRB problem, in which damage is observed in the forward skirt upon splashdown, the gages are all located in the top-half of the hinged cylinder. Efforts have been made to keep the gages as small as possible so that the effects on the structural dynamics of

the system would be minimized. The rosettes selected have an overall length of .222" and an overall width of .42". Fig. 4.6 shows a schematic of the hinged-cylinder with gage locations use in this experimental study.

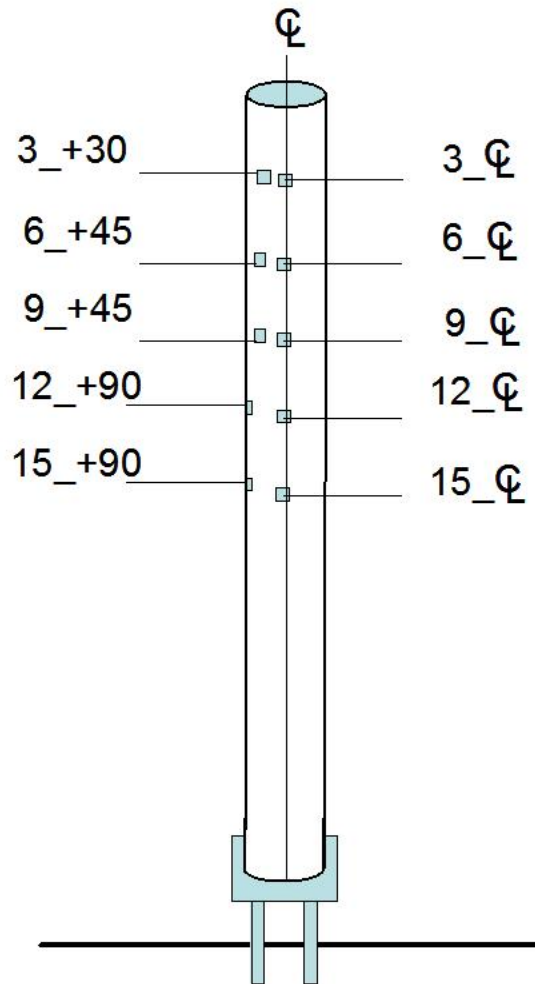


Fig. 4.6 – Cylinder schematic and strain rosette locations

A labeling system has been employed to help indicate the location on the cylinder a given strain reading came from. In Fig. 4.6, the first number in each strain rosette label indicates the distance in inches of the gage from the top of the cylinder. The second part of the label indicates whether the gage is located on the cylinder center line (CL), or some number of degrees about the

circumference from the center line (+30, +45, or +90). A third term in the label (not shown in Fig. 4.6) is used to indicate which of the three individual gages in the rosette is used to record the signal. The center gage (gage *b* in Fig. 4.5) is labeled +90, while gages *a* and *c* are labeled +45 and +135, respectively. These latter numbers indicate the orientation of each gage relative to the cylinder center line.

Affixing of the strain rosettes to the cylinder is a crucial step in the experimental setup, since failure to achieve a true seal with the aluminum surface could result in erroneous values for strain. The first phase of the process involves cleaning the aluminum of any contaminants or blemishes which might prevent proper adhesion. The target location is smoothed with sandpaper of increasing grit to produce a smooth surface, and solvents are used to further clean the cylinder surface of any residue. Next a neutralizing agent is used to help ensure that the bonding agent achieves a full seal. The rosette is placed face-up on a piece of clear cellophane tape, which is then carefully aligned on the cylinder so that the center gage (gage *b* in Fig. 4.5) is aligned with the circumferential axis. A drop of solvent is placed upon the rosette backing, and then the tape is pressed firmly in place and held for several minutes. Careful removal of the tape leaves the bonded gage affixed to the cylinder surface.

In this experimental work there is an obvious need for protection of the gages (and the electrical current passing through them) from the water held within the drop tank. Initial efforts used a thick rubber sealant that was painted over the gage locations and allowed to cure. This method provided sound protection in the drops conducted, but the protective coating was so thick that it affected the impact strains observed in the cylinder. Subsequently gages were protected with layers of Teflon tape and a thin nitrile rubber coating applied around the edges and lead wires. This method proved adequate in most cases while not noticeably altering the measured

signal, but it should be noted that problems with signal quality have not been completely resolved. One problem encountered is the apparent presence of small openings in the coverings of the lead wires that came pre-attached to the strain rosettes. This has led to several instances of signal loss due to simple handling of the lead wires following an experimental drop. In short, once the cylinder and lead wires are wetted following a test drop, the issue of signal quality is a significant concern.

4.3.3 Multi-Channel Dynamic Strain Measurement

It is not an insignificant task to apply the Wheatstone bridge configuration described previously to a practical experimental setup with multiple strain rosettes providing dynamic structural response measurement. This section discusses some of the details of the design of the experimental data acquisition system.

The multi-channel circuitry needed to measure the various voltage differentials is provided by a commercially available peripheral component interconnect (PCI) card produced by the National Instruments Corporation. The card can be inserted directly into the standard PCI slot of compatible desktop computers. In this case a Dell Xeon with a 2.4 GHz processor is used. The maximum sampling rate of the PCI card is listed as 250 kHz, though this rating is for only one channel and assumes sufficient processor speed. For practical applications, the true sampling rate is equal to 250 kHz divided by the number of channels being recorded. Consideration must also be given to data management issues, and whether sampling above a certain rate will produce more data than can be effectively stored and analyzed.

The PCI card is physically connected to the rest of the data-acquisition circuitry via a 68-pin connector cable that runs to a shielded connector block containing screw terminals. Each connector block contains screw terminals for 16 channels, and each is numbered according to

factory specifications. Terminals are also available for electrical grounding, and several switches can be set depending on the type of input signal to be measured.

In addition to the Wheatstone bridge configuration described previously, several electronic components are needed within the circuitry design in order to produce a steady, measurable signal. The first component is a dual-output power supply to provide both the input voltage V_S described previously, but also to provide requisite input voltages for the components to be discussed next. For this work, the two voltage terminals were set to +15 V and -15 V.

The first of these components is a voltage reference device used to ensure that the source voltage V_S for the Wheatstone bridge is constant at a pre-set value and free of surges or dips. Such disruptions in the supply voltage will create erroneous results for strain (see Eq. 4.2) by effectively altering the observed gage resistance R_g . The voltage reference components used for this experimental work are known by the code LM4040 and can be purchased through many commercial sources. In this case, the LM4040s typically reference the input voltage to +5 V or +10 V.

The next circuitry component is the widely-used operational amplifier, or op-amp, needed to further condition the input signal. The op-amps used in this work are known by the code LF412 and are widely available through commercial vendors. These op-amps are dual-channel so that one component can be used to condition two separate signals prior to passage to the Wheatstone bridges.

The final circuitry component is called an instrumentation amplifier and is used to magnify the voltage differential V_I across the two arms of the Wheatstone bridge. With the typical source voltage used in this work being +5 V, this differential voltage resulting from deformation of the strain gages is only on the order of millivolts. To ensure that the signal is

properly measured and not lost in electronic noise, the instrumentation amplifier applies a gain G_n to the V_I signal, such that:

$$G_n = \frac{49,400}{R_{amp}} + 1 \quad (4.9)$$

With R_{amp} being the resistance of a standard ceramic resistor connected to the instrumentation amplifier. The magnitude of the true voltage differential V_I is multiplied by the gain G_n before the output signal is sent to the connector block to be measured and recorded by the PCI card.

All of the various components just described were connected in a manner shown by the schematic in Fig. 4.7.

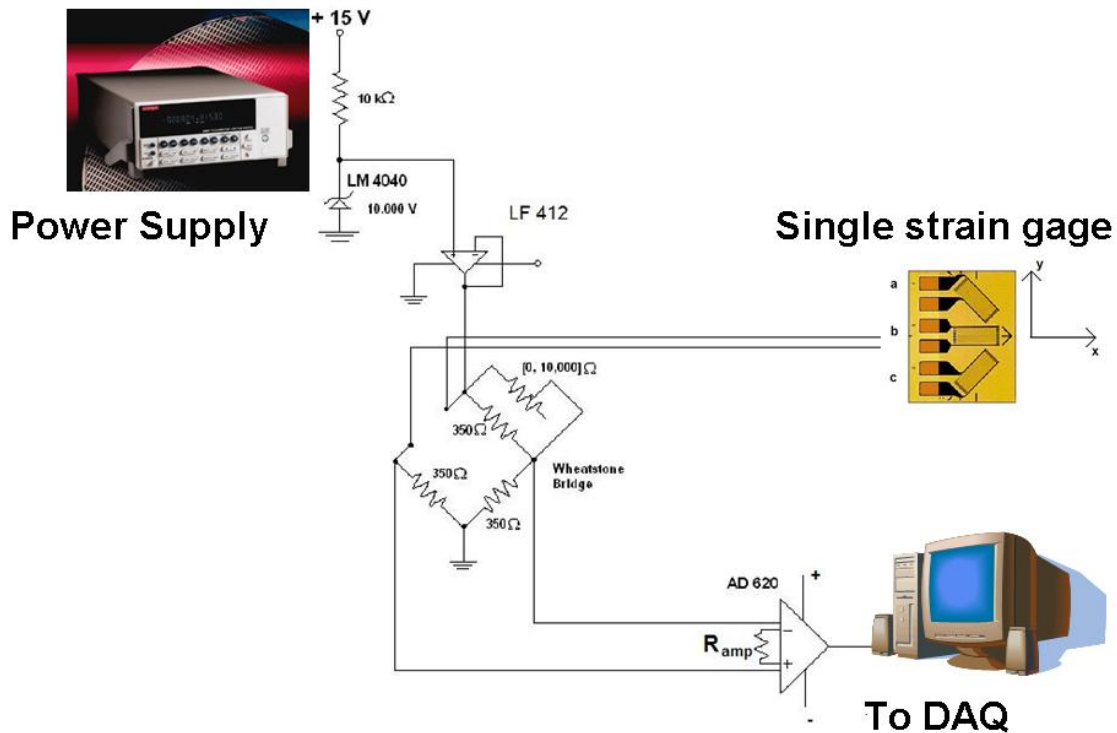


Fig. 4.7 –Schematic of circuitry design for strain measurement

In this study, pre-wired 350-Ohm strain rosettes manufactured by Vishay Intertechnology, Inc. are used. Note that for each strain rosette with three separate strain gages, three of the circuitry layouts shown in Fig. 4.7 must be constructed. These circuits are assembled using a wire-wrap technique in which the various components just described are plugged into sockets. The legs of these sockets are in turn placed through a perforated backing board, and connections are made underneath the board by wrapping small-gage electrical wiring around the appropriate socket leg. Additional screw terminal blocks are added to provide connections for the lead wires of the strain gages, and sockets are grouped so that circuitry relating to individual rosettes was located within the same part of the perforated board. When possible, circuitry components such as the LM4040 and dual-channel LF412 are shared between multiple channels. Care has to be taken to ensure components are not overloaded with parallel channels, resulting in electrical current that exceeds design specifications. Fig. 4.8 shows a picture of one of the wire-wrap circuitry assemblies used in this experimental study with accommodations for up to 16 channels.

4.3.4 Measurement Software and Signal Processing

In this work, the interface software package needed to interpret the analog signals being sent to the PCI card is provided by National Instruments. The software is needed to properly interpret the incoming signals, to provide a user interface for test setup and management, and for processing and recording the signals for later study.

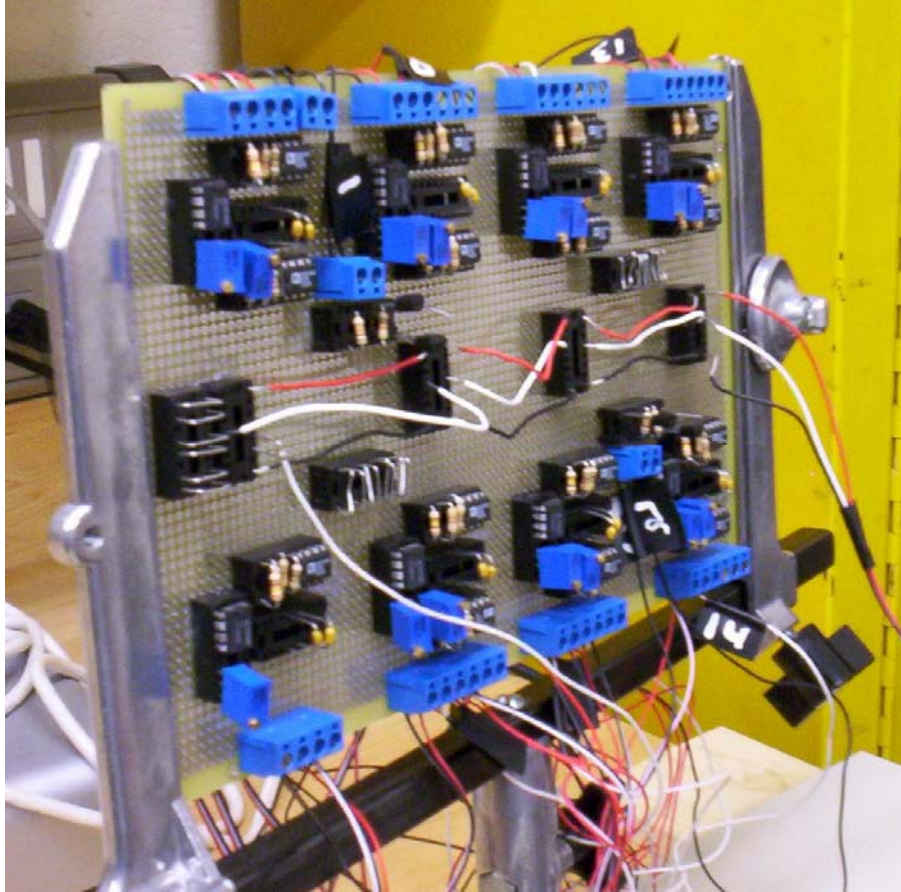


Fig. 4.8 – Wire-wrapped circuitry components for multi-channel strain measurement

This section will describe how the raw measured voltage differential recorded by each PCI channel is used to formulate values for von Mises stress in the cylinder wall at the rosette locations.

Fig. 4.9 shows an example of the raw V_I voltages recorded by the three channels of a strain rosette location on the leading edge of the cylinder 6" from the top end (Station 6_CL_90, see Fig. 4.6).

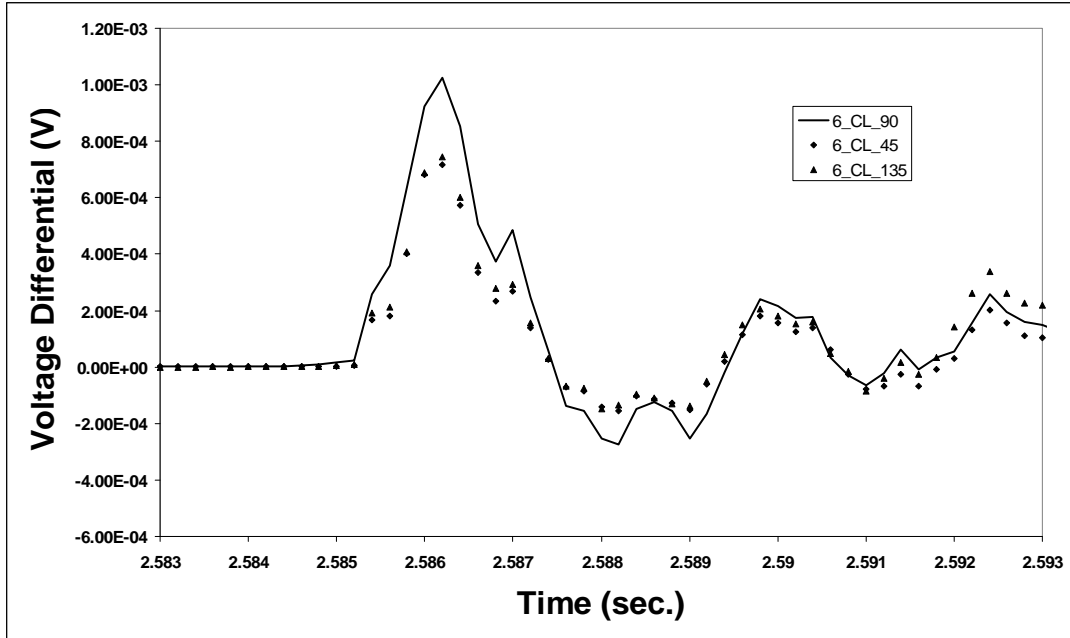


Fig. 4.9 – Raw V_I voltage differentials recorded at Station 6_CL

For comparison, Fig. 4.10 shows the same measured quantities recorded simultaneously for a strain rosette on the leading edge of the cylinder 15" from the top end.

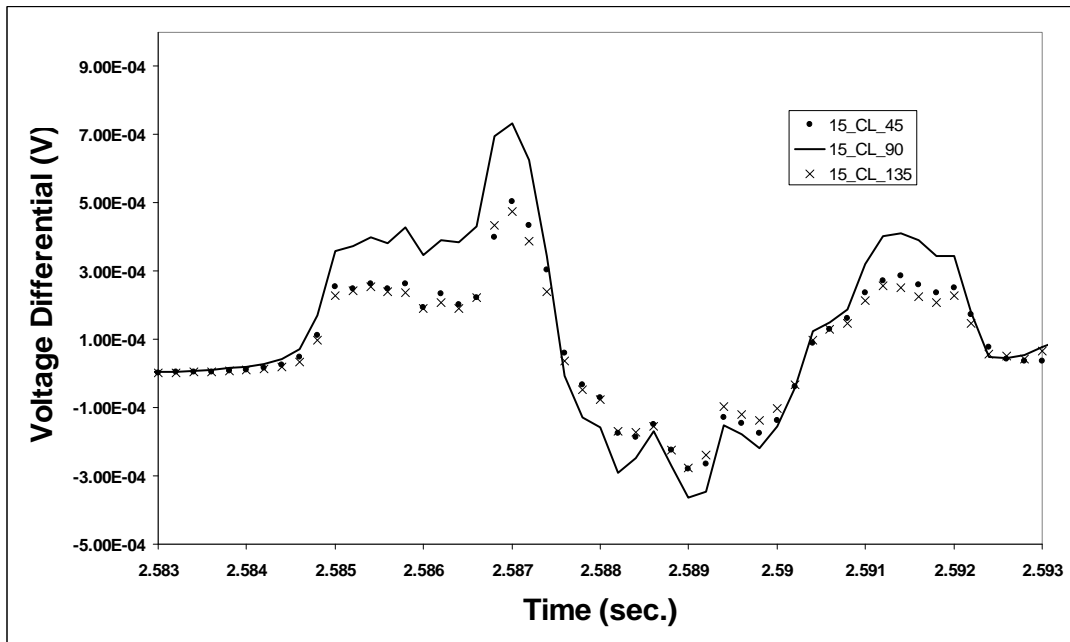


Fig. 4.10 – Raw V_I voltage differentials recorded at Station 15_CL

As can be seen, in both instances the measured differentials are on the order of millivolts, showing the importance of the gain factor G_n applied by the instrumental amplifier. As will be shown, the raw voltage measurements alone are sufficient for identifying general loading trends in the cylinder wall resulting from water impact. Also, the fact that the gages oriented at +45 and +135 are correlated provides a convenient means for quickly checking signal integrity during data processing.

The National Instruments DAQ software allows the three signals shown in the above figures to be processed according to Eqs. 4.1-4.8. Notice that the source voltage V_S through each Wheatstone bridge must also be monitored in order for the signal to be converted. To minimize the number of channels devoted to V_S , circuitry for gages on a single rosette were usually connected in parallel. Care has to be taken to ensure the electrical current does not exceed the limits of the shared LM4040.

The software also allows for filtering of the measured signal in real-time. A band filter is applied to 60 Hz +/- 1 Hz to account for common electrical noise, and a low pass filter is applied at 2,500 Hz since spectral analysis shows the dominant frequencies of structural vibration to be found well below 1,200 Hz.

Processing of the data in real-time affects the speed at which data can be effectively recorded. To ensure the sampling rate of the PCI card is fully utilized, data is typically recorded in raw, voltage differential form (as shown above in Figs. 4.9 and 4.10), and saved to a data file. This file is subsequently reopened and input to an additional processing program for conversion to von Mises stress history files.

Figs. 4.11 and 4.12 show the resulting von Mises stress history plots for the same locations for which the raw voltages are shown in Figs. 4.9 and 4.10.

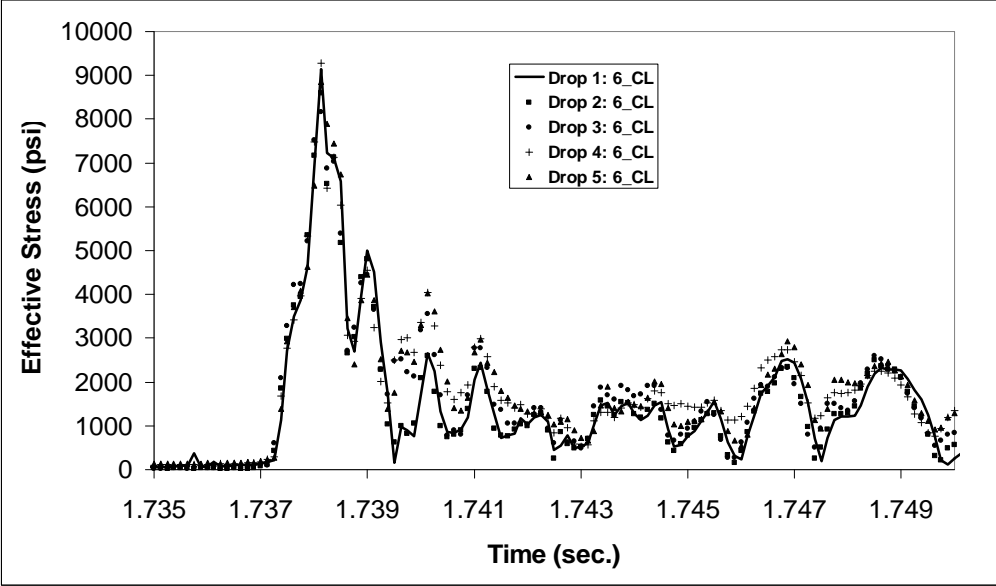


Fig. 4.11 – Measured time histories of von Mises stress at Station 6_CL

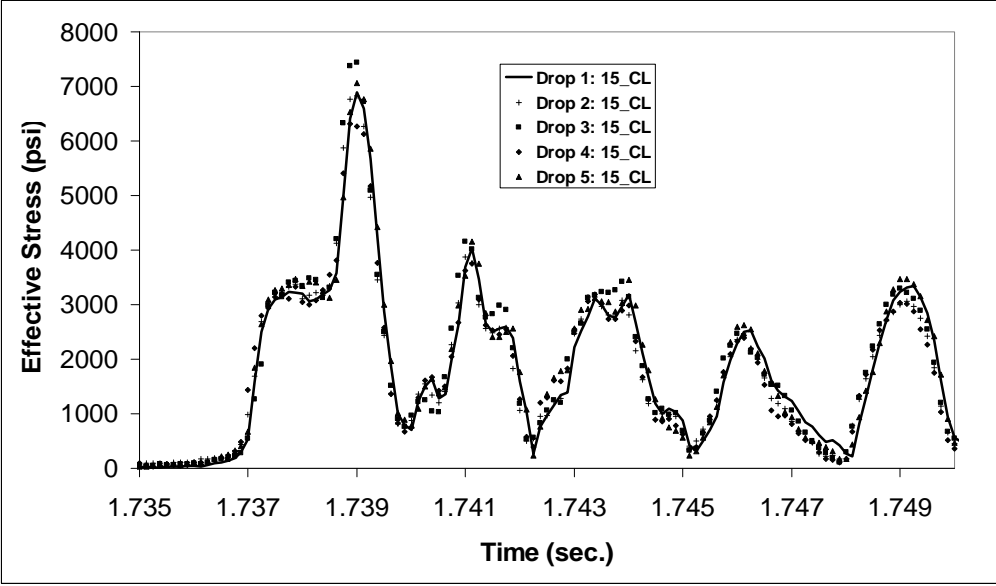


Fig. 4.12 – Measured time histories of von Mises stress at Station 15_CL

In spite of several sources of error to be discussed further in later sections, the measured results from the cylinder impact tests show consistent agreeability, at least based upon qualitative

comparisons of the stress history plots. Though there are differences observed in the peak values of the stress readings, there is consistent temporal agreement in the plots. That is to say, the peaks and valleys of the stress history plots match up consistently well, even when several separate drops are compared.

4.3.5 Experimental Uncertainty

The experimental setup described in the previous sections is used to measure the structural response of a thin-walled aluminum cylinder to a blunt impact with a free water surface. Experimental variability is present in all real-world testing scenarios, and cannot be completely removed from even the most advanced experimental setups. In the cylinder-splash tests, experimental variability between drops is primarily present in two physical quantities: the height of the axis of rotation above the still water level, and the radial velocity of the cylinder at impact with the free surface.

The aluminum rod used as the supporting axle for the hinged cylinder is supported by two aluminum brackets clamped to either side of the acrylic tank. At the start of each round of tests, the axle is positioned 1.5" above the free water surface to ensure that the cylinder breaks the surface in a perfectly horizontal manner. This is thought to maximize the slamming forces at impact and ensure a response that can be recorded with sufficient fidelity. However, in some instances the brackets supporting the hinged cylinder are seen to shift slightly during tests and have to be repositioned. In all likelihood this repositioning along with any movement of the brackets that goes unobserved introduces some degree of experimental error into the measured response of the cylinder as it breaks the free water surface. Since even a slight change in the height of the axis of rotation above the free surface can cause the cylinder to strike the water

surface unevenly, these slight variations are thought to have a potentially significant effect on the stress response within the cylinder.

The rotational velocity of the cylinder as it impacts the free surface is the second experimental parameter that has potential for variation from one drop to the next. The cylinder is mounted onto a small platform using a ¼" threaded bolt that goes through the center of the bottom end cap. The platform is in turn mounted to two rectangular connecting legs containing holes for the support axis mentioned above. Though lubrication is occasionally applied to reduce any friction generated between the rod and the connector legs, some resistance is undoubtedly produced. Perhaps more significant to the impact velocity are the lead wires connecting the strain rosettes to the DAS connector block. Efforts are made during testing to keep the wires draped across the top of the acrylic tank and out of the way of the falling cylinder path. However, in some instances the wires drag across the upper edge of the tank or fall into the water ahead of the cylinder.

This discussion of the uncertainty in the impact velocity and cylinder orientation as it breaks the free surface is relevant because these are the parameters considered in the model validation exercise presented in §4.4. These are by no means the only uncertain parameters present in the experimental cylinder assembly. In addition to some of the structural characteristics of the cylinder (i.e., tuning parameters to be discussed in §4.3.3), there is also measurement uncertainty introduced by the DAS. Electrical interference and noise cannot be eliminated completely, and so the recorded signal contains some degree of measurement error.

4.3.6 Tuning Parameters

It is worth noting that the two random parameters just discussed are not the only experimental parameters for which uncertainty exists. Several structural parameters of the aluminum cylinder, namely elastic modulus E , density ρ , and wall thickness t vary spatially throughout the cylinder, but do not change from one drop to the next (assuming plastic yielding does not occur). An attempt has been made at laboratory testing of the aluminum sheeting used to construct the aluminum cylinders in order to determine the stiffness parameter E . Though the tests are performed on samples cut from the same sheet of aluminum used to construct the test cylinder, the samples do not necessarily reflect any changes in elastic modulus due to the cold-working performed on the sheet to form the cylindrical shape. Regardless, the tensile testing machine has trouble gripping the thin samples adequately during the pull sequence, and conclusive results have not been obtained. Fig. 4.13 shows one of the samples tested to failure. Absent any meaningful test data concerning the elastic modulus E , the nominal value stated by the manufacturer, 10.5 ksi is assumed to be the mean for modeling purposes.

The effective stiffness of the cylinder is further complicated by the presence of the epoxied seam running along the back edge opposite the leading edge which first impacts the free water surface. This seam changes the global stiffness of the aluminum cylinder, though quantifying these effects is a challenging undertaking. Furthermore, it is not known what effect, if any, this seam has on the impact-induced wall stresses within the cylinder resulting from impact. All of these unknown parameters can be addressed through model tuning and calibration.

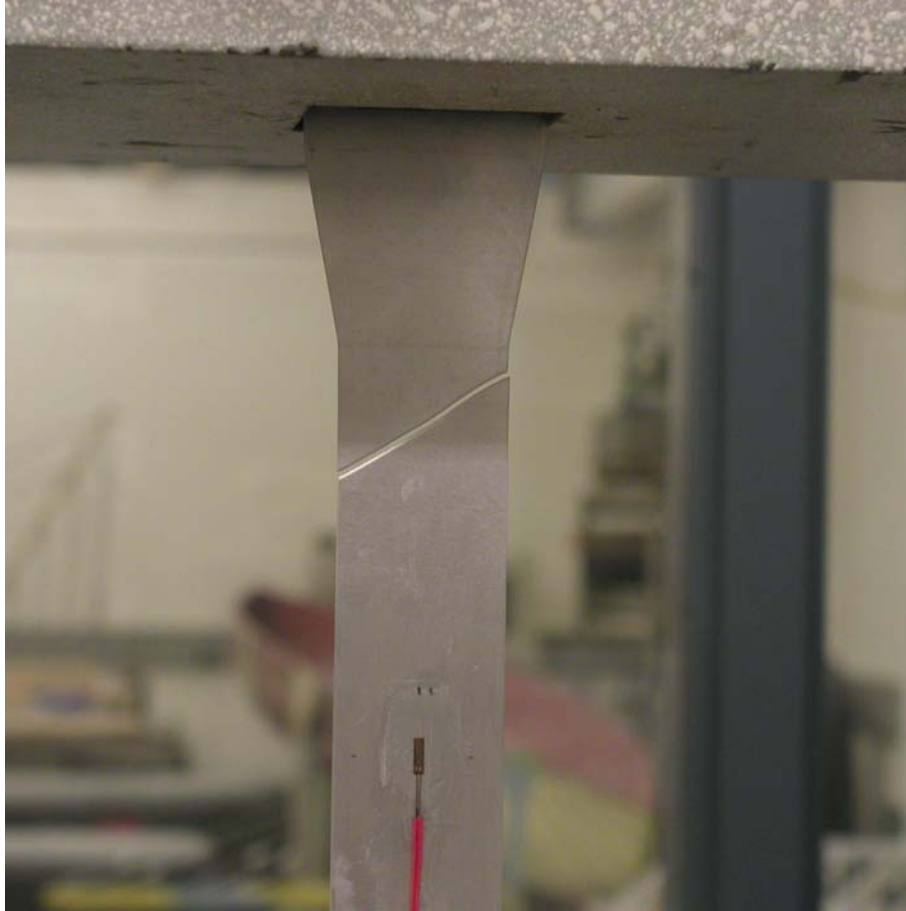


Fig. 4.13 – Al 3003 sample loaded to failure in elastic modulus test

4.4 Qualitative Cylinder Model Validation

This section presents the procedures and results of a model validation exercise conducted using the experimental setup just described and a corresponding model constructed with LS-Dyna. A simple qualitative validation is first presented, in which model predictions and test data are visually compared. Quantitative validation results are next shown, in which both classical and Bayesian statistical metrics are used to evaluate the accuracy of the model prediction based on the measured data.

The cylinder model to be validated is of the same form as that described in the verification exercise detailed in Chapter 3. However, recall that one of the significant

observations from the verification exercise is the sensitivity of the iterative coupling algorithm employed by LS-Dyna to the relative mesh resolutions of the fluid and structural regions. It can be seen in Figs. 3.7 and 3.8 that if the Eulerian fluid mesh is more finely resolved than the Lagrangian structural mesh, then erroneous stress results will be introduced into the structural elements as the coupling algorithm tries to reconcile the boundary between the two domains. Therefore, for the validation phase of this study, the respective mesh sizes are chosen very carefully. It is found that acceptable run times can still be achieved using rectangular Eulerian solid elements with edge lengths of 0.15" and Lagrangian structural shell elements measuring 0.1316" × 0.1309". The resulting stress history plots confirm that a significant structural response is not recorded in the cylinder wall until after the impact with the free water surface.

It is not uncommon in engineering analyses based upon computational models for predictions to be compared qualitatively to the available data concerning the real-world system. In many instances, the model prediction for a range of input conditions is plotted against test data and a simple visual comparison is made. Indeed, this sort of approach appears to be the dominant procedure currently followed for validation efforts in most science and engineering disciplines using computational models. Two recent examples (among many) of validation using visual comparisons involving structural impact include Hughes et al. (2008) and O'Daniel et al. (2005). Though the work presented here includes more rigorous quantitative validation metrics as well, there is valuable insight to be gained from qualitative model validation. Particularly in the early stages of model development, qualitative validation provides a straightforward and inexpensive way for engineers to quickly gage the accuracy of predictions.

The LS-Dyna post-processing software includes animation capabilities for viewing of the modeled system under simulated loadings. Figs. 4.14a-c show three frame captures from the LS-Dyna model of the cylinder impact using nominal input values.

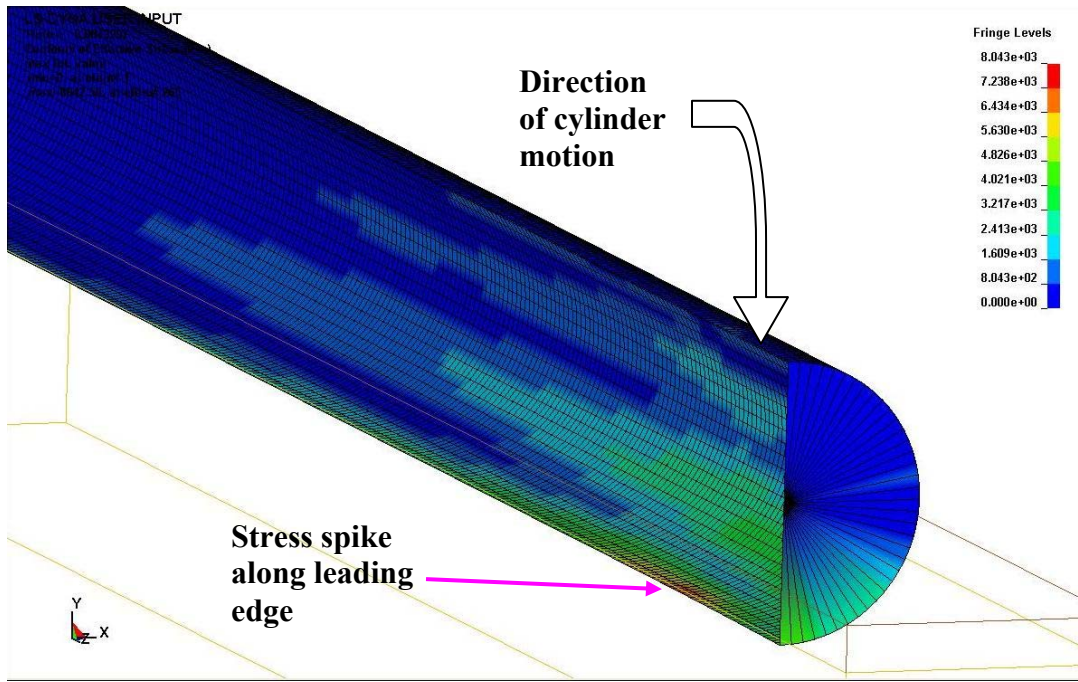


Fig. 4.14a – Initial stress concentration on cylinder wall at initial water impact

For clarity, the fluid region is not shown, however the original free surface is indicated and shown to be parallel to the impacting cylinder. A stress concentration is just visible near the forward end of the impacting cylinder, in the vicinity of measured locations Sta3_CL and Sta6_CL. The legend on the right indicates that stress levels at this location reach over 8.0 ksi. The entire leading edge of the cylinder experiences higher stress levels during the initial impact with the free water surface. Additional stress waves are visible up the sides of the cylinder, though their magnitudes are not as high as the concentration along the leading edge. Fig. 4.14b shows conditions 1.2 milliseconds later.

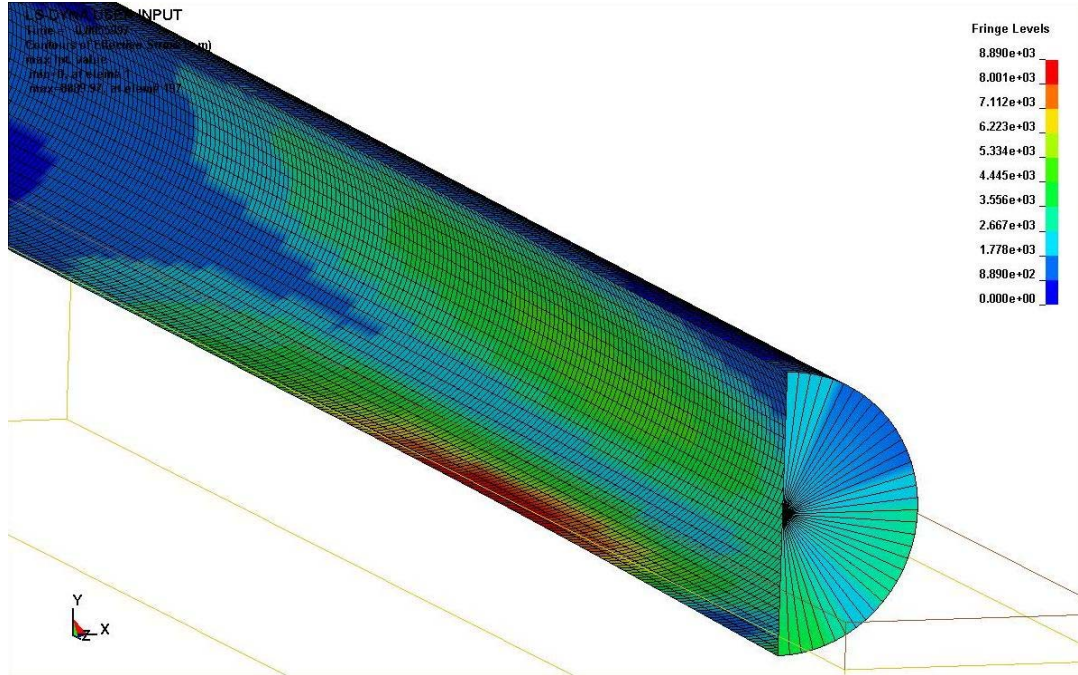


Fig. 4.14b – Stress wave moving along leading edge as cylinder penetrates free surface

One can now see the presence of a pronounced stress wave moving along the leading edge of the cylinder as it breaks the free surface. The peak stress in the cylinder wall has now reached nearly 8.9 ksi in the vicinity of Sta9_CL and Sta12_CL. A large secondary stress wave is also seen to be moving up the side of the cylinder. The final frame capture in Fig. 4.14c shows conditions after an additional 1.7 milliseconds.

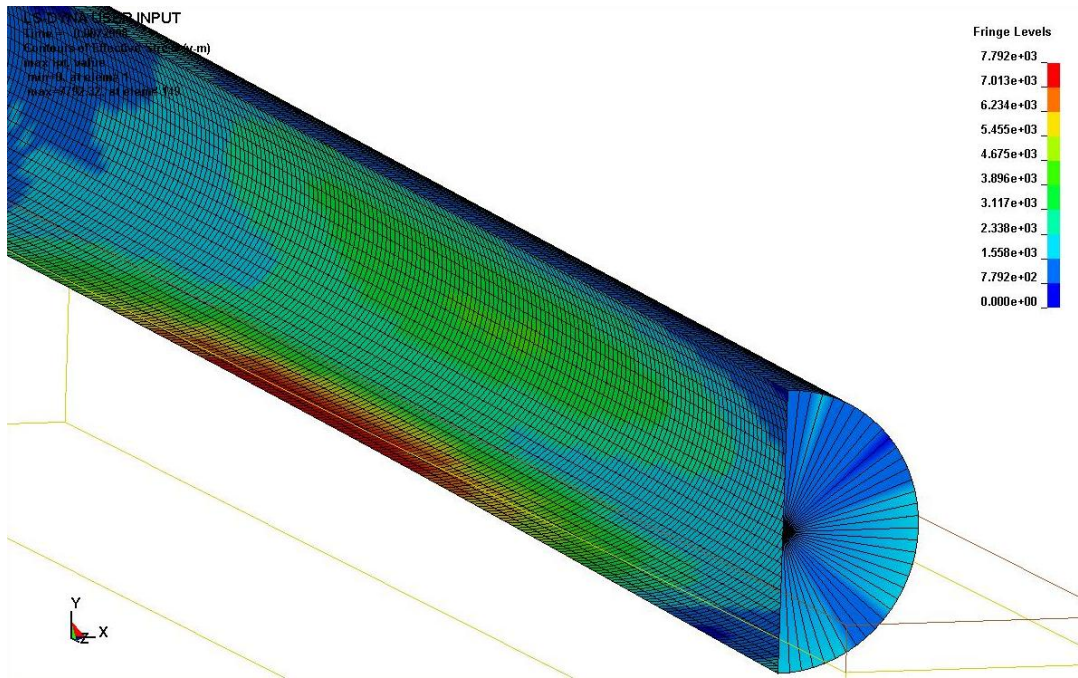


Fig. 4.14c - Stress wave moving along leading edge as cylinder penetrates free surface

The peak stress along the cylinder leading edge is now roughly 7.8 ksi, with the concentration now at the cylinder midpoint near Sta15_CL. Figs. 4.14a-c show how during the cylinder-water impact, the stress concentration in the cylinder wall starts near the top end cap, which makes intuitive sense due to the higher relative velocity (farther from rotational axis) in this region. The rigid end cap lends structural stiffness and the stress wave increases in magnitude for some distance down before subsiding as it approaches the cylinder midpoint. Secondary stress waves are seen to move up the cylinder wall from the leading edge and also follow the main stress concentration down towards the midpoint.

Though there is no available counterpart to the LS-Dyna animation frames for visualizing the experimental results, the same stress propagation patterns seen in Figs. 4.14a-c can be deduced based upon the stress time histories measured with the experimental rig and cylinder.

Fig. 4.15 shows one such plot for four locations along the leading edge of the 3" diameter aluminum cylinder during water impact.

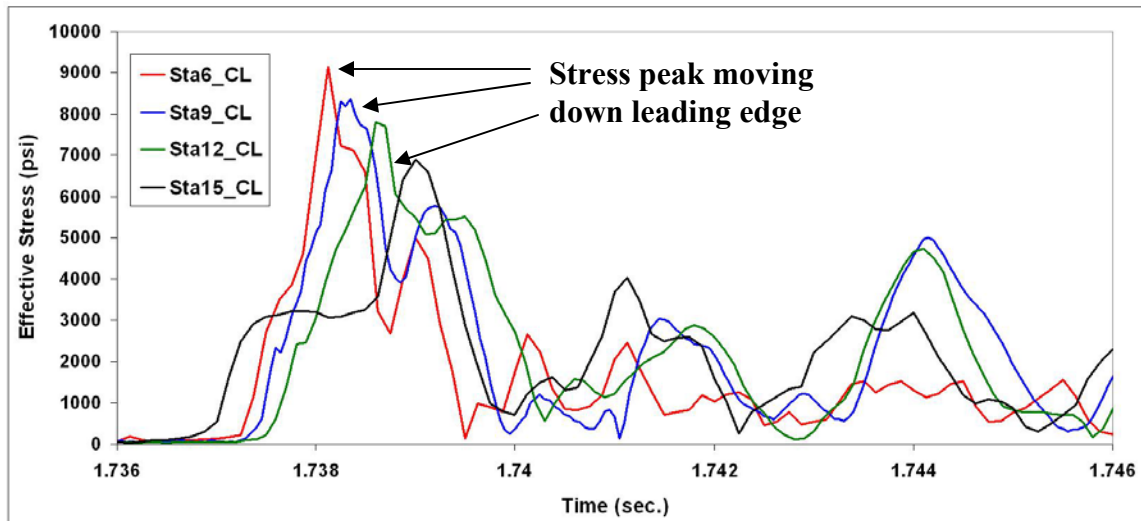


Fig. 4.15 – Stress time histories measured with experimental cylinder

These curves offer qualitative reinforcement to previously observed stress patterns. The location closest to the upper end of the cylinder, Sta6_CL, undergoes peak stress before the other measured locations, and the stress spike dissipates as it moves away from the rigid end cap. Also, the magnitudes of peak stresses are in rough agreement with those predicted by the LS-Dyna model. At the cylinder midpoint, Sta15_CL, the initial shock of cylinder impact actually is registered before the other locations, but the peak stress does not increase until the stress wave has moved down the cylinder leading edge. Similar trends can be seen from monitoring the stress history plots at locations moving up the cylinder wall, though the movement of stress waves is not as pronounced. It should be noted that the curves plotted in Fig. 4.15 were recorded on different cylinder drop tests: Sta6_CL and Sta15_CL were measured from the same test, while Sta9_CL and Sta12_CL were each measured during separate tests. To ensure that the

signals are appropriately aligned temporally, one of the channels in the data acquisition unit was designated as a synchronization channel. Typically the raw voltage through the *b* gage of Sta3_CL was recorded because of the clearly defined pulse that formed just after impact and then quickly dissipated. With this synchronization signal always recorded, measurements from drop tests conducted at different times as well as from different gage locations can be aligned by matching the location in time of the peak of this signal.

To conclude the qualitative validation discussion, visual comparisons of the LS-Dyna model prediction to the measured effective stress in the cylinder leading edge are presented in Figs. 4.16a-d.

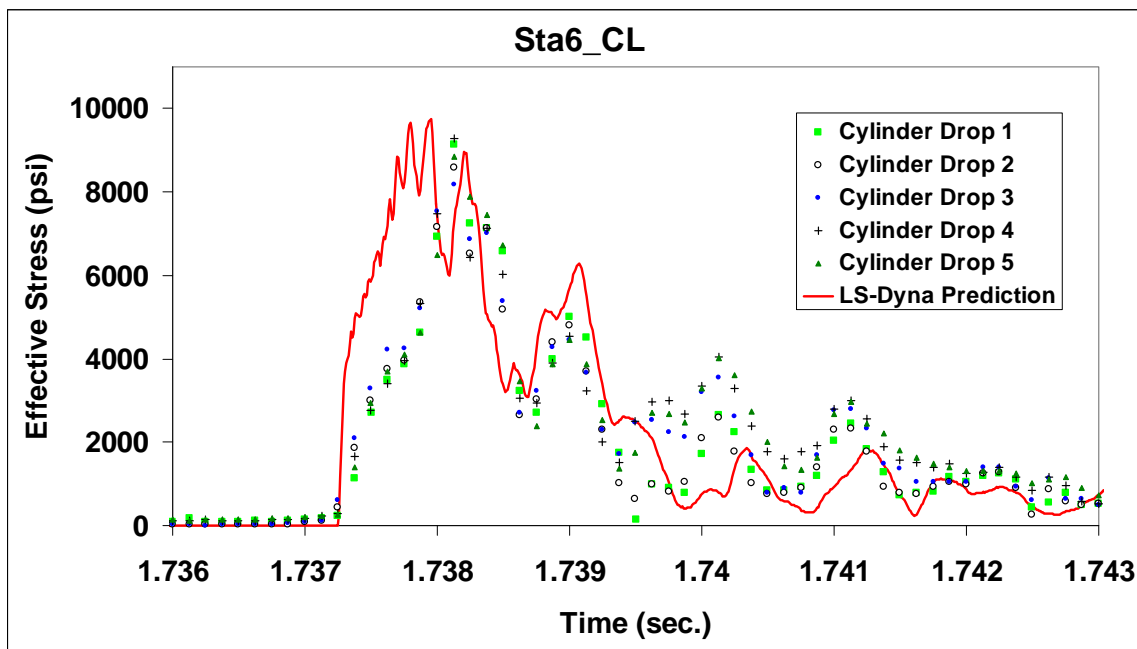


Fig. 4.16a – LS-Dyna prediction and measured water impact data for Sta6_CL

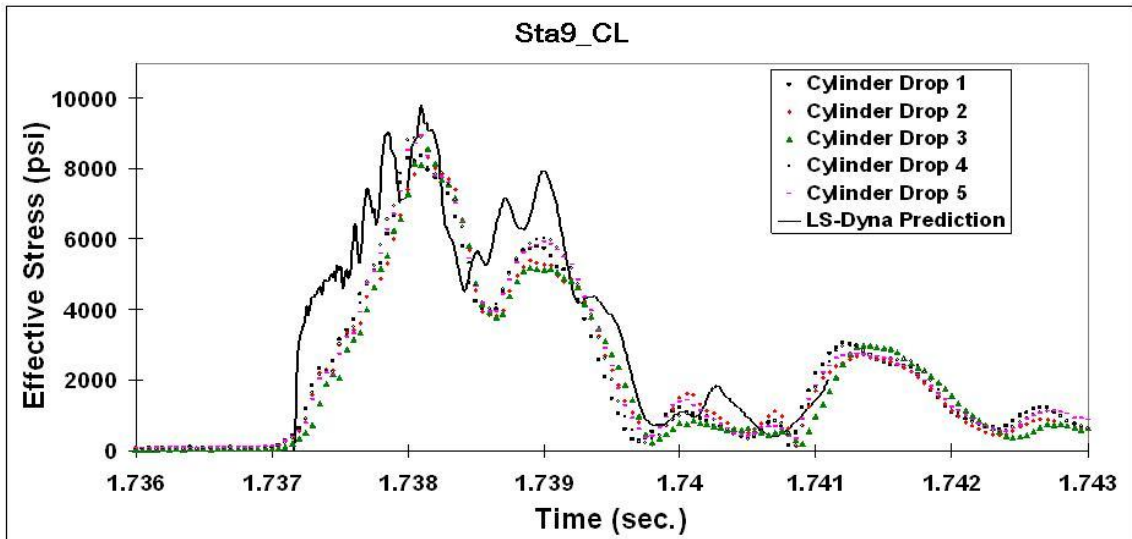


Fig. 4.16b – LS-Dyna prediction and measured water impact data for Sta9_CL

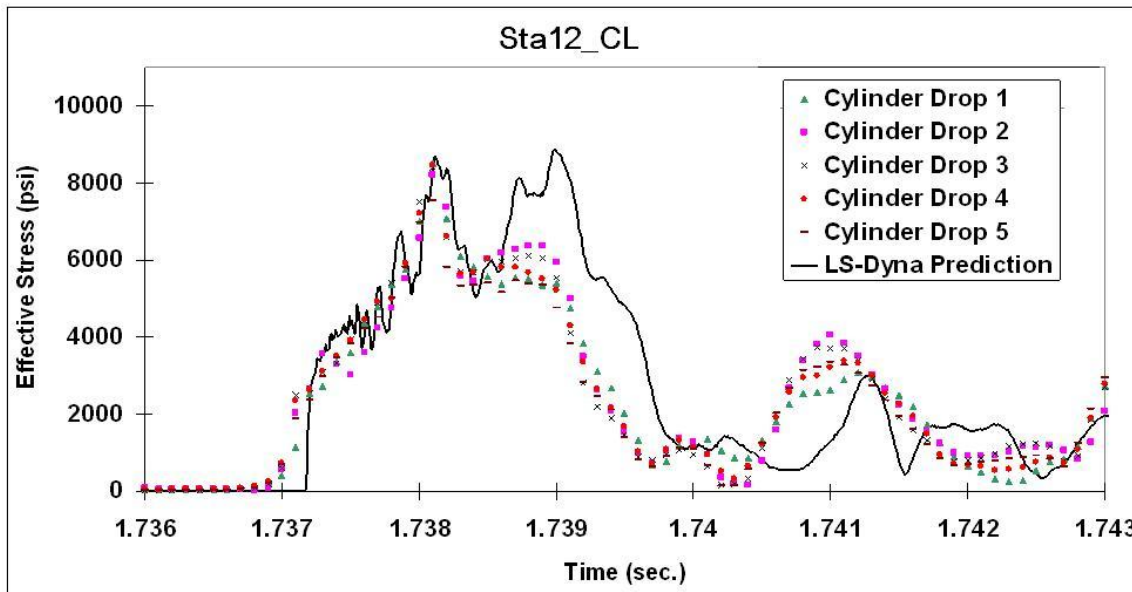


Fig. 4.16c – LS-Dyna prediction and measured water impact data for Sta12_CL

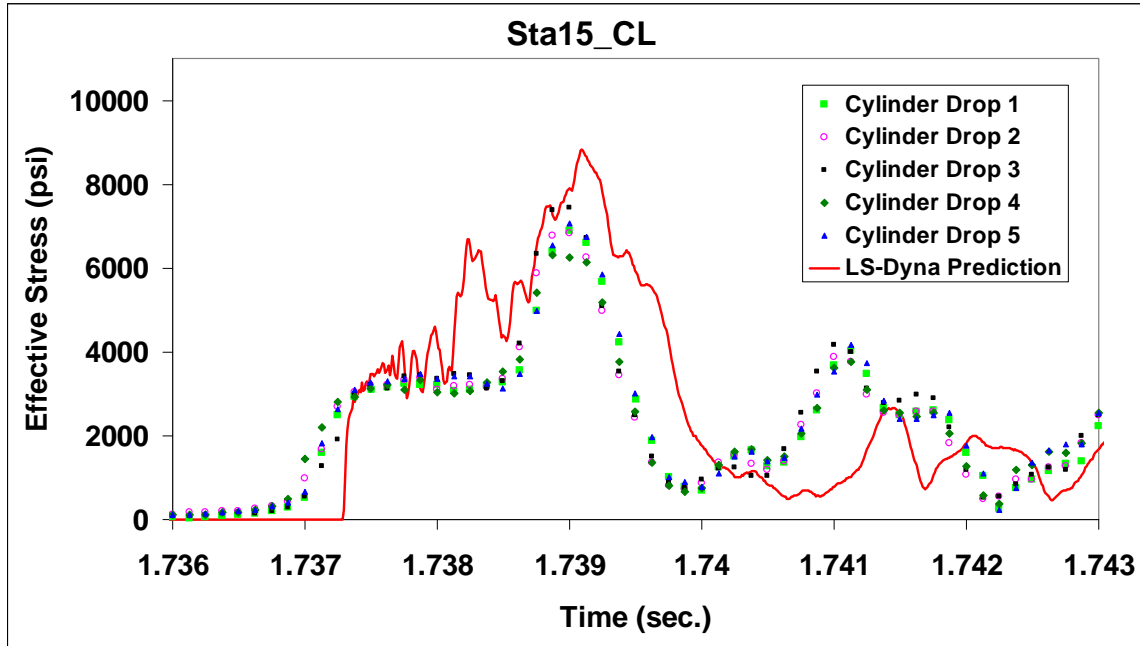


Fig. 4.16d – LS-Dyna prediction and measured water impact data for Sta15_CL

The LS-Dyna model is seen to generally capture the stress propagation along the leading edge of the cylinder during water impact. The extent of agreement with measured peak stress levels varies by location. The model appears to under predict the post-impact stress oscillations following the initial stress spike, indicating that global damping factors in the model may need to be reduced.

4.5 Quantitative Validation Under Uncertainty

In the preceding discussion of qualitative model validation, the LS-Dyna prediction and test data are treated as deterministic. However, the presence of experimental uncertainty has already been discussed in this chapter, and Figs. 4.16a-d have been presented showing the variability that is present between multiple cylinder drop tests. With this in mind, the measured stresses in the cylinder resulting from water impact can be thought of as random samples from an underlying

statistical distribution. In order to accurately reflect this, the LS-Dyna prediction should also account for uncertainty and show a suitable distribution for the model output. In this case, validation becomes a matter of comparing two statistical populations.

For the purposes of the validation exercise presented here, only the radial impact velocity V_{imp} and height of the axis of rotation above the free water surface h are considered as random inputs to the LS-Dyna model, because these are thought to be the only significant experimental conditions that vary from one drop to the next. The experiments were all conducted using the same 3" rolled aluminum cylinder outfitted with strain rosettes. The impact parameters V_{imp} and h are both assumed to follow normal probability distributions, with $V_{imp} \sim N(4.36 \text{ rad/sec}, 0.12 \text{ rad/sec})$ and $h \sim N(1.5", 0.025")$. A battery of LS-Dyna model runs is used to see how the predicted cylinder response changes as a function of V_{imp} and h . This allows for creation of response surfaces to describe output quantities at different locations within the cylinder. These response surfaces can then be used in a straightforward Monte Carlo simulation approach to generate the statistical distributions of the output quantities of interest.

Several validation examples will now be given using both classical statistical comparison metrics and also Bayesian validation metrics. Comparisons will be shown using the measured peak stress data and model prediction quantities at several locations on the cylinder. Hypothesis testing will be used to compute the validation metrics. In each instance, a null hypothesis H_0 is considered in which the difference between the model prediction and test data is zero. Additionally, an alternate hypothesis H_A is formulated wherein the model prediction deviates from the data by a significant amount.

4.5.1 Classical Hypothesis Testing

Table 4.2 shows the experimental peak von Mises stress results from 10 cylinder drop tests at four gage locations recorded simultaneously. The tests were conducted during one laboratory session, in which the cylinder was allowed to fall over from an initial vertical alignment. Between drops the cylinder was removed from the water and the motions in the free water surface allowed to dissipate.

Table 4.2 – Peak von Mises stress (psi) results from 10 cylinder drop tests

Drop #	Sta6_CL	Sta6_+45	Sta15_CL	Sta15_+90
1	9,143.75	4,185.22	6,886.70	2,616.96
2	8,589.59	3,994.23	6,831.51	2,574.40
3	8,162.97	4,103.36	7,431.11	2,770.20
4	9,021.05	4,144.51	6,899.67	2,572.35
5	9,271.23	4,205.06	6,305.63	2,572.53
6	8,856.11	4,653.73	7,067.51	2,774.27
7	9,269.82	5,358.79	5,724.00	2,504.67
8	7,587.69	4,028.79	7,442.95	2,949.45
9	8,393.38	4,286.41	6,756.16	2,490.93
10	8,378.91	4,551.08	6,676.73	2,762.99

The ten measurements can be considered random samples from a statistical population, owing to the experimental uncertainty and measurement errors previously discussed. Table 4.3 summarizes the sample average \bar{y} and standard deviation σ_y at each location, as well as the LS-

Dyna model prediction x_0 at the nominal values for V_{imp} and h , 4.36 rad/sec. (see Table 4.1) and 1.5", respectively.

Table 4.3 – Sample statistics and LS-Dyna peak stress prediction for multiple locations

	Sta6_CL	Sta6_+45	Sta15_CL	Sta15_+90
\bar{y}	8,667.45	4,351.12	6,802.20	2,658.88
σ_y	547.69	413.03	507.82	147.88
LS-Dyna: x_0	9,747.24	4,467.14	8,837.33	6,395.51

The sample statistics apply only to the ten measurements shown in Table 4.2; a second round of tests would produce different sample statistics. Therefore, the sample mean \bar{y} is considered to be a random variable that can be shown to follow the Student t -distribution. Under the null hypothesis H_0 , the following should then hold true:

$$\left| \frac{x_0 - \bar{y}}{\sigma_y} \right| \sqrt{n} < t_{\alpha, n-1} \quad (4.10)$$

where $t_{\alpha, n-1}$ is the t -distribution evaluated at significance level α for $n-1$ degrees of freedom. However, for the set of results presented above, only the prediction for Sta6_+45 satisfies the condition given in Eq. 4.10 at a significance level α of 0.05. An alternate way of conveying these results is to compare the model prediction to the confidence bounds on the sample mean \bar{y} based on the observed data. These bounds can be found via:

$$\langle \mu \rangle_{1-\alpha} = \left[\bar{y} - t_{\alpha/2, n-1} \frac{\sigma_y}{\sqrt{n}}; \bar{y} + t_{\alpha/2, n-1} \frac{\sigma_y}{\sqrt{n}} \right] \quad (4.11)$$

Table 4.4 shows the upper and lower 95% (i.e., $1-\alpha$) confidence bounds for the mean peak stress at each of the four measured locations based on the observed data.

Table 4.4 – 95% Confidence bounds for mean peak stress based on experimental results

Location	Sta6_CL	Sta6_+45	Sta15_CL	Sta15_+90
Upper Bound	9,059.22	4,646.56	7,165.44	2,764.65
Lower Bound	8,275.68	4,055.68	6,438.95	2,553.1

By comparing the LS-Dyna predictions in Table 4.3 to these values, one can see that the only location for which the LS-Dyna prediction x_0 falls within the lower and upper confidence bounds is Sta6_+45. Therefore the null hypothesis is accepted only at this location. These results indicate that further tuning and calibration of the model parameters in the LS-Dyna cylinder model are needed.

A more realistic predictive model of the cylinder impact test will include the effects of randomness in the experimental input parameters (for example V_{imp} and h mentioned previously). Therefore, rather than having a single value to compare to the measured data at each location, the model produces a distribution for the peak stress at each location. Now, in addition to comparing the mean values of each distribution using the t -distribution as shown above, an additional statistic can be defined to compare the variance of both the model prediction and the observed data. This can be done using the χ^2 statistic where:

$$\chi^2 = \frac{(n-1)s_Y^2}{\sigma^2} \quad (4.12)$$

Just as the sample mean can be shown to follow the t -distribution, the sample variance s_Y^2 can be shown to follow the χ^2 distribution. Under the null hypothesis H_0 , the variance on the model prediction will equal the true variance of the cylinder impact tests. Note that s_Y^2 is based only upon the measured samples, and therefore only estimates the actual variance.

Four different locations on the cylinder are now used to demonstrate classical validation considering the mean and variance of both the measured data sample and the model prediction. Using this formulation, a 10,000-sample Monte Carlo simulation is conducted using LS-Dyna model results and assuming joint, independent normality for V_{imp} and h . The distribution parameters are $\mu = 4.36$ rad/sec, and $\sigma = .12$ rad/sec for V_{imp} ; and $\mu = 1.5''$ and $\sigma = .025''$ for h . A linearly-iterpolative, non-parametric response function is used based on the battery of LS-Dyna runs conducted. Drop test results from 5 independent trials are used for validation, and are shown in Table 4.5.

Table 4.5 – Peak von Mises stress measurements for five drop tests at four new locations

Drop #	Sta9_CL	Sta9_+45	Sta12_CL	Sta12_+90
1	8,379.65	3,818.77	7,805.52	4,442.36
2	8,567.88	3,927.78	8,510.63	4,681.35
3	8,903.35	4,059.52	8,210.19	5,031.63
4	9,166.04	4,022.81	8,400.20	5,006.65
5	8,892.66	4,031.73	8,453.00	4,826.07

The sample mean and variance as well as the LS-Dyna model prediction mean and variance are summarized in Table 4.6.

Table 4.6 – Observed sample and model prediction statistical parameters

Location Parameter	Sta9_CL	Sta9_+45	Sta12_CL	Sta12_+90
Sample mean: \bar{y}	8,781.91	3,972.12	8,275.91	4,797.61
Sample variance: s_Y^2	95,548.2	9,810.5	81,870.6	59,748.6
Prediction mean: μ_X	9,734.91	4,397.12	8,841.40	6,203.75
Prediction variance: σ^2_X	45,674.2	6,694.3	67,632.9	17,664.5

Using the t -distribution for the mean values and the χ^2 distribution for the variances, the acceptance or rejection of the null hypothesis at the 0.05 significance level is shown for each location in Table 4.7.

Table 4.7 – Model validation via classical tests for mean and variance

Location Test Statistic	Sta9_CL	Sta9_+45	Sta12_CL	Sta12_+90
T	Rejected	Rejected	Rejected	Rejected
χ^2	Accepted	Accepted	Accepted	Rejected

These results show that the classical validation test based on the t -distribution for comparing the model mean prediction to the observations rejects the null hypothesis at each location. However,

by the χ^2 test, the variance on the model prediction is supported by the data at each location except Sta12_+90. The null hypothesis does not pass both tests at any single location.

The classical validation metrics are evaluated independently for each location of interest on the cylinder, despite being produced by the same model evaluations. If an aggregate validation metric for multiple locations is desired, the Mahalanobis distance similarity metric can be considered as the multivariate counterpart to the T statistic. It can be thought of as the distance between the centroids of two data clouds. It is computed via (Anderson 1984):

$$d^2 = n(\bar{\mathbf{Y}} - \boldsymbol{\mu}_0)^T \mathbf{S}^{-1} (\bar{\mathbf{Y}} - \boldsymbol{\mu}_0) \quad (4.13)$$

where $\boldsymbol{\mu}_0$ is the vector of mean values of the predicted system responses from a probabilistic model, $\bar{\mathbf{Y}}$ is the vector of mean values of the experimental measurements, \mathbf{S} is the covariance matrix of the experimental data, and n is the number of random samples from the probabilistic model. The reader is referred to Srivastava (2002) for additional information regarding use of the Mahalanobis distance, including checking for covariance similarity between the model output and the observed data.

4.5.2 Bayesian Hypothesis Testing

Bayes' Theorem is often applied as a tool for probabilistic analysis, and is valued for the way it allows newly obtained information to be used to update the previously held belief concerning the probability of some event. In general form, Bayes' Theorem can be stated (Haldar and Mahadevan 2000):

$$P(E_i|A) = \frac{P(A|E_i)P(E_i)}{\sum_{i=1}^n P(A|E_i)P(E_i)} \quad (4.14)$$

where E_i is the possible event and A is the new information. This idea has been applied to the assessment of model uncertainty, as discussed by Alvin et al. (1998). Under this formulation, the various models under consideration comprise the universal space, and as new data is obtained the relative probabilities of the respective models being correct are updated. In the case of a single model, Bayesian hypothesis testing can be implemented, wherein a model is either accepted as being equivalent to the actual system (null hypothesis, $H_0: x = x_o$) or rejected (alternate hypothesis, $H_A: x \neq x_o$). Several validation metrics based upon Bayesian hypothesis testing have been proposed (Mahadevan and Rebba 2003; Rebba and Mahadevan 2003; Zhang and Mahadevan 2003).

In this section a comparison will be conducted using the experimental data obtained for four different locations along the cylinder leading edge. The metric for comparison is known as the Bayes factor (Jeffreys 1961), and is the ratio of the relative probabilities of observing the experimental data under the null hypothesis H_0 and alternative hypothesis, H_A . Mathematically this is expressed as:

$$B = \frac{P(D | H_0)}{P(D | H_A)} \quad (4.15)$$

When B is found to be greater than 1, the observed data D gives more support to the null hypothesis than to the alternate hypothesis. Bayes' theorem can be used to compute the posterior probability for the null hypothesis, and this in turn can be used to calculate the confidence C in the null hypothesis being true:

$$C = \frac{P(H_0)B}{P(H_0)B + 1 - P(H_0)} \quad (4.16)$$

The prior degree of belief that the null hypothesis is true $P(H_0)$ can be considered to be equal to that for the alternate hypothesis absent any prior knowledge, that is, $P(H_0) = P(H_A) = 0.5$. In this

case, the confidence in H_0 then becomes $C = B/(B+1)$. Chapter 6 will present a methodology for extrapolating the confidence C in a computational model from a validated domain to a domain for which test data is unavailable.

For continuous parameters in the absence of prior knowledge, the Bayes factor can be expressed as the ratio of posterior and prior densities evaluated at the model prediction value (Rebba 2005):

$$B = \frac{f(x | \theta_0)}{\int f(x | \theta) f(\theta) dx} = \frac{f(\theta | x)}{f(\theta)} \Big|_{\theta=\theta_0} \quad (4.17)$$

Therefore, the Bayesian validation metric simply becomes the ratio of the posterior density for the continuous parameter to the prior density, evaluated at the value predicted by the model.

As in the classical validation test, a 10,000-sample Monte Carlo simulation is conducted using LS-Dyna model results and assuming joint, independent normality for V_{imp} and h . Given the results of the classical validation test, in which the model was rejected for each measured location, the statistics concerning V_{imp} and h are revised for the sake of illustration. In practice, such a revision could come as the result of additional data concerning input conditions to the real-world system, and this helps make the point that the computational model being validated is statistical in nature. The distribution parameters are now given as $\mu = 4.25$ rad/sec, and $\sigma = 0.24$ rad/sec for V_{imp} ; and $\mu = 1.48''$ and $\sigma = 0.05''$ for h . The same linearly-iterpolative, non-parametric response function is used based on the battery of LS-Dyna runs conducted.

In the context of Bayesian updating, the mean peak stress μ at each location is itself considered to be a random variable, and the measured data is used to update the governing distribution. A prior density function is assigned to μ to reflect the degree of belief surrounding its value, and for this case the distribution is assumed to be normal. In order to compute the

posterior density (numerator in Eq. 4.17), it is necessary to apply Bayes' theorem, and therefore the likelihood function for $\mu = \theta_0$ is found via:

$$f(x | \theta_0) = \prod_{i=1}^n \frac{1}{\sqrt{2\pi\sigma}} e^{\left[-\frac{1}{2}\left(\frac{x_i - \theta_0}{\sigma}\right)^2\right]} \quad (4.18)$$

For a prior normal density function with known standard deviation σ , it can be shown that the updated density function, or posterior distribution, will also be normal. The pair of distributions (prior and posterior) is known as a conjugate pair, and considerable mathematical effort can be saved by choosing a prior density with a known posterior form. Several examples of conjugate distributions are given by Ang and Tang (1975). For the example at hand, with a normal underlying random variable (peak stress) and known σ (say, from observed confidence bounds on the measured stress levels), if the prior mean and standard deviation of the normally-distributed parameter μ to be updated are denoted as μ'_μ and σ'_μ , respectively, then the posterior distribution for μ is also normal with updated parameters:

$$\mu''_\mu = \frac{\mu'_\mu (\sigma^2 / n) + \bar{x} \sigma'^2_\mu}{\sigma^2 / n + (\sigma'_\mu)^2} \quad (4.19)$$

$$\sigma''_\mu = \sqrt{\frac{(\sigma'_\mu)^2 (\sigma^2 / n)}{(\sigma'_\mu)^2 + \sigma^2 / n}} \quad (4.20)$$

where \bar{x} is the sample average of the measured data, n is the number of measured data points, and σ is the known standard deviation at each location, taken to be between 500-600 psi for the purposes of this exercise, depending on the amount of observed signal variability in the channel used to measure each location. The prior distribution parameters μ'_μ and σ'_μ are assigned using the results of the Monte Carlo simulation. The predicted mean peak stress at each location is taken as the point estimate of μ'_μ , and σ'_μ is found based on an assumed coefficient of variation

(σ/μ) of 10%. Table 4.8 summarizes the results of the Bayesian validation test using five drop test results for locations along the cylinder leading edge.

Table 4.8 – Model validation metric, B and confidence, C

Location	n	Prior Parameters	Posterior Parameters	Bayes Factor, B	C
Sta6_CL	5	$\mu_{\mu}' = 10,042.7$ $\sigma_{\mu}' = 1,004.3$	$\mu_{\mu}'' = 8,918.0$ $\sigma_{\mu}'' = 259.2$.00032	.0003
Sta9_CL	5	$\mu_{\mu}' = 9,783.6$ $\sigma_{\mu}' = 978.4$	$\mu_{\mu}'' = 8,831.6$ $\sigma_{\mu}'' = 218.0$.00032	.0003
Sta12_CL	5	$\mu_{\mu}' = 8,335.3$ $\sigma_{\mu}' = 833.5$	$\mu_{\mu}'' = 8,279.9$ $\sigma_{\mu}'' = 216.0$	3.735	.789
Sta15_CL	5	$\mu_{\mu}' = 8,147.0$ $\sigma_{\mu}' = 814.7$	$\mu_{\mu}'' = 6,995.8$ $\sigma_{\mu}'' = 254.9$.00012	.0001

It can be seen that only the model prediction for Sta12_CL is accepted with any significant confidence. There is almost zero support for the model prediction at the other three measured locations.

Note that these tests are conducted using model output and experimental data of one type (von Mises stress), and from discrete locations only. A multivariate Bayesian formulation will test the aggregate model prediction for multiple quantities and/or locations in space or time; however, this is difficult to implement for practical applications due to computational expense. The reader is referred to Rebba (2005) for a discussion concerning the computational issues that must be addressed.

4.6 Summary and Conclusions

This chapter presents the experimental procedures involved with water impact testing of a hinged-cylinder assembly for validation of the corresponding LS-Dyna finite element model with uncertainty considerations included. A detailed procedure is described for crafting of a thin-walled aluminum cylinder and accompanying splash tank for conducting experimental impact tests on a free water surface. The data acquisition system and necessary signal conversion equations are presented in order to fully describe the manner in which the stress history data was collected for the cylinder impact tests. Batteries of drop tests are conducted so as to provide samples of data that sufficiently capture the random variation in the response quantities of interest.

Straightforward qualitative validation is conducted, in which the model predictions are visually compared to test data so as to check for overall loading trends and general agreement. Though this qualitative exercise is not sufficient by itself for a rigorous model validation and resulting high confidence, it does serve as a necessary and useful step in the validation process. Indeed, if a simple visual comparison of test data and model output shows obvious, fundamental disagreement, then it seems unlikely that a rigorous quantitative validation will increase confidence in the model. Quantitative validation approaches presented cover classical as well as Bayesian methods for evaluating model accuracy using available data. The examples shown include validation performed at several discrete points on the cylinder surface.

There are some promising indications concerning the LS-Dyna cylinder model performance resulting from the qualitative phase of validation. General trends in the stress wave propagation through the cylinder wall during the water impact appear to be captured by the finite element model. However, the results of the quantitative validation tests lead mostly to model

rejection. One option for addressing this is to perform further tuning and calibration to the finite element model by adjusting parameters such as elastic modulus E and density ρ . An example of the effects of such tuning can be seen in Fig. 4.17, where the elastic modulus E is increased.

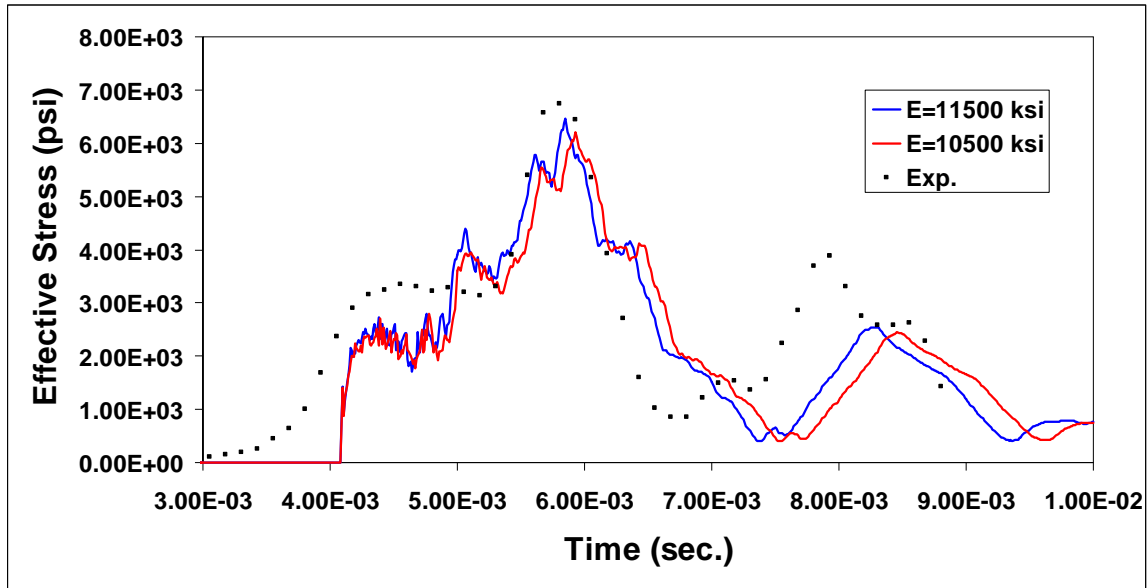


Fig. 4.17 – Tuning effect for model parameter, E

The peak stress is seen to increase somewhat as a result of the higher elastic modulus, and the phase shift is towards that of the measured signal. However, it is clear that additional adjustments to the model are needed. In particular, the predicted stress history is observed to dampen considerably following the initial stress peak, to an extent greater than what is recorded from laboratory testing. Thus far, tuning efforts have had difficulty improving model prediction at all locations on the cylinder wall. For example, increasing the elastic modulus E within the LS-Dyna input file typically results in better agreement with test data for some locations, but reduced agreement for others. Figs. 4.18 and 4.19 show the tuned effective stress history for two locations resulting from a 10% increase in the elastic modulus E .

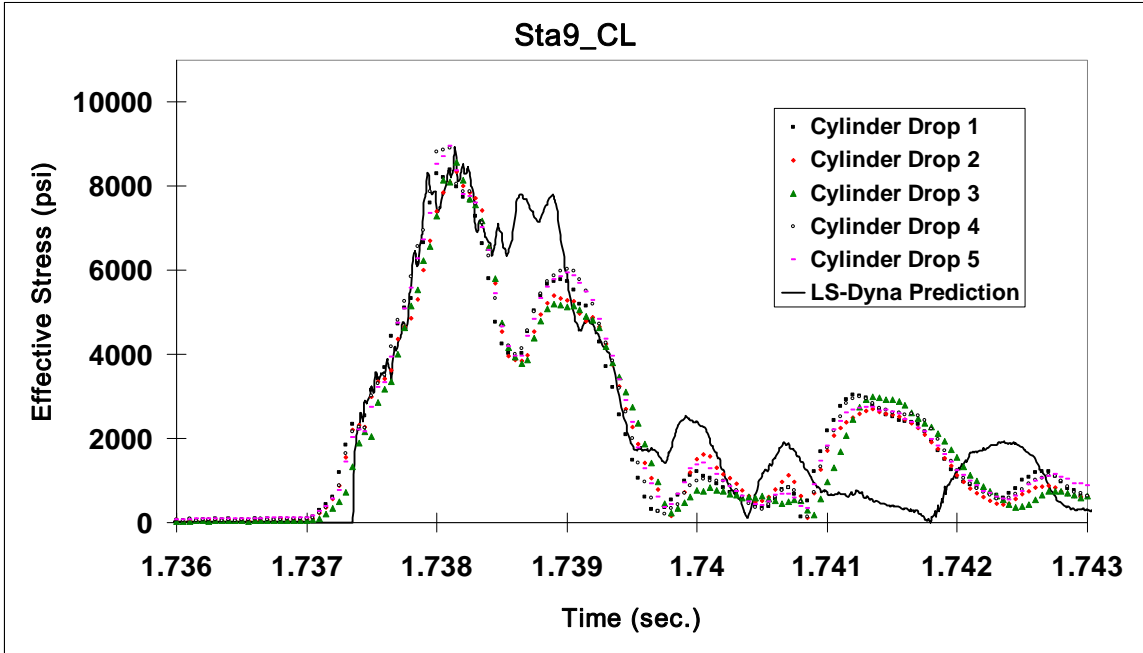


Fig. 4.18 – Tuned LS-Dyna prediction and measured water impact data for Sta9_CL

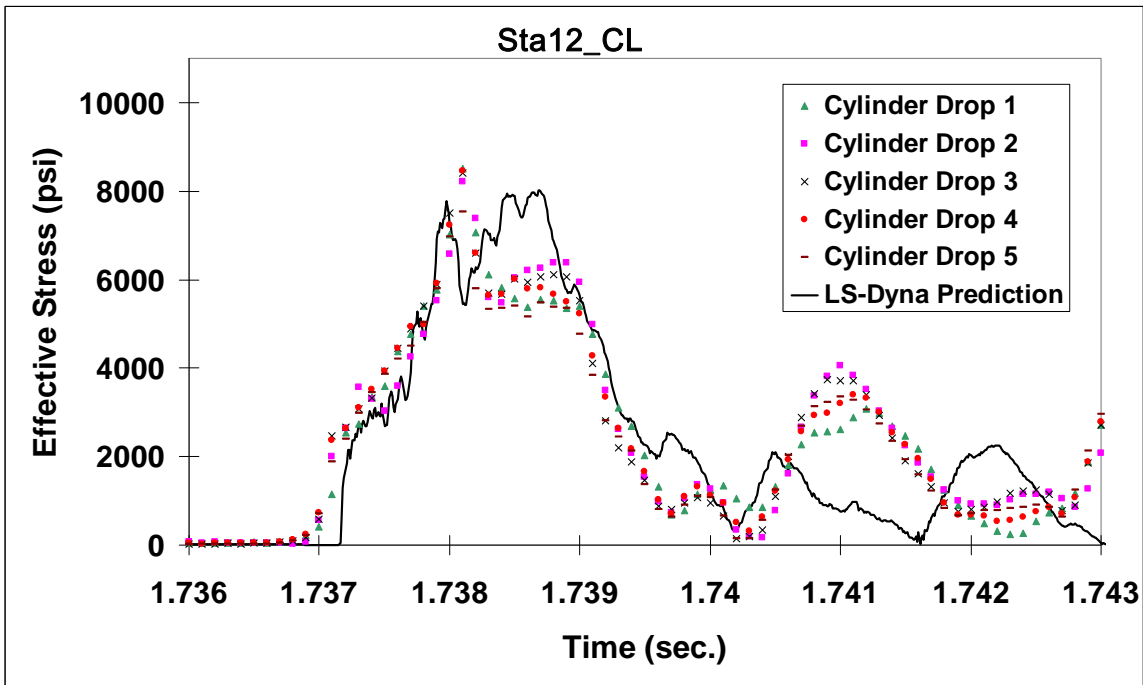


Fig. 4.19 – Tuned LS-Dyna prediction and measured water impact data for Sta12_CL

It can be seen by comparing to Fig. 4.16b that the tuning serves to bring the peak stress prediction for Sta9_CL (Fig. 4.18) into better agreement with the measured peak stress values. The same is true for Sta12_CL (compare to Fig. 4.16c), though the peak stress is not in phase with the measured peak. However, Fig. 4.19 shows that the tuning serves to bring the overall impact stress curve into alignment with the measured data. A similar procedure can be conducted for additional locations on the cylinder wall.

In this study, there are errors and uncertainties present both on the modeling side as well as in the laboratory testing. Numerical error within the finite element formulation of the cylinder impact problem was investigated in Chapter 3, and as a result of the verification exercise, the fluid and structural meshes are carefully chosen for compatibility. Issues such as the iterative coupling algorithm needed to keep the fluid and structure domains in alignment as well as the presence of hourglass energies needed for numerical stability contribute additional uncertainty. Despite several sources of experimental uncertainty such as ambient electrical noise and slight variations in the assembly alignment between drops, the measured stress histories in the cylinder wall show strong, repeatable correlation from one test to the next. With both the numerical and experimental uncertainties sufficiently understood and quantified, model tuning and calibration is demonstrated for discrete locations on the cylinder surface.

CHAPTER V

SRB SPLASHDOWN FAILURE ANALYSIS

5.1 Introduction

In recent years, increased attention has been focused on the topic of structural failure resulting from impact with a free water surface. In some instances of fluid-structure impact the precise structural response mechanism leading to the failure is unknown. The SRB forward skirt damage has been characterized as a buckling phenomenon (McFadden 1999), thought to be induced by the pressure spike that results when the SRB rolls over from vertical and the forward skirt experiences “slapdown” on the free water surface. Photographs of the damaged SRB forward skirts show failure patterns often associated with structural buckling. Fig. 5.1 shows one example of a recovered SRB forward skirt that experienced damage as a result of the splashdown sequence.

The term “buckling” is often used by both engineers and laymen to refer to a wide variety of structural failures, typically those in which the collapse is sudden and irreversible. Additionally, the term is also frequently used to refer to the deformed shape of certain collapsed structures, usually characterized by folds or ripples in what is ordinarily a smooth surface. This widespread usage of the term often results in some linguistic imprecision concerning exactly what sorts of structural failures qualify as buckling.



Fig. 5.1 – SRB forward skirt splashdown-induced damage

In previous analyses conducted by the author (Mitchell 2003; Mitchell and Mahadevan 2004) numerical stress history predictions are made using the MSC.Dytran finite element software, as seen in Fig. 5.2.

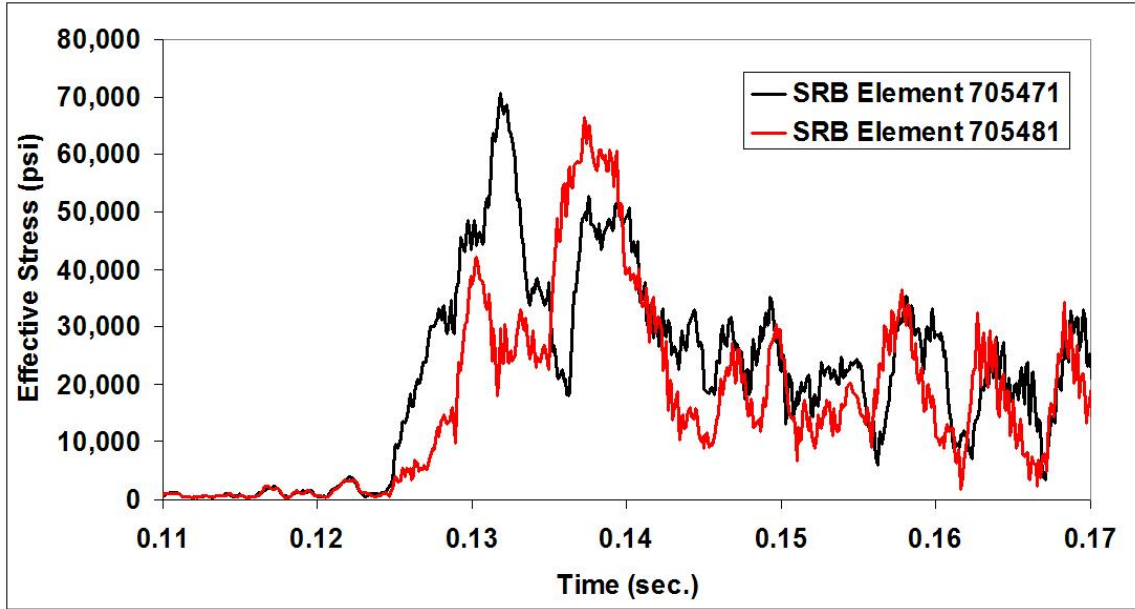


Fig. 5.2 – Representative stress history prediction by Dytran

The stress history plot shows the transient von Mises stress in two elements of the forward skirt of the SRB during a Dytran simulation of a water splashdown test with specific impact velocities and trajectories. However, the von Mises stress alone is not a sufficient indicator of the damage such as that observed in the SRB forward skirt. The von Mises criterion is useful for prediction of plastic yielding, but exceedance of the yield stress does not necessarily result in the deformations patterns witnessed in the damaged SRB forward skirts. In the case of the Dytran simulations, numerical instabilities are frequently encountered following the water impact and the analyses terminate prematurely, though peak stress predictions such as those seen in Fig. 5.2 are still obtained. The unbounded nodal deflections that precipitate these premature terminations typically originate in the vicinity of the forward skirt, and there is some question as to whether this indicates buckling in that region. However, without Dytran results that actually predict post-buckled behavior (i.e., deformation patterns), there can be little confidence assigned to the model

prediction. Therefore a consistent, quantifiable buckling definition is needed in order to conduct a more complete risk assessment of the forward skirt damage resulting from water impact.

In nearly all scenarios, full-scale, potentially destructive experimental splash testing of large aerospace structures like the SRB is not a cost-effective approach to research and design. Therefore in this study, failure analysis of the forward skirt of the impacting SRB is investigated using structural response predictions generated from nonlinear finite element analysis. The commercial analysis code LS-Dyna is used to simulate the forward skirt impacting on the free water surface. Note that the question of whether damage to the SRB during splashdown is possible has already been answered by real-world experience. Therefore this work aims to accurately model the SRB splashdown conditions, analyze the resulting structural response including large deflections and plastic yielding, and then determine whether the term “buckling” is applicable to the resulting damage.

The lack of available SRB flight data showing the stress history within the forward skirt makes it difficult to precisely know the exact mechanism (or combination of mechanisms) at work. To the knowledge of the author, no post-failure forensic work such as electron spectrometry has been conducted to give a better understanding of the failure mode. This chapter discusses the possible means of failure of water-impacting structures generally, and presents results of an attempt to better characterize the SRB forward skirt failures using nonlinear finite element analysis.

5.2 Buckling Overview and Background

Fluid-structure impact events involve dynamic loading conditions that can lead to sudden and severe structural damage, with the resulting deformation patterns often described as buckling.

However, buckling is a failure mechanism that historically has proven quite difficult for engineers in all structural design fields to predict, and has resulted in many catastrophic structural collapses (Bushnell 1985). In this section, previous research into structural buckling is summarized, with particular attention given to dynamic pulse buckling of cylinders.

5.2.1 Buckling Theories and Experiments

It is generally known that many engineering structures are susceptible to buckling failure under the right combination of loadings, even though the stresses in the individual structural members may be well below those which cause plastic yielding. Linear structural analysis problems deal with conditions in which the deflections within a structure are directly proportional to the applied load. However, structural buckling is characterized by a disproportionate increase in displacement due to only a small increase in the applied loading. Buckling is therefore a nonlinear phenomenon (Brush and Almroth 1975).

Nonlinear behavior can be initiated within a structure in one of two ways: either through physical or geometrical changes within the structure. Physical nonlinearity occurs when the stresses induced within the structure exceed the yield strength of the material, thus leading to nonlinear load-deflection curves. Geometrical nonlinearity occurs when deflections become large enough such that rotational terms can no longer be ignored and load paths within the structure are significantly altered.

Cylindrical structures such as the SRB may experience sudden buckling failure due to both axial loadings as well as lateral pressures. Buckling of cylindrical structures can occur due to static (also quasi-static) loading as well as dynamic loading, as in the case of fluid-structure impact. A dynamic load factor (DLF) can be defined for a structure as the ratio of the dynamic

buckling load to the static buckling load (Yaffe and Abramovich 2003). Dynamic buckling can be further divided into vibration buckling caused by oscillatory loadings and pulse buckling due to a single load of certain amplitude, shape, and duration (Lindberg and Florence 1987).

Dynamic pulse buckling of cylindrical structures has been investigated extensively through both experimentation and numerical analyses. Two different analytical approaches have been derived for thick cylinder (plastic flow) and thin-cylinder (elastic) pulse buckling resulting from uniform external pressures. The plastic flow or tangent modulus model for dynamic pulse buckling was derived by Abrahamson and Goodier (1962) and assumes a completely plastic state with strain hardening. The dominant wavelength of buckling or critical buckling mode n_{cr} is given as:

$$n_{cr}^2 = \frac{1}{2}(s^2 + 1) \quad (5.1)$$

where $s = 12\sigma_m a^2 / E_h h^2$. The radius and thickness of the cylinder are given by a and h respectively, σ_m is the average flow stress, and E_h is the strain hardening modulus. Lindberg and Florence (1987) defined the buckling threshold for thick-walled cylinders in terms of the critical impulse I_{cr} (pressure applied over time) as:

$$I_{cr} = \sqrt{3} \rho c a \sqrt{\frac{E_h}{E}} \left(\frac{h}{a} \right)^2 \quad (5.2)$$

where ρ is the mass density, c is the speed of sound through the material, and E is Young's modulus.

The type of buckling (elastic or plastic) that occurs in a cylinder subjected to a pressure pulse depends on the magnitude of the pulse as well as the duration. Anderson and Lindberg (1968) developed a series of critical curves for buckling of cylinders based on the elastic and

plastic material properties, the radius-to-thickness (a/h) ratio, and length-to-diameter ratio. These curves are defined within the pressure (P) and impulse (I) plane as shown in Fig. 5.3.

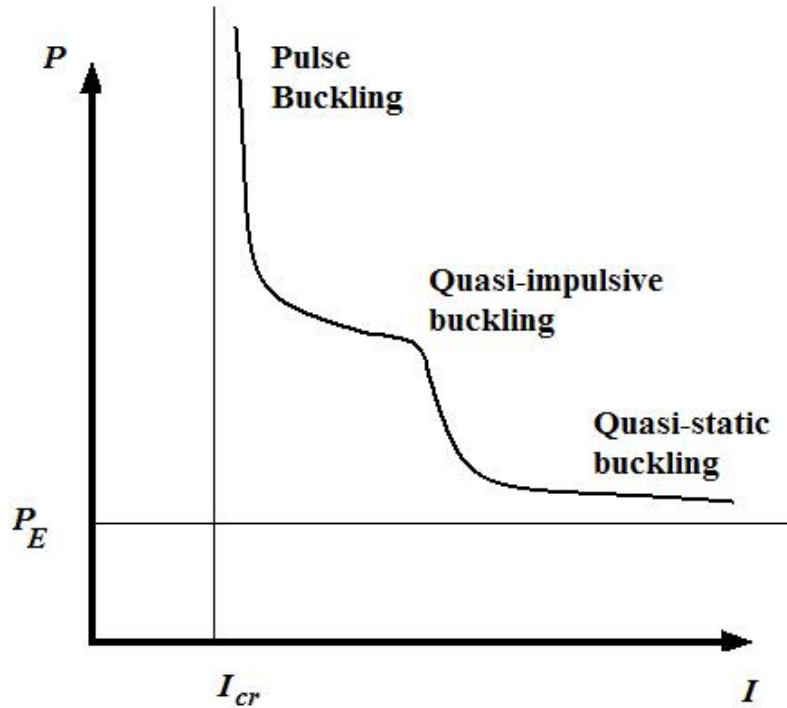


Fig. 5.3 – Schematic for buckling in pressure-impulse plane

Cylinders subjected to short-duration, high-pressure impulse loads experience pulse buckling according to plastic flow theory, while quasi-static loads induce elastic buckling. Note that the critical impulse loading I_{cr} is given by Eq. 5.2. The static collapse pressure required to induce elastic buckling, P_E can be approximated by:

$$P_E = 0.92E \left(\frac{a}{L} \right) \left(\frac{h}{a} \right)^{5/2} \quad (5.3)$$

However, this expression is only valid for $100 \leq Z \leq 10(a/h)^2$, where $Z = (1 - \nu^2)^{1/2} L^2 / ah$. Anderson and Lindberg (1968) noted that for quasi-impulsive loadings neither the elastic nor

plastic flow buckling theories fully describe the deformation of the cylinders since the effects of strain hardening as the buckles become large are neglected.

Later work by Kirkpatrick and Holmes (1988) incorporated nonlinear finite element codes to capture the effects of strain hardening. They used the nonlinear DYNA3D computer code, the predecessor to LS-DYNA used in this work, to analyze the buckling response of cylinders subjected to lateral pulse loadings. They included initial shape and loading imperfections in the FEM model in order to predict the final buckling shape of the cylinder. A mesh refinement study showed that roughly 10 elements per buckle wavelength were needed to accurately predict the final buckled shape.

Pegg (1991) presented results from a finite element investigation of infinite cylinders with a/h ratios varying from 10 to 300. It was noted that for midrange a/h ratios (which cover many practical structural members; forward skirt $a/h \sim 156$) that neither elastic pulse nor plastic flow buckling theory adequately predicted the cylinder response. Subsequent work (Pegg 1992) used finite element analysis to examine ring-stiffened cylinders. It was found that pulse buckling theory can still be used to obtain reasonable results, but that effective a/h ratios must be developed for the ring-stiffened cylinders. A comprehensive presentation of both finite element and finite differencing techniques applied to both stiffened and unstiffened cylinders, for pulse loadings of various magnitudes and durations is given by Pegg (1994). It is noted that dynamic buckling occurs at much higher loadings and with much smaller wavelengths than static buckling failure.

It should be noted that buckling investigations have traditionally been conducted through experimentation, and that only with recent advances in computational power have detailed numerical buckling investigations been widely undertaken. Even now, for complex structural

systems, full-scale experimental testing is often the ideal method of analysis, but also often prohibitively expensive. For dynamic, impact-induced buckling problems in particular, the difficulty associated with accurately measuring the various component stresses and moments within the structure make experimental analysis very challenging. As a result, many experimental buckling analyses compare theoretical buckling loads and deformation patterns to observed structural behavior (see Singer et al. 1998, Vol 2).

Early buckling studies in the 19th century resulted in empirical relationships and guidelines for structural stability. Some of the earliest experimental buckling studies date to 1845, when Fairbairn observed wrinkles and other anomalies while performing tests on scaled box beams for a railway bridge (Timoshenko 1953). In the 20th century, theoretical studies became more common, but there was often little correlation with experimental validation tests (Singer et al. 1998, Vol. 1), even for carefully controlled, static buckling investigations. Extreme sensitivity to initial imperfections in the structural geometry has often been cited as an explanation for differences in experimental results and buckling theory, though advances in manufacturing technology have led to better agreement in some cases (see e.g., Blachut 2002).

For dynamic pulse buckling, several of the previously cited research efforts have included experimental testing in conjunction with theoretical derivations. Lindberg (1968) presented experimental results for very thin cylindrical shells that were in agreement with pulse buckling theory. Lindberg and Florence (1987) also presented results from many pulse buckling studies and comparisons to theory. More recently, experimental work has served as the baseline for comparison used in the development of many numerical methods. Kirkpatrick and Holmes (1988) used explosives to generate pressure pulses applied to thin aluminum cylindrical shells, and compared the observed results to the DYNA3D predictions. Additional recent experimental

work with cylindrical shells includes that of Karagiozova and Jones (1998), in which observed axisymmetric buckling patterns are compared to predictions from a discrete spring-mass model. Barlag and Rothert (2002) derive stability conditions for predicting localized and global buckling pressures for ring-stiffened cylindrical shells, and compare the predictions to experimental results. Also, Mathon and Limam (2006) present experimental buckling results for pressurized cylinders subjected to bending loads.

In Singer et al. (1998, Vol. 1) eight primary motivations for experimental buckling analysis in the modern age of increasing computer power are listed, and one of these motivations deals explicitly with fluid-structure interaction problems such as the SRB problem investigated here:

“For buckling under dynamic loading and in fluid-structure interaction problems. These are areas where computation is cumbersome, expensive, and difficult to interpret reliably. Experiments may therefore be preferable at this stage, though they too present many difficulties. Theory and numerical computations should follow these experiments closely, to reinforce and broaden the partial understanding of the phenomena that the experiments will provide.”

Though this research does entail experimental testing (presented in Chapter 4), it is not the aim of the small-scale cylinder drop tests to shed insight on the failure mechanism leading to the forward skirt damage. The SRB is a very complex structural system, and therefore scaled structural modeling with sufficient fidelity to capture the observed deformation patterns is prohibitively expensive. Therefore, in this chapter a numerical investigation of the SRB forward skirt buckling damage is presented.

5.2.2 SRB Splashdown Buckling

The previous discussion of dynamic pulse buckling is presented due to the seeming applicability of the failure mechanism to the damage observed in the SRB forward skirt. Recall from Chapter 2 that the splashdown sequence is characterized by a large acceleration spike occurring several seconds after initial water impact, as the SRB rolls over and slaps the free water surface. The pressure pulse resulting from this impact is believed to be responsible for the observed damage; however, the question remains as to whether this damage can technically be classified as pulse buckling.

It should be noted that the dynamic pulse buckling theory mentioned above pertains to pressure loads applied evenly about the circumference of uniform, isotropic cylinders, whereas the SRB splashdown sequence only results in impact pressure applied to one side of the forward skirt. Additionally, the forward skirt contains ring stiffeners and the thickness varies from 0.25" – 0.75" about the circumference, so effective values for L and h must be used when computing the critical impulse and pressure loads shown by Eqs. 5.2 and 5.3, respectively. Also, for the SRB forward skirt, the Z parameter used for calculating the static collapse pressure P_E is less than 100, even using non-conservative assumptions on the effective L and h . Therefore application of the pulse buckling loading parameters to the SRB forward skirt is not a straightforward procedure. Pegg (1994) stresses that a wide range of practical cylinder geometries falls outside the range for which pulse buckling theory can be directly applied, and recommends numerical techniques such as the finite element method for analysis of buckling mechanisms.

The buckled cylinders presented in the pulse buckling studies all show buckling patterns in a longitudinal orientation (see e.g., Anderson and Lindberg 1968, and Kirkpatrick and Holmes

1988), that is, the deformations patterns run parallel to the long axis of the cylinder. Recall from Fig. 5.1 the buckling pattern of the forward skirt of the SRB. The buckled wavelengths are confined to a region just above the interface with the steel motor casing, and run more in the circumferential direction or at roughly 45° angles. These buckling patterns observed in the SRB are more similar to those observed in axial compression and bending situations, such as those shown by Mathon and Limam (2006) and Karagiozova and Jones (2000). The physics of the splashdown sequence seem to imply a pressure pulse on the forward skirt due to the slapdown effect very similar to the pulse buckling loads in the cited literature, yet the observed damage patterns indicate buckling due more to an axial compressive or bending load. Furthermore, the pure pulse buckling failure mechanisms described by Lindberg and Florence (1987) are characterized by a very high number of buckles with short wavelengths, and impulse loads of very short duration and high pressure. Pure pulse buckling, according to the curves derived by Lindberg and Anderson (1968) typically occur at pressures several orders of magnitude higher than the elastic collapse pressure, and these pressures are applied over a loading period that is on the same order as the natural period of the cylinder. In experimental studies such as Lindberg (1964), such loads are applied to cylinders using explosives. Given all of these considerations, it seems unlikely that pure pulse buckling is the sole mechanism at work with the SRB forward skirt damage. It is more likely that the pressure pulse resulting from water impact combined with internal forces and moments generated during the splashdown sequence lead to the observed damage.

In recent years nonlinear finite element analysis has been widely used for predicting the buckling behavior of practical engineering structures for which it is difficult to apply analytical buckling theories directly. As will be shown, such an approach can accurately predict

deformation patterns resulting from structural failure. However, if one seeks insight into the nature of the failure mechanism beyond the final deformed state (i.e. elastic buckling versus simple plastic yielding), further analysis of the model results is required. This work seeks to gain a better understanding of the failure mechanism responsible for the SRB forward skirt damage. Therefore output from the LS-Dyna model used in this study is used to evaluate several classical shell stability conditions, to be presented subsequently.

5.3 Fundamental Shell Buckling Equations

It is helpful to begin a discussion of shell buckling theory with an introduction of the constitutive forces and moments acting on a plate element (Brush and Almroth 1975; Chajes 1974):

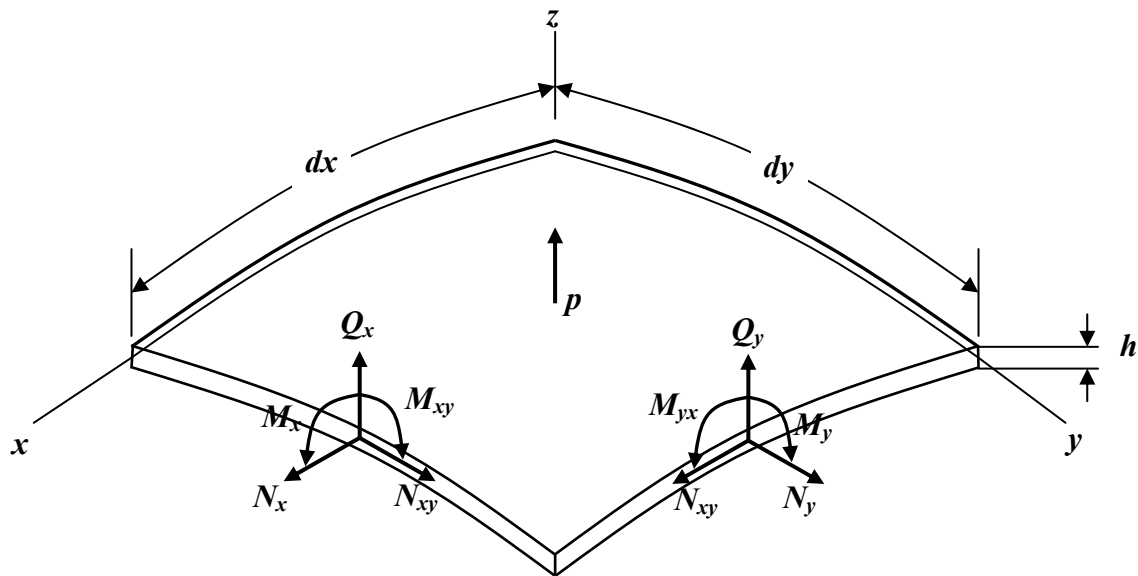


Fig. 5.4 – Schematic of plate element for bending analysis

The forces and moments shown along each edge of the plate element in Fig. 5.4 are given by:

$$N_x = \int_{-h/2}^{h/2} \bar{\sigma}_x dz \quad N_y = \int_{-h/2}^{h/2} \bar{\sigma}_y dz \quad (5.1a)$$

$$N_{xy} = \int_{-h/2}^{h/2} \bar{\tau}_{xy} dz \quad N_{yx} = \int_{-h/2}^{h/2} \bar{\tau}_{yx} dz \quad (5.1b)$$

$$Q_x = \int_{-h/2}^{h/2} \bar{\tau}_{xz} dz \quad Q_y = \int_{-h/2}^{h/2} \bar{\tau}_{yz} dz \quad (5.1c)$$

$$M_x = \int_{-h/2}^{h/2} \bar{\sigma}_x z dz \quad M_y = \int_{-h/2}^{h/2} \bar{\sigma}_y z dz \quad (5.1d)$$

$$M_{xy} = \int_{-h/2}^{h/2} \bar{\tau}_{xy} z dz \quad M_{yx} = \int_{-h/2}^{h/2} \bar{\tau}_{yx} z dz \quad (5.1e)$$

Where N_x , N_y , N_{xy} , and N_{yx} are the in-plane normal and shearing force intensities, Q_x and Q_y are the transverse shearing force intensities, M_x and M_y are the edge bending moment intensities, and M_{xy} and M_{yx} are the twisting moment intensities. Note that the $\bar{\sigma}$ and $\bar{\tau}$ terms represent the normal and shear stress components with variation through the plate thickness, not simply the mid-plane stress. The eight expressions above can be consolidated by virtue of $\bar{\tau}_{xy} = \bar{\tau}_{yx}$, therefore $N_{xy} = N_{yx}$ and $M_{xy} = M_{yx}$. The Kirchhoff assumptions (Novozhilov 1953) can be used to simplify the equations further:

1) transverse shearing and normal strains may be neglected when deriving the kinematic relations, because normals to the undeformed mid-plane are assumed to remain straight and inextensional during deformation.

2) transverse normal stresses are neglected in the stress-strain relations because they are assumed to be small compared with other stress components.

The Kirchhoff assumptions allow the displacement components (\bar{u} , \bar{v} , and \bar{w}) at any point through the plate thickness h to be expressed in terms of the mid-plane (i.e., $z=0$) displacements.

$$\bar{u} = u + z\beta_x \quad (5.2a)$$

$$\bar{v} = v + z\beta_y \quad (5.2b)$$

$$\bar{w} = w \quad (5.2c)$$

The β terms represent rotation of mid-plane normal relative to the x and y -coordinate directions, respectively. The displacement components are shown graphically in Fig. 5.5, which shows the plate and mid-plane surface normal before and after deformation.

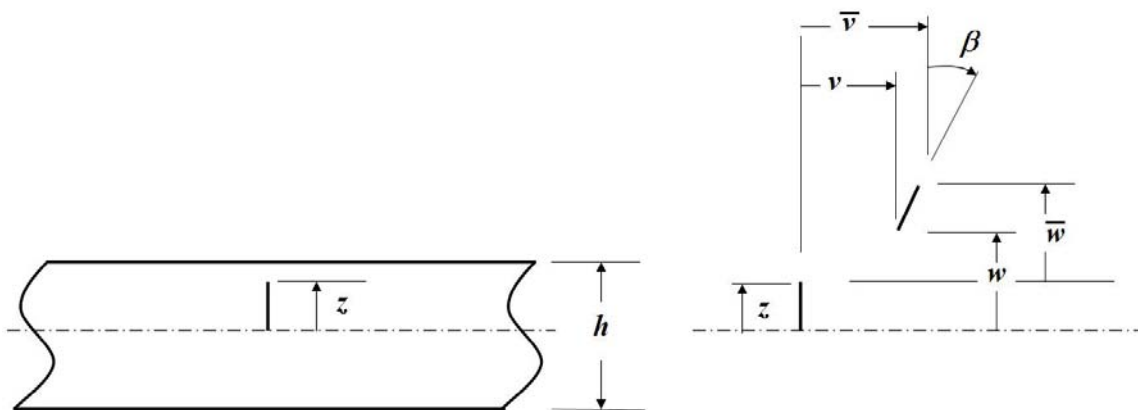


Fig. 5.5 – Mid-surface normal before and after deformation

For the intermediate class of deformations, with small strains, small rotations about the x and y coordinate axes, and negligible rotations about to the z coordinate axis, the strain components through the plate thickness can be related to the displacements above by:

$$\bar{\varepsilon}_x = \frac{\partial \bar{u}}{\partial x} + \frac{\partial^2 \bar{w}}{2\partial x^2} \quad (5.3a)$$

$$\bar{\varepsilon}_y = \frac{\partial \bar{v}}{\partial y} + \frac{\partial^2 \bar{w}}{2\partial y^2} \quad (5.3b)$$

$$\bar{\gamma}_{xy} = \frac{\partial \bar{v}}{\partial x} + \frac{\partial \bar{u}}{\partial y} + \frac{\partial^2 \bar{w}}{\partial x \partial y} \quad (5.3c)$$

Also, for the intermediate deformation assumption, rotation of the mid-plane normals, β_x and β_y , is equal to $-\frac{\partial w}{\partial x}$ and $-\frac{\partial w}{\partial y}$, respectively.

The generalized Hooke's law for thin plates (i.e., $\sigma_z = 0$; see Kirchhoff assumption 2 above) relates these strain components to stress via:

$$\bar{\sigma}_x = \frac{E}{1-\nu^2} (\bar{\varepsilon}_x + \nu \bar{\varepsilon}_y) \quad (5.4a)$$

$$\bar{\sigma}_y = \frac{E}{1-\nu^2} (\bar{\varepsilon}_y + \nu \bar{\varepsilon}_x) \quad (5.4b)$$

$$\bar{\tau}_{xy} = \frac{E}{2(1+\nu)} \bar{\gamma}_{xy} \quad (5.4c)$$

Using these stress-strain relations with the force and moment intensities of Eqs. 5.1a-e gives the force intensities as:

$$N_x = \frac{Eh}{1-\nu^2} (\varepsilon_x + \nu \varepsilon_y) \quad (5.5a)$$

$$N_y = \frac{Eh}{1-\nu^2} (\varepsilon_y + \nu \varepsilon_x) \quad (5.5b)$$

$$N_{xy} = \frac{Eh}{1-\nu^2} \left(\frac{1-\nu}{2} \right) \gamma_{xy} \quad (5.5c)$$

While the moment intensities are:

$$M_x = -\frac{Eh^3}{12(1-\nu^2)} \left(\frac{\partial^2 w}{\partial x^2} + \nu \frac{\partial^2 w}{\partial y^2} \right) \quad (5.6a)$$

$$M_y = -\frac{Eh^3}{12(1-\nu^2)} \left(\frac{\partial^2 w}{\partial y^2} + \nu \frac{\partial^2 w}{\partial x^2} \right) \quad (5.6b)$$

$$M_{xy} = \frac{Eh^3}{12(1-\nu^2)} (1-\nu) \frac{\partial^2 w}{\partial x \partial y} \quad (5.6c)$$

5.3.1 von Karman Plate Equilibrium Equations

Brush and Almroth (1975) and Chajes (1974) show the derivation of the plate equilibrium equations by summing the forces and moment intensities defined above for the plate element shown in Fig. 5.4. The equilibrium equations are:

$$\frac{\partial N_x}{\partial x} + \frac{\partial N_{xy}}{\partial y} = 0 \quad (5.7a)$$

$$\frac{\partial N_y}{\partial y} + \frac{\partial N_{xy}}{\partial x} = 0 \quad (5.7b)$$

$$D \left(\frac{\partial^4 w}{\partial x^4} + 2 \frac{\partial^4 w}{\partial x^2 \partial y^2} + \frac{\partial^4 w}{\partial y^4} \right) - N_x \frac{\partial^2 w}{\partial x^2} - N_y \frac{\partial^2 w}{\partial y^2} - 2N_{xy} \frac{\partial^2 w}{\partial x \partial y} = p \quad (5.7c)$$

Where D is the bending stiffness parameter, $D = Eh^3/12(1-\nu^2)$. These equilibrium equations are known as the von Karman large-deflection plate equations. They can also be derived from stationary potential energy theory (Brush and Almroth 1975).

5.3.2 Donnell Equilibrium Conditions for Cylinders

Extending the stability concepts upon which the plate equilibrium conditions are based to a circular cylindrical shell is shown by the Donnell equilibrium conditions. If one takes the plate element schematic in Fig. 5.4 and replaces the y terms with θ to indicate the circumferential direction about the cylinder wall, then the same summing of forces and moments yields:

$$r \frac{\partial N_x}{\partial x} + \frac{\partial N_{x\theta}}{\partial \theta} = 0 \quad (5.8a)$$

$$r \frac{\partial N_{x\theta}}{\partial x} + \frac{\partial N_\theta}{\partial \theta} = 0 \quad (5.8b)$$

$$D \left(\frac{\partial^4 w}{\partial x^4} + \frac{2}{r^2} \frac{\partial^4 w}{\partial x^2 \partial \theta^2} + \frac{1}{r^4} \frac{\partial^4 w}{\partial \theta^4} \right) + \frac{1}{r} N_\theta - \left(N_x \frac{\partial^2 w}{\partial x^2} - \frac{1}{r^2} N_\theta \frac{\partial^2 w}{\partial \theta^2} + \frac{2}{r} N_{x\theta} \frac{\partial^2 w}{\partial x \partial \theta} \right) = p \quad (5.8c)$$

Eqs. 5.8a-c represent the non-linear equilibrium conditions for cylindrical shells and are analogous to the von Karman plate equations given by Eqs. 5.7a-c. Note the presence of the additional r terms, indicating the significance of the cylinder radius on structural stability.

5.4 Numerical Buckling Analysis

Nonlinear finite element codes such as MSC.Dytran and LS-Dyna have been used extensively in structural buckling studies. There are several studies reported in which nonlinear finite element analysis codes have been employed to predict the deformed shape of helicopter fuselage sections resulting from water impact. Fasanella et al. (2003) compared experimental observations such as accelerations and material yielding to predictions from models developed with both MSC.Dytran and LS-Dyna. Majamaki (2002) employed Dytran simulations for initial proofing and general decision support regarding designs for a complex and expensive full-scale helicopter drop test. More recently, Hughes et al. (2008) used LS-Dyna to predict deformed shapes, including

buckling failures, of various components of a helicopter fuselage section following a water impact.

In this section the previously described von Karman (Eqs. 5.7a-c) and Donnell (5.8a-c) stability conditions will be compared with the computed structural response of a simple cylindrical structure in a quasi-static loading situation. The loaded cylinder is modeled using the LS-Dyna finite element software. The partial derivatives in the von Karman and Donnell stability conditions are evaluated by applying a finite difference type approach using the predicted response at several locations on the meshed cylinder wall, as shown in Fig. 5.6.

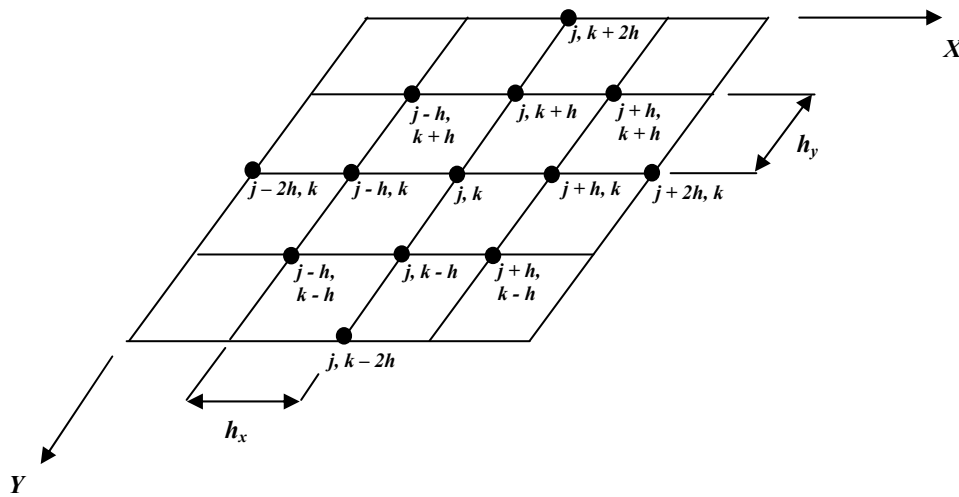


Fig. 5.6 – Output locations used to monitor von Karman and Donnell stability conditions

Using this configuration, the second and fourth partial derivatives of w from Eqs. 5.7c and 5.8c can be found by:

$$\left(\frac{\partial^2 w}{\partial x^2} \right)_{j,k} = \frac{w_{j+h,k} - 2w_{j,k} + w_{j-h,k}}{h_x^2} \quad (5.9a)$$

$$\left(\frac{\partial^4 w}{\partial x^4}\right)_{j,k} = \frac{w_{j+2h,k} - 4w_{j+h,k} + 6w_{j,k} - 4w_{j-h,k} + w_{j-2h,k}}{h_x^4} \quad (5.9b)$$

$$\left(\frac{\partial^4 w}{\partial x^2 \partial y^2}\right)_{j,k} \cong \frac{1}{h^4} [(w_{j+h,k+h} - 2w_{j+h,k} + w_{j+h,k-h}) - 2(w_{j,k+h} \dots \\ \dots - 2w_{j,k} + w_{j,k-h}) + (w_{j-h,k+h} - 2w_{j-h,k} + w_{j-h,k-h})] \quad (5.9c)$$

Note that the partial derivatives in the vertical (y) direction are found in the same manner. The purpose of the simple cylinder exercise is to show how the LS-Dyna model output can be compared to theoretical plate and cylinder stability conditions in order to determine whether the predicted damage can be termed buckling.

5.4.1 Quasi-Static Cylinder Example

The dimensions of the modeled cylinder chosen for this work are the same as that modeled for validation with the experimental cylinder-water impact study discussed in Chapter 4. The 30" cylinder with a 3.0" diameter is meshed using 28,294 nodes and 28,200 quadrilateral shell elements. A uniform compressive load is applied along the upper edge of the cylinder, and appropriate nodal constraints applied to prevent global instabilities. The cylinder thickness is varied along the length, both to reinforce the cylinder edges from boundary effects of loading and reaction forces, and to limit the number of elements that needed to be monitored for failure. The upper and lower sections of the cylinder are given a thickness of 0.1", followed by transition segments with a thickness of 0.05". The middle portion designated for buckling failure was given a thickness of 0.015".

LS-Dyna uses an explicit central-differencing technique to advance the transient analysis forward in time (Hallquist 2006). The updated structural geometry is then computed via:

$$a^n = M^{-1}[P^n - F^n + H^n] \quad (5.10)$$

where a^n is the vector of nodal accelerations at time step n , M is the diagonal nodal mass matrix, and P , F , and H are the external force, internal structural force, and hourglass vectors, respectively. The advantage to using the explicit approach, as opposed to implicit solvers, is the trivial inversion of the diagonal nodal mass matrix at each time step. The disadvantage is that the required time step for a stable solution is governed by the single element in the model with the highest natural frequency, ω_{max} . This requirement can result in extremely long computational times for analysis if the elements within the model are not sized carefully. It also presents challenges for conducting quasi-static analyses, since by their very nature they require a significant time period for analysis. One approach for overcoming these challenges and achieving manageable run times is to conduct mass scaling, or the artificial reduction of ω_{max} by increasing the density ρ and/or decreasing the stiffness, E . For this case, the stiffness of the cylinder material was lowered from that typical for aluminum to a value of 5.05E+06 psi. Also, the density was increased roughly 3 times to a value of .3058 lb/in³. There are also more advanced options available, such as selective mass scaling (Olovsson *et al.* 2005) wherein artificial terms are added to the mass matrix of the system in order to reduce the higher frequencies without affecting the lower frequencies. However in this example problem regular mass scaling is sufficient to achieve manageable analysis times.

The yield stress for the material was specified using an elastic-plastic material model within LS-Dyna. The plastic stiffness modulus was specified as 5.0E+05 psi, or 10% of the elastic modulus. The yield stress and the applied load could be adjusted to make the collapse of

the cylinder occur within the elastic or plastic range. An example of elastic buckling is shown in Fig. 5.7.

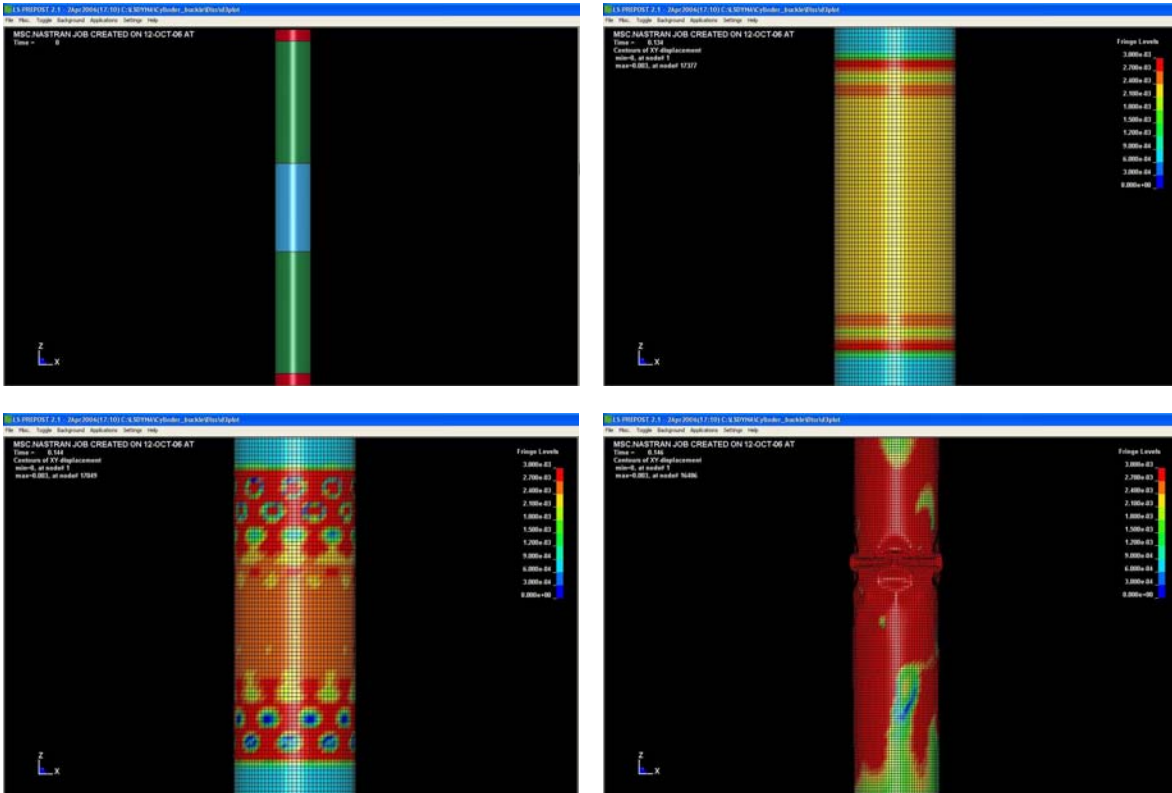


Fig. 5.7 – Cylinder geometry and elastic buckling due to quasi-static compressive loading

The deflection patterns certainly show all of the classically understood indications of buckling, both just prior to and immediately after collapse. It is interesting to note that the cylinder fails very close to the critical load for compressed circular cylinders predicted by the Donnell stability conditions. Using the derivation for straight compression from the Donnell equilibrium conditions given by Brush and Almroth (1975), the critical stress is given by:

$$\sigma_{cr} = \frac{Eh/a}{[3(1-\nu^2)]^{1/2}} \quad (5.11)$$

For the cylinder in this example, this gives a critical compressive stress of 30,552.5 psi, while the LS Dyna model shows collapse at 28,326.8 psi, a conservative prediction with percent difference of 7.28%. To ensure elastic buckling, the material is given a yield stress σ_y of 51,000 psi. The load-deflection curve becomes nonlinear at $t = 0.142$ sec. Fig. 5.8 shows the plot of the von Karman stability conditions of Eqs 5.7a-c as they are evaluated at each time step in the quasi-static analysis.

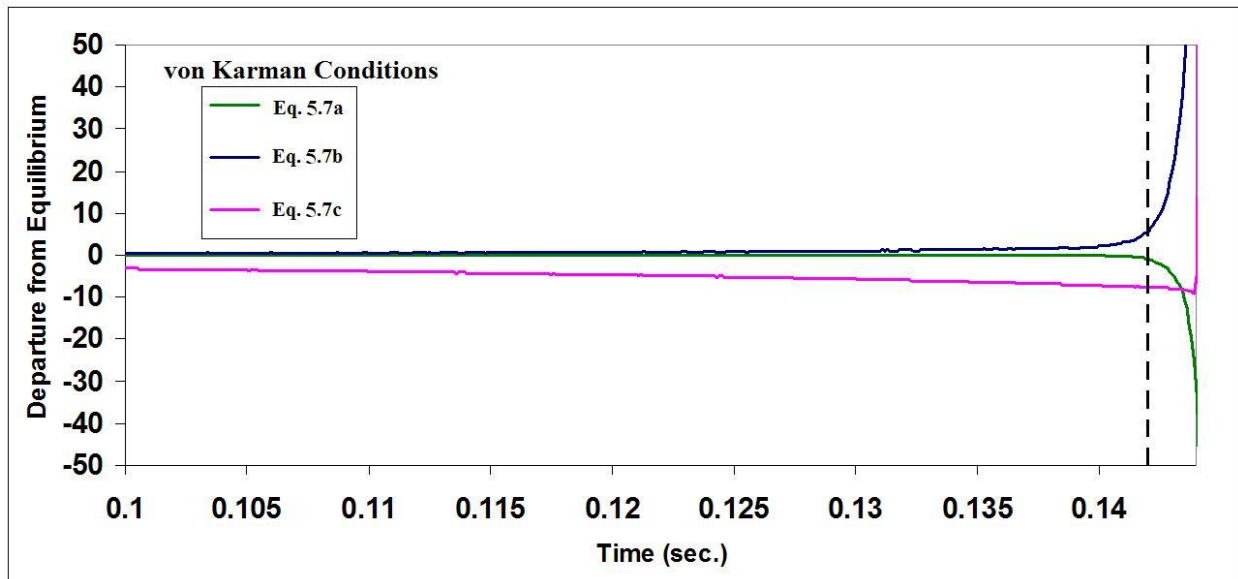


Fig. 5.8 – von Karman stability conditions (Eqs. 5.7a-c) during compressive buckling

As can be seen, once each curve deviates from equilibrium, cylinder collapse is eminent. The dashed line shows the point at which lateral deflections in the cylinder wall begin to grow nonlinearly with respect to the applied load. This shows that for this simple, quasi-static analysis, the von Karman stability theory accurately predicts the onset of buckling.

The same procedure is carried out for the Donnell cylinder equilibrium conditions, and the results show very similar behavior to the von Karman conditions. This is not surprising given the similarity between the von Karman and Donnell stability conditions.

The cylinder loading exercise is repeated with the yield stress σ_y reduced to 17,000 psi so that plastic deformation will occur within the cylinder wall prior to elastic buckling. Analysis of the von Karman and Donnell stability criteria shows similar behavior overall, however close inspection of the curves shows that once plastic yielding has begun, the smooth, monotonic behavior seen in the elastic buckling case (Fig. 5.8) prior to collapse is no longer maintained. Therefore it is possible to distinguish between the elastic and plastic buckling situations based upon evaluation of the von Karman and Donnell stability conditions.

5.4.2 SRB Forward Skirt Buckling

The preceding discussion is relevant to the SRB forward skirt splashdown problem owing to the visible buckling damage sustained on several missions (Clayton and Craft 1995). Figure 5.9 shows three of the five forward skirts that have experienced damage as a result of splashdown. In each instance, the damage is confined to the lowermost portion of the forward skirt, between the connection points with the steel solid rocket motor casing and the first circumferential stringer. Though the term “buckling” has been used by NASA engineers to describe damage generally, a comprehensive study of the failure mechanism has not been conducted. The question remains as to whether this forward skirt damage is actually the result of a true buckling mechanism or simply the result of plastic yielding, brittle fracture, or some other combination of mechanisms.



Fig. 5.9 – Three damaged SRB forward skirts

In this section, a numerical investigation is conducted into the forward skirt damage phenomenon in order to shed insight into the true nature of the failure mode.

As original sponsors of the splashdown damage study, engineers from the NASA Marshall Space Flight Center provided a NASTRAN finite element model of the SRB for analysis and risk assessment (Mitchell 2003; Mitchell and Mahadevan 2004). This is the same model discussed in Chapter 2 to predict the stress response of the SRB as a result of blunt water impact. One of the primary motivations for initially employing MSC.Dytran in this research is its relative compatibility with NASTRAN (both packages produced by MSC). It is believed that this compatibility provided a more straightforward SRB model translation (see Mitchell 2003) for fluid-structure impact purposes than would have otherwise been possible. However, as mentioned previously, the Dytran fine-mesh SRB impact simulations typically terminate

prematurely due to unbounded deflections, which prevents further understanding of the failure mechanism at work. Fortunately, subsequent releases of the LS-Dyna preprocessor have included built-in translators for conversion of models constructed for other analysis codes, including MSC.NASTRAN. LS-Dyna has also been shown to provide for robust, generally stable analyses of impact problems with large deformations (e.g., Rust and Schweizerhof 2003), with reductions in convergence issues and abrupt terminations. This is the justification for employing LS Dyna for the purposes of numerical buckling analysis (for both the simple cylinder and SRB) in this study. Fig. 5.10 shows the mesh resolution of the original NASA-provided SRB model in the vicinity of the forward skirt loaded into the LS-Dyna user interface.

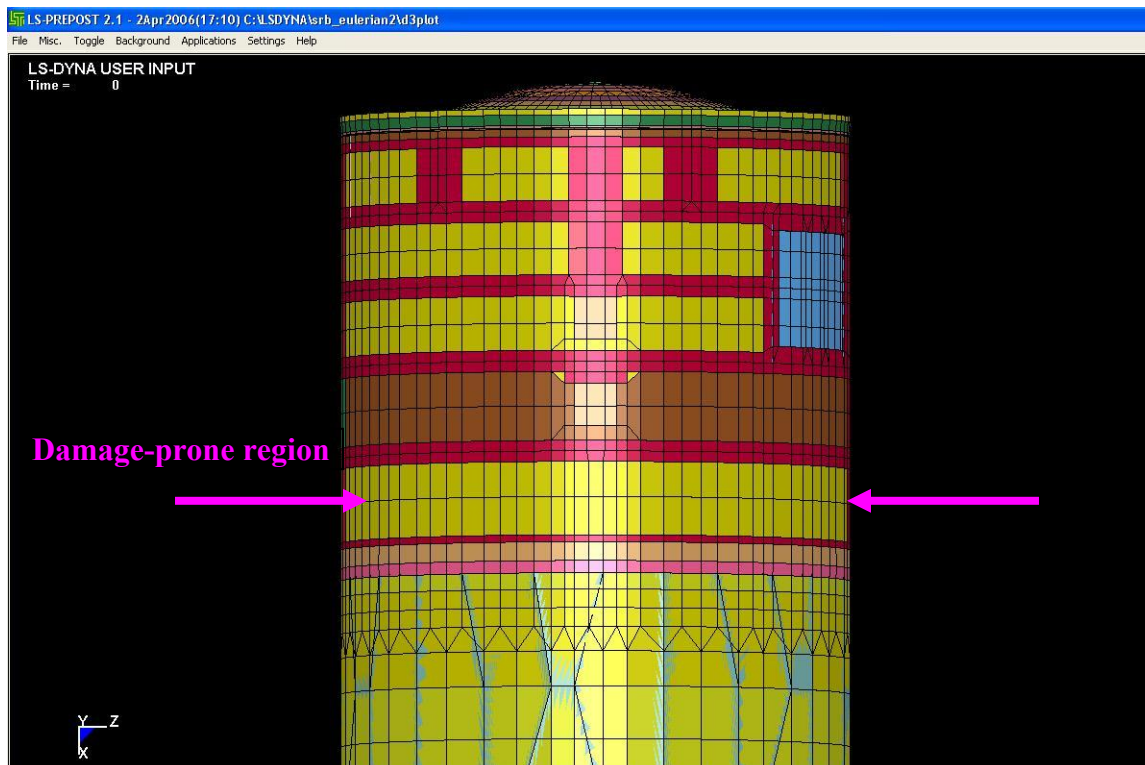


Fig. 5.10 – Original mesh of SRB forward skirt FEM

Water impact simulations conducted with both MSC.Dytran and LS-Dyna predict plastic yielding in the damage-prone region shown in the photographs in Fig. 5.9. Fig. 5.11 shows the predicted plastic strain resulting from one such simulation.

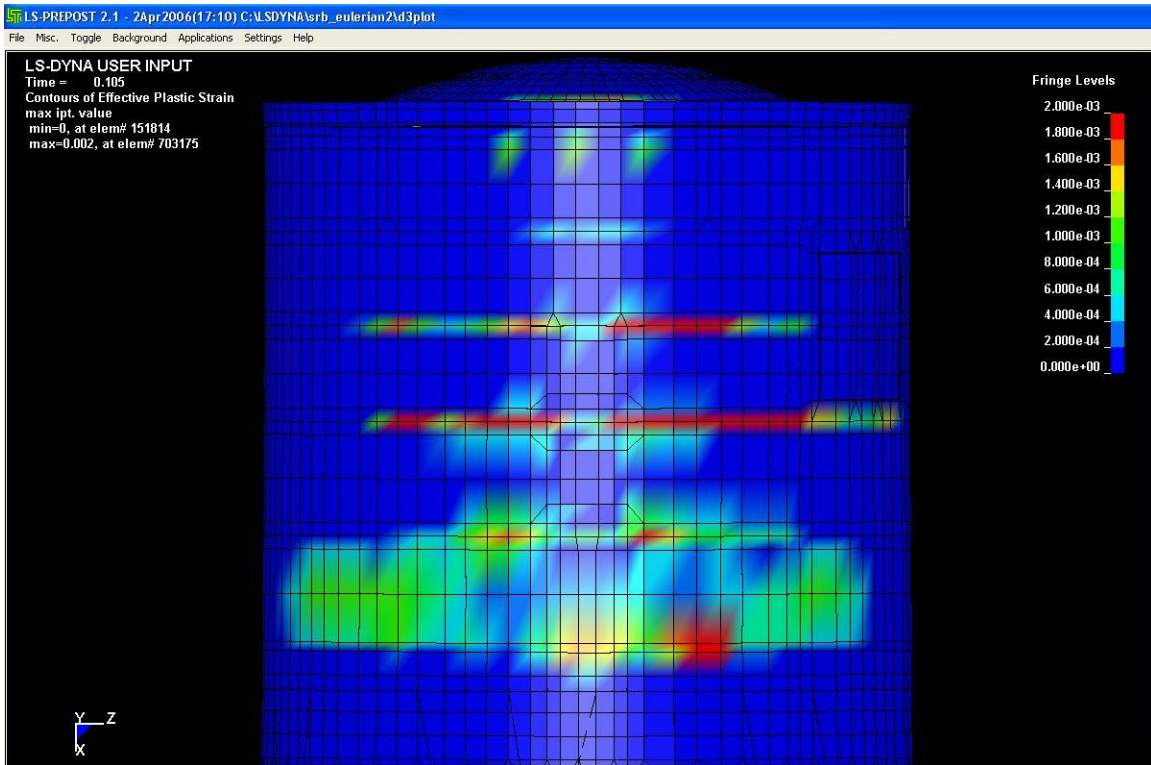


Fig. 5.11 – Plastic yielding predicted from initial splashdown modeling

Though the original mesh is sufficiently resolved to indicate stress concentrations and plastic yielding in the region where material failure has been observed, there does not appear to be sufficient resolution to capture the buckled deflection patterns. In order to confirm this, hypothetical loading conditions are applied to the forward skirt to determine whether buckled patterns such as those observed can be replicated.

The first loading case is compressive only, and the load is applied along the upper rim of the forward skirt, and is slowly increased so as to avoid any potential for dynamic buckling

mechanisms. Fig. 5.12 shows the buckled shape that results once the applied load is increased to the critical load of the forward skirt assembly.

LS-DYNA USER INPUT
Time = 0.375

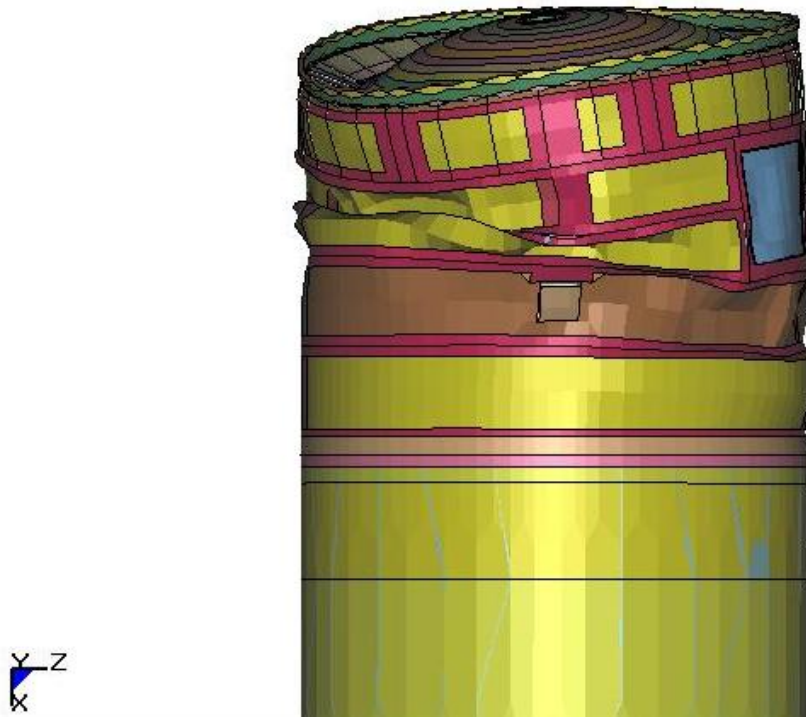


Fig. 5.12 – Buckled SRB forward skirt from compressive loading

The deformation pattern shows that using the current mesh, the LS-Dyna model does not predict buckling in the damage-prone region of the forward skirt, even at compressive loads that lead to global collapse of the forward skirt.

In the second loading scenario, a compressive force and uniform lateral pressure field are applied in a quasi-static fashion to the damage-prone section of the forward skirt. The results indicate that even under extreme loading conditions, when the circumferential stiffener just above the section experiencing damage is itself yielded, the failure pattern still does not resemble

the angled buckled patterns witnessed on recovered forward skirts. Fig. 5.13 shows a deflection pattern for one of the hypothetical loadings.

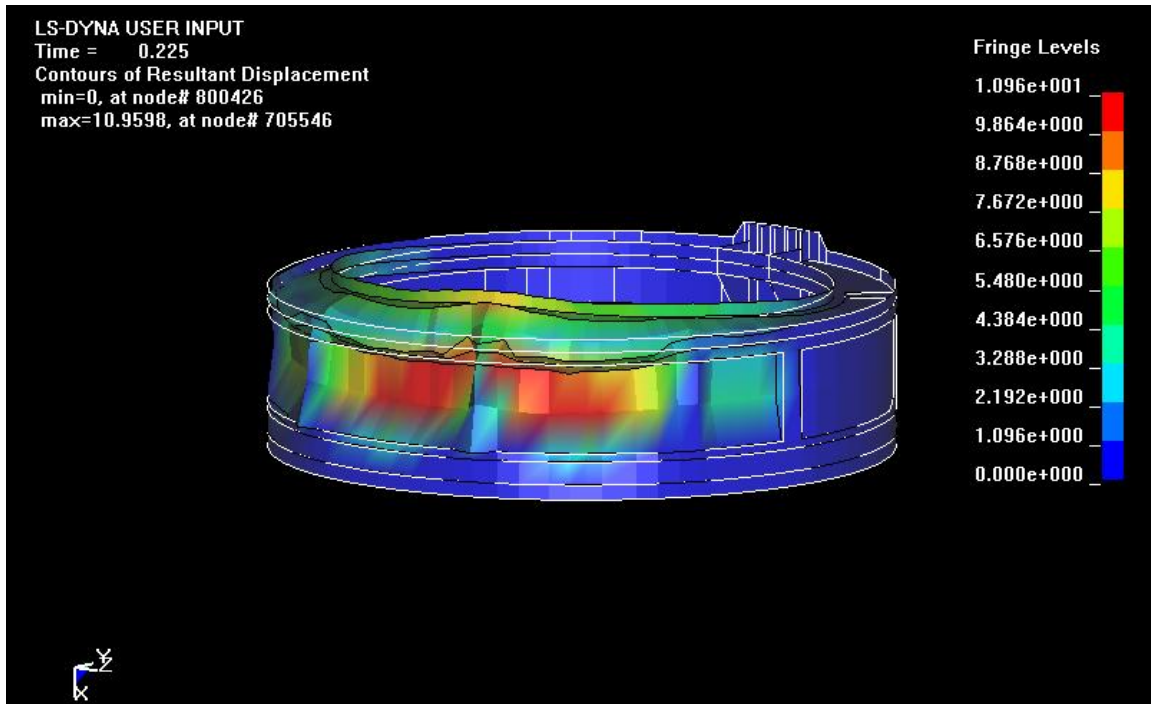


Fig. 5.13 – Hypothetical loading of original forward skirt mesh

This simple loading exercise indicates that there does not appear to be sufficient resolution in the original SRB mesh to adequately capture the buckled failure patterns. Therefore in order to more fully capture the deformation patterns observed, a re-meshing is conducted in which the plate elements in the lowest circumferential panel of the forward skirt (between the lowest circular stiffener and the bolt holes for connection to the steel motor casing) are split up into quadrilateral (and some triangular) shell elements. Fig. 5.14 shows the re-meshed forward skirt.

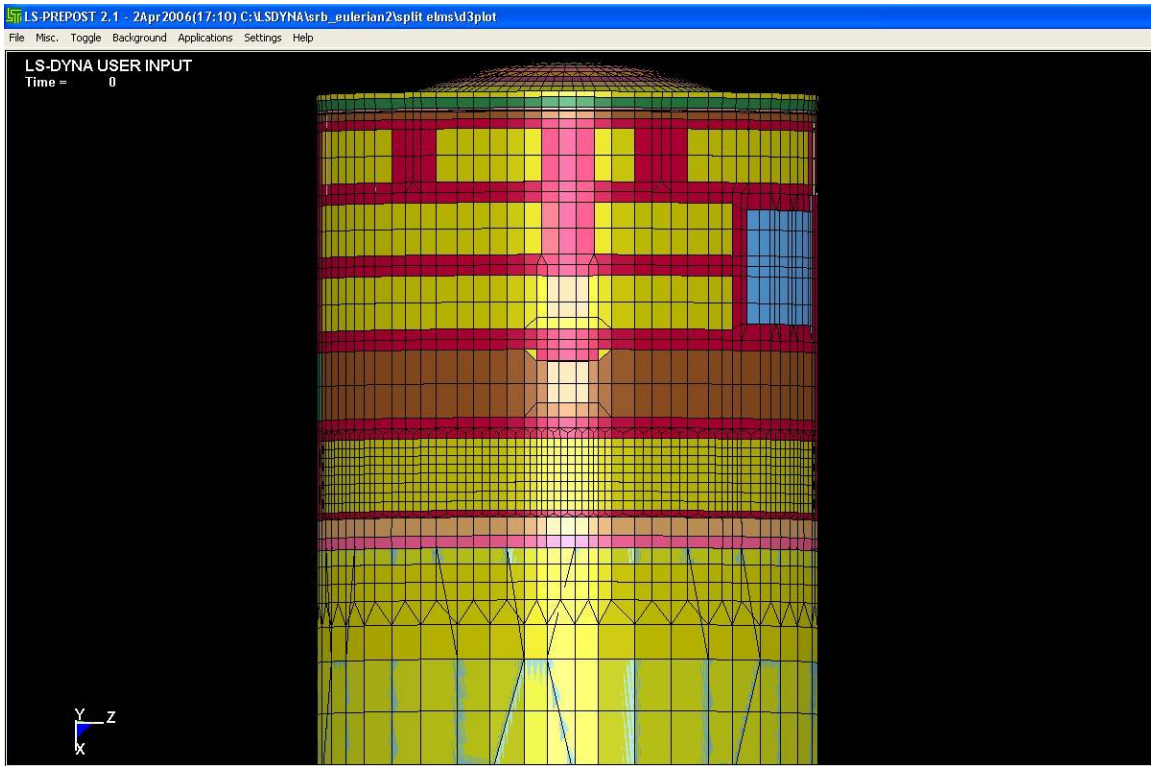


Fig. 5.14 – Re-meshed SRB forward skirt

The increased resolution in the damage-prone portion of the forward skirt allows for a more accurate prediction of the internal forces and elemental stresses during the fluid impact. The smaller element edge lengths also make it possible for the deformation patterns observed in real-world SRB damage cases to be predicted. The increased number of elements does not contribute appreciably to the overall model run times, since in total there are over 10,000 Lagrangian nodes. Additionally, the time step used by LS-Dyna is still governed by an element elsewhere in the structural model, so the remeshing of the forward skirt does not increase overall model analysis times.

The remeshed SRB model is given an initial velocity (both transverse and rotational) and impacted with an Eulerian fluid region given the material properties of water. Recall from Chapter 3 the observations concerning the relative mesh resolutions of the Lagrangian and

Eulerian domains. The model verification exercise presented shows that for transient finite element analyses using explicit time integration, the coupling algorithms used to reconcile the structural and fluid regions are sensitive to the relative resolutions. This has implications for the impact analysis of the SRB forward skirt presented here. The smaller element edge lengths in the remeshed portion of the forward skirt now require a fluid mesh that is similarly resolved in order to avoid the spurious pre-impact oscillations observed in the verification exercise (see Figs. 3.7 and 3.8). In order to avoid excessively long run times, the three-dimensional Eulerian volume is meshed such that those elements nearest the remeshed portion of the forward skirt are given comparable element edge lengths. However, as one moves away from the area of focus, the element edge lengths gradually become longer. This approach should be employed carefully, because unsuitably high aspect ratios can result for some elements if the element edge lengths are increased too quickly.

Fig. 5.15a shows the SRB model positioned with the Eulerian fluid region prior to water impact.

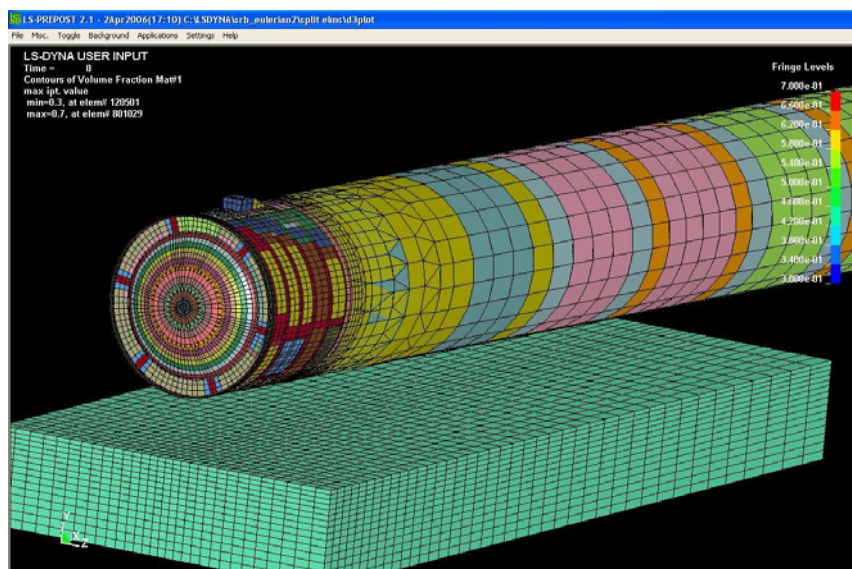


Fig. 5.15a – SRB prior to impact with the free water surface

Not shown in Fig. 5.15a are additional Eulerian elements between those shown and the SRB. These elements are initialized as being void of fluid, but water displaced by the SRB during impact is able to move into these empty volumes. Fig. 5.15b shows the model of the SRB at the instant of slapdown.

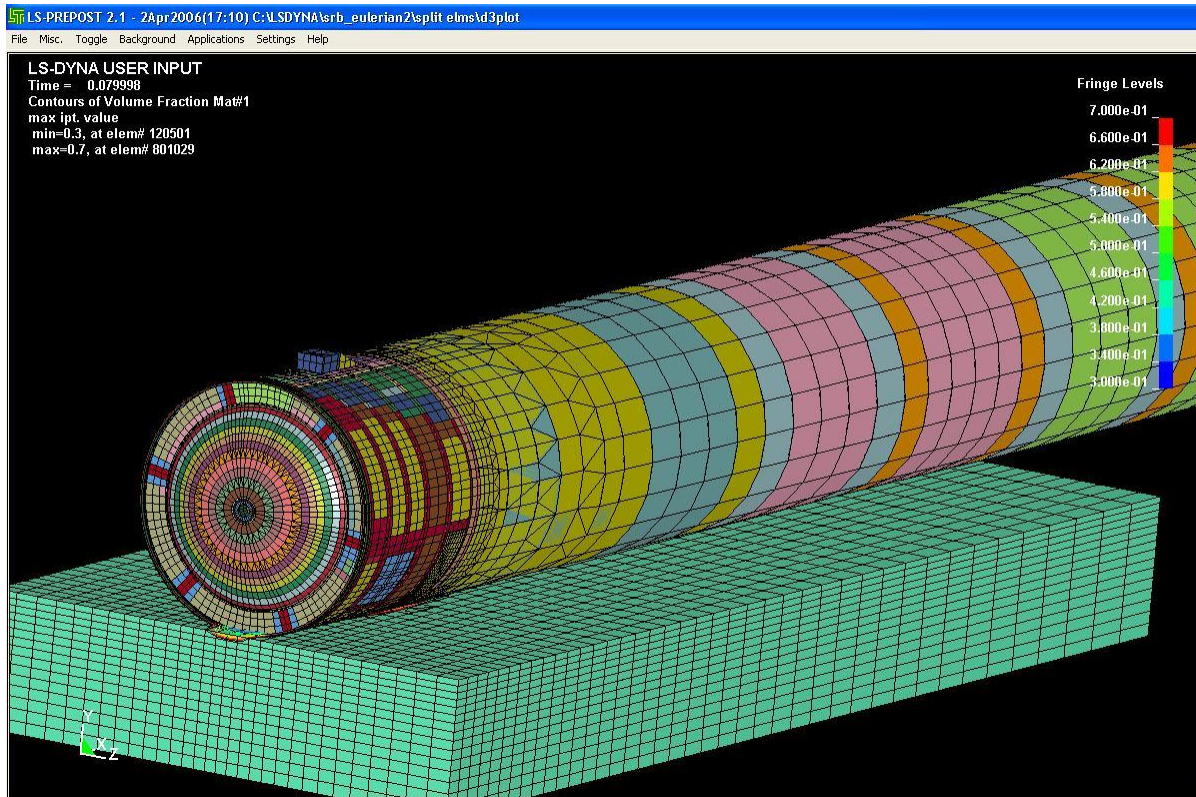


Fig. 5.15b – SRB impacting with the free water surface

Just visible at the point of contact between the forward skirt and the fluid elements are the model fringe lines indicating the boundary between water elements and void elements. These fringe lines can therefore be thought of as the free water surface. Fig. 5.15c shows the SRB model 5 milliseconds after the initial impact.

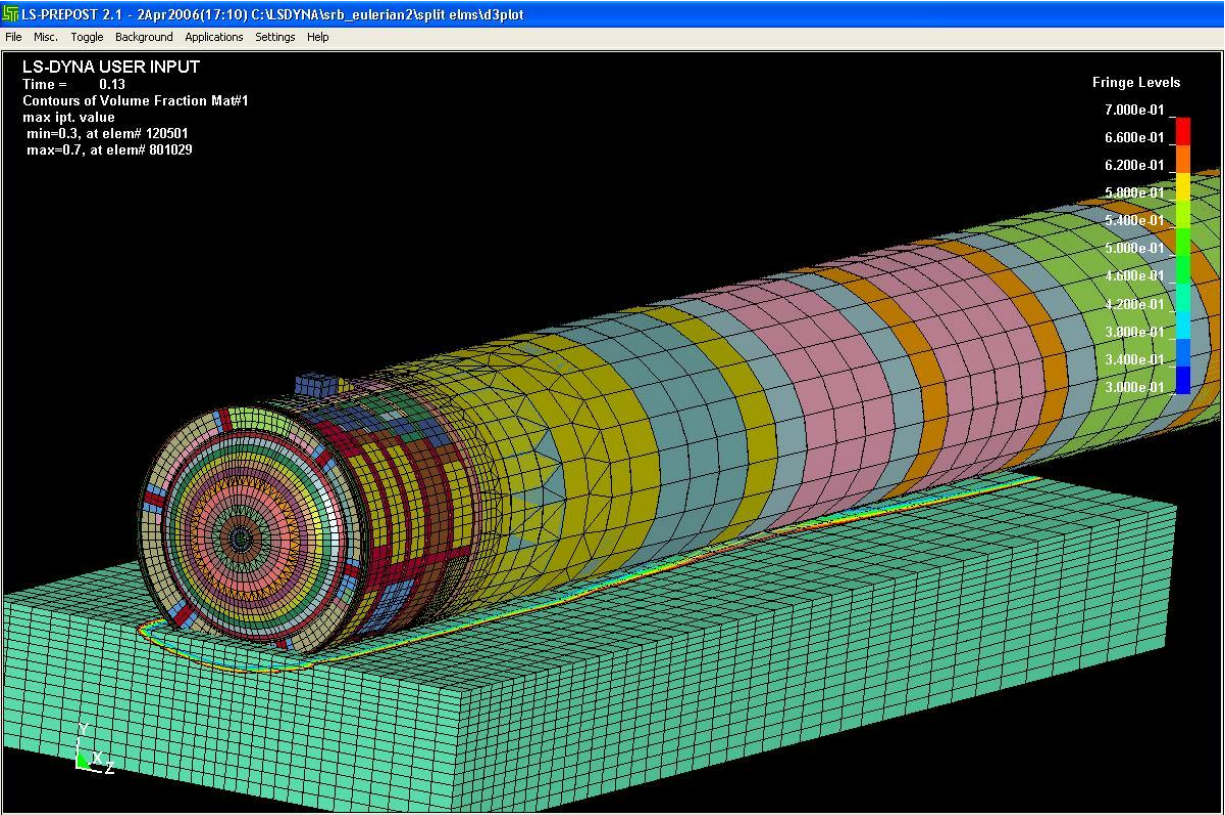


Fig. 5.15c – Contours showing free water surface profile as result of SRB impact

The fringe lines are seen moving out from the body of the SRB, indicating that water is being displaced. Stresses and deformations occurring within the Lagrangian structural model are extracted through the LS-Dyna post-processor. The plastic yielding predicted by the impact simulations with the remeshed forward skirt show displacement patterns in general agreement with those observed in SRB damage cases. Fig. 5.16 shows the diagonal bands of plastic yielding resulting from an LS-Dyna simulation for one particular impact scenario.

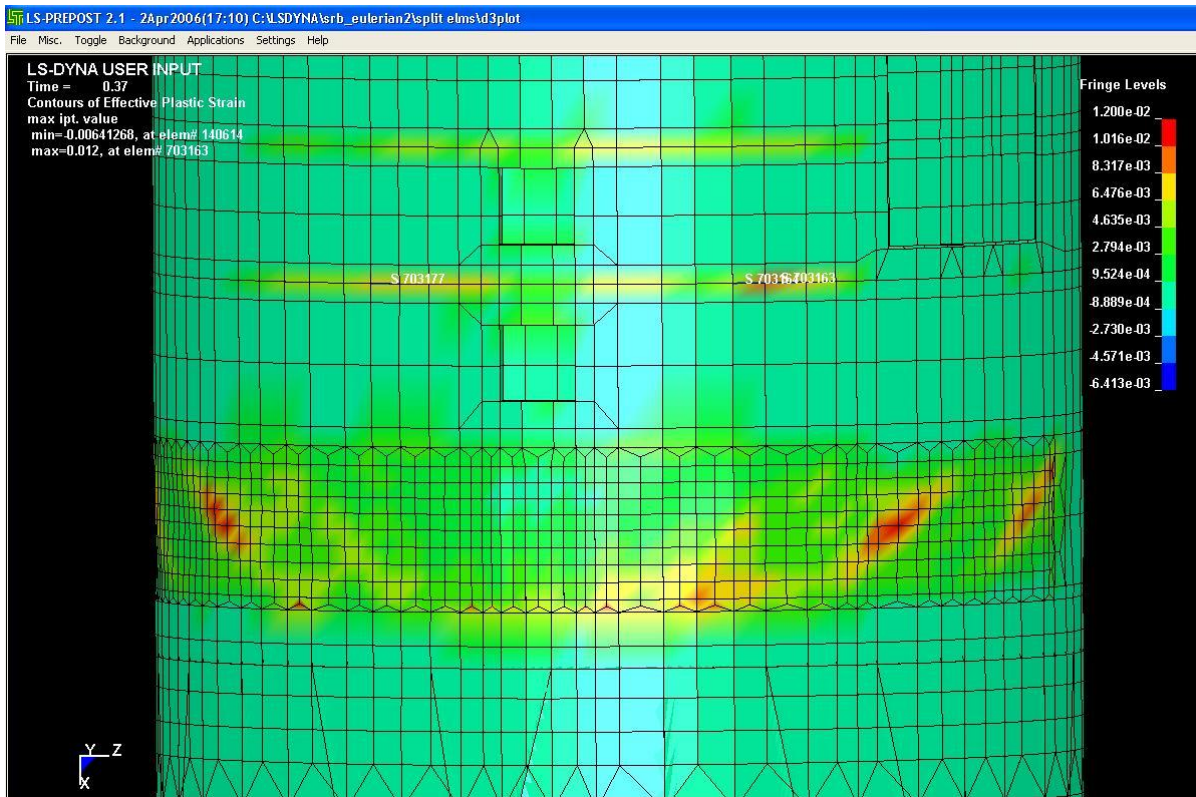


Fig. 5.16 – Diagonal plastic yielding bands in SRB forward skirt

Note that these results are obtained simply as a result of the water impact simulation, and no additional loadings are applied to the structure. The resulting failure patterns are generated as a result of water impact loads only. Fig. 5.17 shows the lateral deflection of the nodes in the lower segment of the forward skirt corresponding to the observed buckle patterns seen in Fig. 5.18. Note that in Fig. 5.17, the color contours indicate displacement in the YZ plane. The upper and lower bound of the color legend have been adjusted to highlight the displacement pattern within the forward skirt. Without this adjustment the plastic deformation would be drowned out by the rigid-body displacement (approximately 93") of the entire SRB during the impact simulation. The predicted deformation patterns in the forward skirt clearly show the same orientation and as those seen in Fig. 5.18.

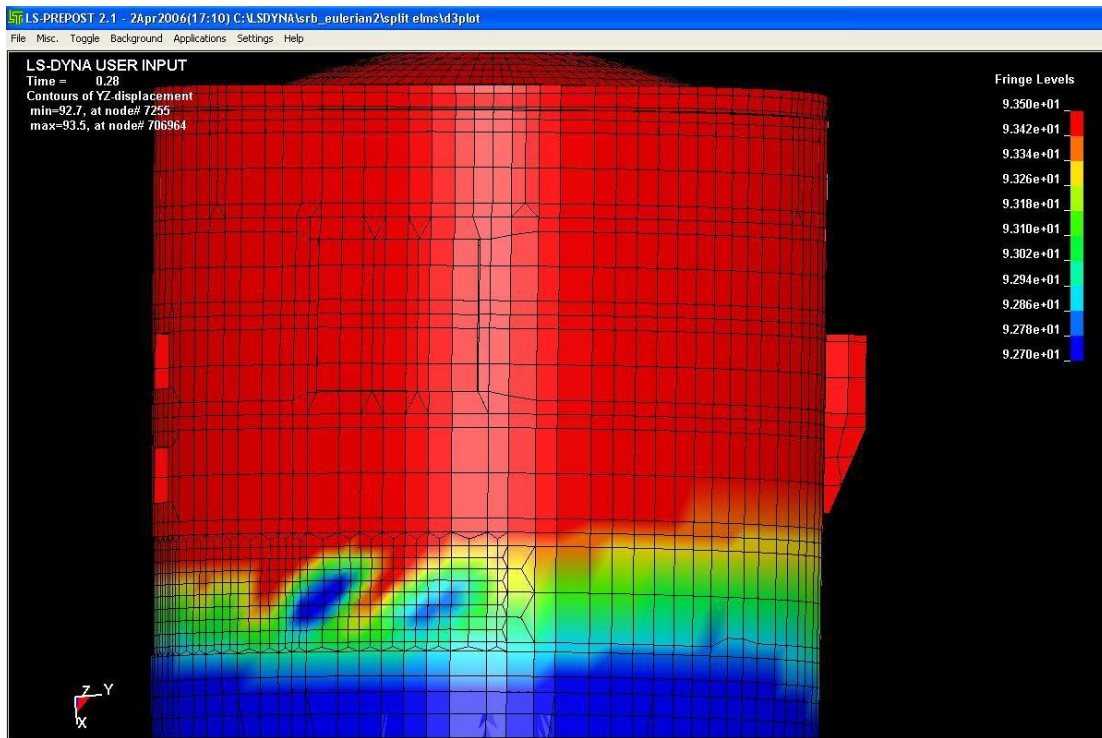


Fig. 5.17 – Relative lateral displacement of nodes in forward skirt

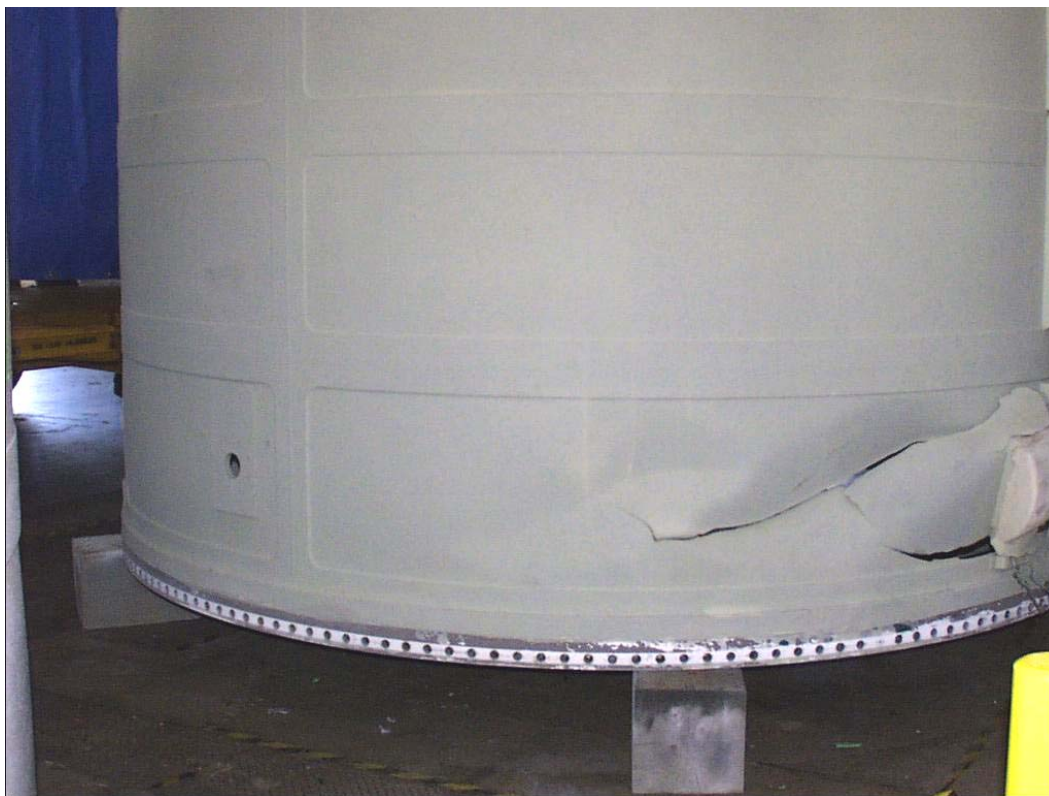


Fig. 5.18 – Buckled patterns on SRB forward skirt

The qualitative results of the remeshed forward skirt impact simulations appear to show damage patterns in agreement with those observed on actual shuttle missions.

The next step is to evaluate the structural response of the yielded elements during the splashdown sequence to determine whether the failure mechanism can be characterized as buckling according to the von Karman plate and Donnell cylinder stability equations. Since these conditions are time-independent, for analysis of the transient forward skirt problem, the stability criteria need to be modified to account for inertial effects and transient pressures. Similar approaches have been conducted in other studies involving impact-induced buckling. The transverse motion of a thin cylindrical shell subjected to axisymmetric loading and deformation is given by (Wei et al. 2005):

$$\frac{\partial^2 M_x}{\partial x^2} + N_x \frac{\partial^2 w}{\partial x^2} + \frac{N_\theta}{R} = \rho h \frac{\partial^2 w}{\partial t^2} \quad (5.12)$$

Recognizing that the term on the right hand side of Eq. 5.11 is the inertial force per unit area, and recalling the transverse (i.e., normal to the plate) von Karman equilibrium condition, additional terms are added to Eq. 5.7c account for inertial effects and the time-dependent pressure loading resulting from water impact:

$$D \left(\frac{\partial^4 w}{\partial x^4} + 2 \frac{\partial^4 w}{\partial x^2 \partial y^2} + \frac{\partial^4 w}{\partial y^4} \right) - N_x \frac{\partial^2 w}{\partial x^2} - N_y \frac{\partial^2 w}{\partial y^2} - 2N_{xy} \frac{\partial^2 w}{\partial x \partial y} = p(t) + \rho h \frac{\partial^2 w}{\partial t^2} \quad (5.13)$$

Eq. 5.13 can be monitored using finite differencing of adjacent elements in the SRB forward skirt as a time-dependent indicator of buckling. This is done using an array of elements that experience yielding in the damage-prone segment of the forward skirt and evaluating the partial derivatives with the same finite-differencing type approach described previously for the simple cylinder exercise. The evaluation is performed for an instance of damage predicted by the

LS-Dyna model, and also for an instance where no damage is predicted. Fig. 5.19 shows Eq. 5.13 evaluated in time during the respective impact sequences.

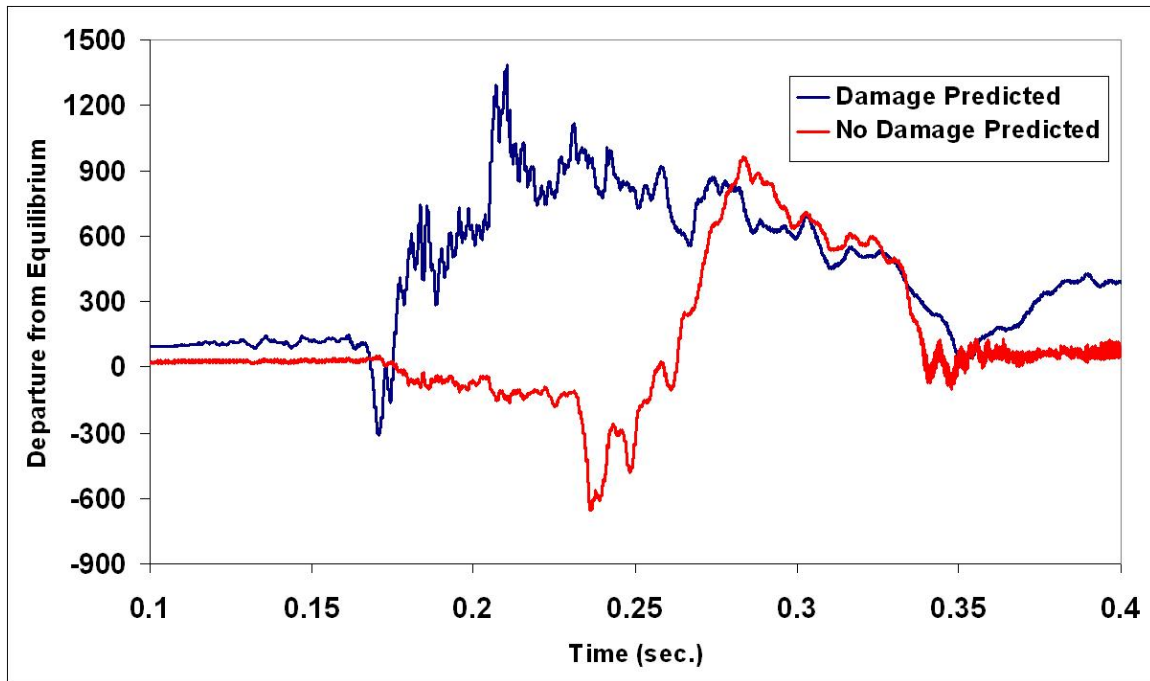


Fig. 5.19 – Time-dependent von Karman equilibrium condition evaluated for damage and no-damage impact sequences

The instance in which damage is predicted is given a higher initial velocity, and therefore impact occurs prior to the case where no damage is predicted. It is interesting to note that the initial departure from equilibrium as a result of impact for both curves is of roughly the same magnitude and duration. In the no-damage case, the equilibrium condition eventually is restored at close to zero, while this is not the case for the forward skirt that experiences damage. This indicates that the time-dependent von Karman plate equilibrium condition offered by Eq. 5.13 does offer one means for classifying damage predicted by the LS-Dyna model as buckling.

5.4.3 SRB Risk Assessment

With the re-meshed FE model of the SRB forward skirt predicting deformation patterns consistent with the observed damage cases, an improved limit state can be defined for the purposes of structural risk assessment. Recall that previous SRB risk predictions (Mitchell 2003; Mitchell and Mahadevan 2004) were not in agreement with the observed frequency of damage, due in part to uncertainty concerning the failure definition. The numerical buckling study of the SRB forward skirt just presented shows that the von Mises stress predictions from the re-meshed model offer a suitable (i.e. consistent with observed damage patterns) indicator of damage to the SRB. The nonlinear LS-Dyna code tracks small rotational displacements within the structure, and will therefore predict damage resulting from buckling failure mechanisms.

In this section the re-meshed SRB model is used to update the risk assessment prediction for the forward skirt as a result of splashdown. The impact sequence shown in Figs. 5.15a-c is simulated for varying initial velocities of the SRB. The von Mises stresses in the forward skirt as well as deflection patterns are monitored in order to determine whether the buckling damage has occurred. Based on this numerical analysis, the critical impact velocity for the onset of damage is found to be 420 in/sec. The impact simulations are conducted with several different portions of the SRB serving as the leading edge, so as to better understand the role of axial orientation in the observed damage. It is found that when the reinforced portion of the SRB serves as leading edge, damage does not occur within that portion of the forward skirt, even for impact velocities in excess of the 420 in/sec limit for the non-reinforced portions of the SRB. In general, this supports the results of the simple drop tests performed previously (Mitchell and Mahadevan 2004) with MSC.Dytran, though the less-resolved model resulted in lower critical impact velocities.

At this stage some discussion is in order concerning the statistics that have been used previously for the initial horizontal and vertical impact velocities of the SRB. Figures provided by NASA have indicated that the SRB strikes the ocean surface with a vertical velocity of 75 fps, and with a horizontal velocity equal to the surface wind speed at the time of splashdown. The average surface wind speed as recorded by NASA following space shuttle launches is 23.0 fps, and with a standard deviation of 11.2 fps. To confirm these figures, historical buoy data were obtained from the National Oceanic and Atmospheric Administration for Station 41010, which is deployed roughly 130 miles east-northeast of the shuttle launch sites at Cape Canaveral and is funded by NASA for the purpose of monitoring sea state conditions in the SRB recovery zone. The buoy data show a lognormal distribution for the surface wind speed, with a mean of 20.3 fps and a standard deviation of 10.1 fps. Recall that the instances of forward skirt damage are correlated with high surface wind velocity; however, there has been no confirmation regarding the assumption that the SRB horizontal velocity at initial impact is actually equal to the surface wind velocity.

For the purposes of a revised risk assessment based upon the refined critical forward skirt impact velocity of 420 in/sec (35 fps), the initial vertical impact velocity is assumed to be normally distributed with a mean of 900 in/sec (75 fps) and a standard deviation of 24 in/sec (2.0 fps). Along with the statistics derived from the NOAA buoy data for horizontal velocity, and the forward skirt impact velocities predicted by the rigid-body Dytran model described in Chapter 2, a Monte Carlo simulation is conducted to obtain a revised risk assessment for the SRB forward skirt. To account for the reinforced portion of the SRB forward skirt, it is assumed that failure does not occur when that section (occupying 25% of the total SRB circumference) serves as the leading edge. Given no prior information concerning the axial orientation of the SRB at

splashdown, it is assumed that all portions have an equal likelihood of being the leading edge at impact. Finally, the yield stress of the 2219 aluminum comprising the forward skirt is assumed to follow a lognormal distribution. The mean value is taken as the nominal yield stress for the alloy, 57.3 ksi, and a coefficient of variance of 10% is assumed.

The results of the Monte Carlo simulation give a probability of failure p_f for the SRB forward skirt of 0.095. This result is much closer to the observed failure rate (recall, 4 failures out of 108 splashdowns) than previous estimates, though it is still somewhat higher than what is expected given the frequency of observed damage cases. The failure probability is found to be most sensitive to the assumption for horizontal velocity, and this raises again the issue discussed earlier concerning the correlation between surface wind speed and the actual horizontal velocity of the SRB at splashdown. The three main parachutes are only fully deployed at an altitude of roughly 5,500 ft, leaving less than one minute for the assembly to be affected by winds in the vicinity. However, it also seems apparent that high surface wind speeds do play a significant role in the occurrence of damage (McFadden 1999). Given this uncertainty, it seems reasonable to raise the possibility that the horizontal velocity of the SRB at splashdown may not actually achieve the same magnitude as the surface wind speeds. Table 5.1 shows the results of additional Monte Carlo simulations conducted with reduced mean values for the horizontal velocity. It can be seen that the predicted p_f moves into the range of expected values (based on observed failures) as the mean value for the horizontal velocity of the SRB is reduced. Sensitivity is also observed for the vertical velocity, though the trend is not as pronounced as that shown in Table 5.1.

Table 5.1 – Sensitivity of SRB p_f to horizontal velocity at splashdown

Percent of Mean Surface Wind Speed (20.3 fps)	p_f
100%	0.095
90%	0.073
80%	0.058
70%	0.045

Only the single nominal value for vertical velocity at impact of 900 in/sec has ever been noted, and no information has been found to confirm this value or to quantify the statistical distribution for this quantity.

In spite of the significant informational uncertainty concerning the horizontal and vertical impact velocities, the finite element-based risk predictions presented here are in reasonable proximity to the observed failure rate, indicating that the FEM approach to SRB splashdown shows promise for further studies. However, there are several additional sources of uncertainty concerning the splashdown conditions that also need to be resolved to improve the risk predictions. These include effects from wave conditions on the ocean surface at the time of splashdown (correlated with high surface wind speeds), as well as loads applied to the forward skirt from the parachute chords during the initial impact and rollover phases. It should be stated that the risk estimates made in this study are the result of academic investigations into SRB splashdown and modeling of fluid-structure impact problems. Therefore the risk assessments should not be interpreted as design guidance or as authoritative conclusions concerning the SRB splashdown damage scenarios.

5.5 Summary and Conclusions

This numerical investigation of the failure mechanism leading to the observed forward skirt damage reinforces the theory that water impact loads resulting from slapdown cause the observed damage. The nonlinear LS-Dyna finite element software is shown to predict similar deformation patterns to those observed in the lower segment of the damaged forward skirts. The exercise with the simple cylinder loaded to failure in a quasi-static buckling test demonstrates the nonlinear capabilities of LS-Dyna. Therefore, geometric nonlinearities of the kind that result in elastic buckling are captured by the software. However, it is a separate question as to whether the observed damage to the forward skirts is a result of elastic buckling. Review of the derivations for classical plate and cylinder stability conditions provide a theoretical framework for whether or not to label a particular instance of permanent deformation as buckling. The stability conditions are evaluated over the course of the simulated impact event using a finite differencing type approach in order to determine the true nature of the SRB forward skirt damage.

For the purposes of risk assessment, it has been shown that monitoring of the von Mises yield criteria in the forward skirt elements is sufficient for determination of the limit state for *damage*. However, use of the term *buckling* implies a particular type of damage, usually resulting from geometric instabilities within the structure. In the case of the SRB splashdown problem, there have been no instances of forward skirt damage that appear to result from a separate failure mechanism. All instance of damage have been confined to the same region of the forward skirt, and all deformation patterns have been of the same general form. Therefore monitoring of the von Mises yield condition is found to be a suitable limit state for risk

assessment of the SRB forward skirt, provided it is used along with nonlinear FE analysis and a model that is sufficiently resolved to capture the buckling mechanism.

The revised risk estimate for the SRB forward skirt based on the updated critical impact velocity of 420 in/sec. is in closer agreement with the observed frequency of damage than prior estimates. However, the informational uncertainty concerning the statistical distribution parameters of the horizontal and vertical velocities of the SRB at initial impact presents a challenge for further refinement. Without improved statistical representations of these quantities, as well as additional information concerning the contribution of surface waves and parachute loads, then it is unknown whether the differences in the predicted failure rate and that observed are due to modeling error or simply incorrect assumptions concerning the random variables. Future work should focus on ways of obtaining additional information on the horizontal and vertical velocities of the SRB at splashdown so as to improve upon these assumptions.

CHAPTER VI

VALIDATION INFERENCE EXTRAPOLATION TO SRB PROBLEM

6.1 Background and Overview

The research described heretofore is motivated in large part by the real-world fluid-structure impact problem involving the SRB forward skirt. However, it is clear that any conclusions pertaining to the SRB issue based upon the experimental procedure and model validation outlined in Chapter 4 must be made through extrapolation. Often in engineering design decisions must be made based on information that is not available from the measurements at hand. For example, a model may be validated for a specific output quantity such as stress within a structural member, but the decision to be made may be based upon an acceleration criterion. The question then becomes whether or not validation inferences can be made concerning acceleration levels in the actual system based upon stresses predicted by the model. Also, it is often the case that a model has been validated and a design tested for a set of input conditions, when the actual real-world system is constructed somewhat differently, or is subjected to loadings outside of the tested domain. Within the engineering community, extrapolation is generally considered a practice to be conducted with extreme caution or avoided whenever possible, since many high-profile engineering failures such as the Space Shuttle Challenger explosion (Rogers Commission 1986) and the Tacoma Narrows Bridge collapse (Billah and Scanlan 1991) are perceived to have resulted at least in part from some form of extrapolation by system designers and engineers.

Given that some degree of extrapolation is often unavoidable in practical engineering problems, researchers have focused on methods for making inferences based upon extrapolation of model predictions for system designs and loading conditions for which test data is unavailable. This can be done with some measure of confidence provided a linking function can be found which connects the variables or application regions for which a decision needs to be made to the validated system model (Hills and Leslie 2003). If no such linking function can be obtained, one alternative approach that has been proposed (Hills and Trucano 2001) uses first-order sensitivity factors to relate the validated and target variables or domains.

It should be noted that much of the research pertaining to comprehensive and robust methods for inference extrapolation is fairly recent and the body of literature related to it is not extensive. Several studies by Oberkampf and Trucano (2002), the U.S. Department of Defense (DMSO 1996), and Thacker and Huyse (2002) have emphasized the need for a body of research related to model extrapolation issues. This is not to say that the concept of extrapolation is new to engineering and scientific fields. Indeed, extrapolation approaches are used in many fields for a variety of applications. Spatial extrapolation is often conducted within geographic information system (e.g., Gilmanov et al. 2005; Miller et al. 2004) applications and studies. Also, temporal extrapolation techniques are used by planners in many fields, such as in medicine and public health (Pickle et al. 2007), land use forecasting (Peeters et al. 2008), and financial management (Ooi et al. 2007). In recent years, the increased focus upon the issue of long-term anthropogenic climate change has seen many applications of various extrapolation methodologies for planning scenarios using observed climatic trends (see for example, Bates et al. 2008; NRC 1987).

In this chapter, a conceptual framework using Bayesian networks will be proposed for quantifying the confidence in inferences extended from the validation exercise conducted in

Chapter 4 to the SRB forward skirt problem. The basis for this proposed methodology is work recently conducted by Rebba (2005) and Mahadevan and Rebba (2005). Following a brief introduction to the concept of Bayesian networks, application to experimental work such as that with the thin-walled cylinder presented previously will be proposed. The framework is first established for inferences extended to unmeasured quantities, such as accelerations in the cylinder wall and stresses at locations without strain gages. The potential for this methodology to be applied to the real-world SRB problem is then explored.

6.2 Bayesian Network Methodology

The proposed method involves the use of Bayesian networks to quantify the confidence in inferences extrapolated from the validated model domain to the application domain. In this context, it is helpful to include some background on Bayesian probability theory. The fundamental point to be made is that Bayesian probability represents one's *degree of belief* concerning the value of a quantity, while frequentist probability represents a physical characteristic concerning the likelihood of occurrence of some real-world quantity (Lindley 1965). Note that the frequentist probability can only be determined accurately from repeated trials, whereas the Bayesian probability can incorporate prior knowledge and can be updated as new data (i.e., observed failures and non-failures) becomes available. Therefore, the use of Bayesian probability has gained popularity for real-world instances where experimental or field data is scarce. There are many sources available for more in-depth discussion of Bayes' theorem and Bayesian updating. The reader is referred to these references (e.g., Ang and Tang 1984; Press 1989; Haldar and Mahadevan 2000) for a more thorough introduction to the topic.

The concept behind learning with Bayesian updating comes from applying Bayes' theorem (Eq. 4.17) to situations where prior belief in the value of some system parameter is updated according to newly-acquired data. Rebba (2005) explores a Bayesian framework for several confidence extrapolation scenarios within a model validation context; in this chapter, we investigate the applicability of this methodology to small-scale experimental testing such as that described in Chapter 4. Suppose one is dealing with a computational probabilistic model $y(\mathbf{x}, \boldsymbol{\alpha})$ but must make a decision concerning a separate variable $h(\mathbf{x}, \boldsymbol{\alpha})$. Both the model output and decision variable are functions of an input vector of random variables $\boldsymbol{\alpha}$, while \mathbf{x} represents a vector of spatial or temporal coordinates. A validation experiment is performed producing a vector of data \mathbf{z} . The joint probability distribution as well as the individual marginal densities of each of the input parameters comprising the vector $\boldsymbol{\alpha}$ can then be updated using the Bayesian methodology:

$$f_{\alpha}(\boldsymbol{\alpha} | \mathbf{z}) = \frac{f_{\alpha}(\boldsymbol{\alpha})f(\mathbf{z} | y(\mathbf{x}, \boldsymbol{\alpha}))}{\int f_{\alpha}(\boldsymbol{\alpha})f(\mathbf{z} | y(\mathbf{x}, \boldsymbol{\alpha}))d\boldsymbol{\alpha}} \quad (6.1)$$

where the prior joint density function of the vector $\boldsymbol{\alpha}$ is given by $f_{\alpha}(\boldsymbol{\alpha})$ and the likelihood function for the observed data \mathbf{z} is given by $f(\mathbf{z} | y(\mathbf{x}, \boldsymbol{\alpha}))$. The joint distribution for the decision variable h can then be estimated by generating sample input parameters using the newly-obtained posterior density function $f_{\alpha}(\boldsymbol{\alpha} | \mathbf{z})$ from Eq. 6.1 and then substituting them into $h(\boldsymbol{\alpha} | \mathbf{z})$. The integrations required to solve Eq. 6.1 can be conducted using Markov Chain Monte Carlo (MCMC) techniques (Gilkes et al. 1996). Finally, the confidence of the inferences concerning h can be assessed by comparing the prior and posterior densities of h within the application domain $\boldsymbol{\alpha}$. This step is similar to the calculation of Bayes factor given by Eq. 4.18.

The preceding discussion serves as an introduction to the concept of Bayesian networks (BNs), graphical illustrations showing the conditional dependencies of various random variables or events within a system of interest. The graphs are represented by a series of nodes connected by unidirectional arrows, with each node representing a different variable in the problem. Each node is labeled either a parent or child relative to other nodes depending upon the direction of the arrow connecting it to each node; parent nodes “point” to child nodes. A node cannot be both a parent and child to the same node, and BNs are directed acyclic graphs (DAGs), meaning one cannot follow the direction of parent-child arrows from a node through the network and back to that same node. Examples of introductory texts on the subject of Bayesian networks include Jensen (1996) and Heckerman (1996). The corresponding Bayesian network for the example problem presented above is shown in Fig 6.1.

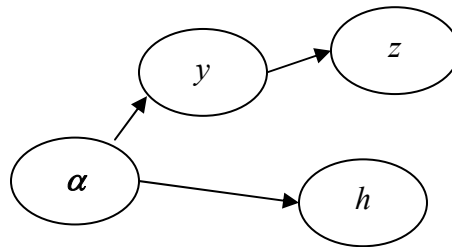


Fig. 6.1 – Sample Bayesian network

If one denotes each variable (node) in the system as X_i , and the parent(s) of that variable as pa_i , then the joint probability distribution of the entire network is given by:

$$p(x) = \prod_{i=1}^n p(x_i | pa_i) \quad (6.2)$$

If we denote the entire Bayesian network shown in Fig. 6.1 as U , then the joint density function according to Eq. 6.2 is given by:

$$f(U) = f(\alpha) \times f(y|\alpha) \times f(h|\alpha) \times f(z|y) \quad (6.3)$$

Newly acquired information concerning a variable can be added as an additional node and the probabilities of all the other nodes in the network can be updated. For example, suppose further analysis reveals an additional set of random variables β upon which the decision variable h is dependent. The original Bayesian network shown in Fig. 6.1 is now represented by:

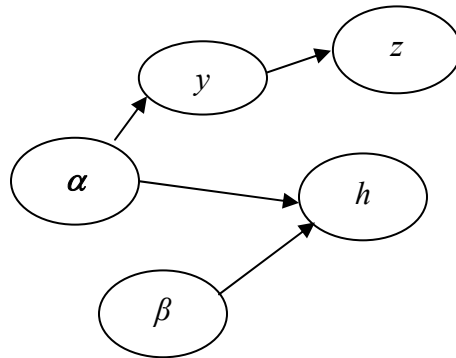


Fig. 6.2 – Updated Bayesian network with additional node

The joint density function for the entire network U is now given by:

$$f(U) = f(\alpha) \times f(y|\alpha) \times f(h|\alpha,\beta) \times f(z|y) \quad (6.4)$$

More discussion on Bayesian networks is available in recent publications (e.g., Mahadevan et al. 2001; Jensen 1996).

6.3 Confidence Extrapolation for Experimental Cylinder and SRB Problem

The research described in previous chapters is motivated by the original problem involving the SRB damage sustained during impact with the ocean surface. In keeping with that motivation, in this section we discuss potential methods for inferences gained in the experimental procedure described in Chapter 4 to be extended into problem domains for which experimental and/or field

data is not available. The concept will be introduced in stages, with several implementations of Bayesian networks described involving the experimental cylinder described before the methodology is explored for the SRB problem.

6.3.1 Experimental Cylinder: Measured Quantity to Unmeasured Quantity

In this section we discuss a scenario often encountered in engineering design: the only available experimental data does not apply directly to the decision variable. Using data collected in the experimental cylinder work previously described, an example is presented of how one might use Bayesian networks and test data concerning peak stress responses to quantify confidence in the model prediction for a separate, unmeasured structural response quantity. The LS-Dyna code used to model the experimental cylinder allows for output of many physical quantities in addition to the peak stress predictions used for the validation exercises in Chapter 4. In Chapter 3 several of these quantities are discussed in the context of mesh refinement for fluid-structure impact problems.

To demonstrate the concept, we will use the predicted time to peak stress $t_{max}(\mathbf{x}, \boldsymbol{\alpha})$ from the LS-Dyna code as the target variable for which additional insight is desired. Note that the vector \mathbf{x} represents spatial coordinates, while $\boldsymbol{\alpha}$ is a vector of random input conditions, in this case, impact velocity V_{imp} and distance h of the center of rotation above the free water surface. The location on the cylinder to be examined is on the leading edge, 6" from the top end cap (labeled Sta6_CL in Fig. 4.4). The vector of observed peak stress data at this location \mathbf{D} is used to update the distribution of $\sigma_{max}(\mathbf{x}, \boldsymbol{\alpha})$, and in turn h and V_{imp} . The posterior distributions of the input variables can then be used to update the density of t_{max} . The Bayesian network for this approach is given in Fig. 6.3.

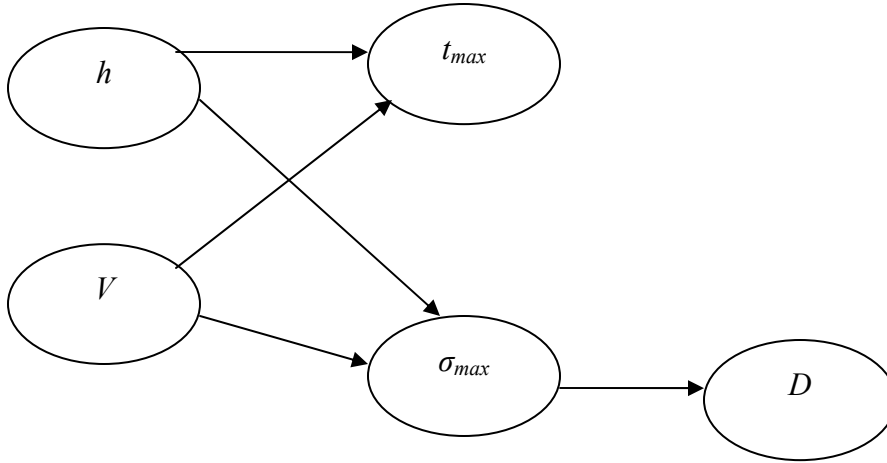


Fig. 6.3 – Bayesian network for quantifying confidence for unmeasured quantity, t_{max}

The expression for the density function corresponding to this Bayesian network is:

$$f(U, D) = f(V) \times f(h) \times f(\sigma_{max}|V_{imp}, h) \times f(t_{max}|V_{imp}, h) \times f(D|\sigma_{max}) \quad (6.5)$$

Due to long computational run times for the LS-Dyna cylinder model, surrogate models are needed to approximate $\sigma_{max}(\mathbf{x}, \boldsymbol{\alpha})$ and $t_{max}(\mathbf{x}, \boldsymbol{\alpha})$. Using the same battery of LS-Dyna runs conducted in the validation exercise in Chapter 4 along with the joint-normality assumption for the prior distributions of V_{imp} and h , the Bayesian network approach for confidence extrapolation to an unmeasured quantity can be demonstrated. The LS-Dyna results for the corresponding location on the cylinder (element 220) are used to construct a parametric response surface relating V_{imp} and h to the predicted peak stress, σ_{max} . Likewise, a second response surface is constructed using LS-Dyna predictions to approximate the time to peak stress, t_{max} at the location of interest. Note that in demonstrating this methodology, we are starting with the assumption that the predictive model has already been judged valid for the quantity of interest within the tested domain. That is, the null hypothesis has been accepted with some suitable degree of

confidence. Therefore observations of the system response can be used, through Bayes' theorem, to update the prior density functions of the random input parameters. The proposed methodology compares the resulting posterior density function of the model prediction for the unmeasured quantity (here, t_{max}) to the prior density of the same quantity in order to determine the confidence in the predictive model for the unmeasured (and therefore un-validated) quantity. The vector of observational peak stress data is taken from the cylinder drop test example presented in Chapter 4, and is measured at the location on the leading edge labeled Sta6_CL: $\mathbf{D} = \{9143.8, 8589.6, 8163.0, 9021.1, 9271.2, 8856.1, 9269.8, 7587.7, 8393.4, 8378.9\}$, with units in psi.

The inference network, response functions, and observed data are entered into the Bayesian framework using the WinBUGS[®] software. Fig. 6.5 shows the BN created using WinBUGS.

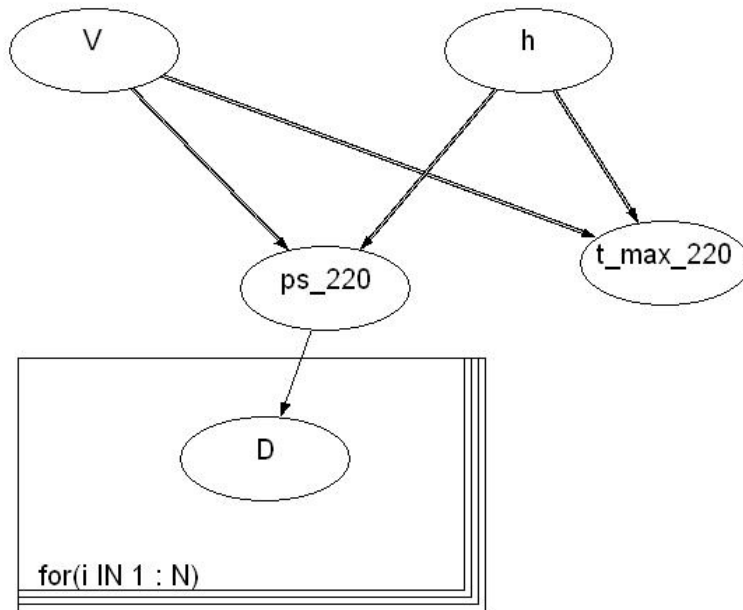


Fig. 6.4 – BN created with WinBUGS software

Note that the bold arrows indicate a functional relationship, while the thin arrow indicates a stochastic relationship. WinBUGS uses a Markov chain Monte Carlo (MCMC) technique to conduct the numerical integrations and update the prior densities on the random variables using the observed data. Table 6.1 summarizes the results.

Table 6.1 – Results of BN simulation for unmeasured quantity, t_{max}

Variable	Prior Density Parameters	Posterior Density Parameters	<i>B</i>
$V_{imp}(\text{rad/sec})$	$\mu' = 4.36$ $\sigma' = .24$	$\mu'' = 4.139$ $\sigma'' = .134$	2.72
$h(\text{in})$	$\mu' = 1.48$ $\sigma' = .05$	$\mu'' = 1.46$ $\sigma'' = .0394$	1.75
$t_{max}(\text{s})$	$\mu' = .00468$ $\sigma' = .00044$	$\mu'' = .0052$ $\sigma'' = .00026$	3.40

The B value is the ratio of the posterior to prior density functions evaluated at the updated mean value for each parameter.

6.3.2 Experimental Cylinder: Gaged Location to Non-Gaged Location

Another situation frequently encountered in engineering design involves decisions that need to be made for physical locations (or points in time) for which experimental or field data is not available. Ideally, all spatial and temporal points of interest can be observed during testing so as to inform designers. However, in most real-world applications, data (whether experimental or field) can typically only be gathered at a few discrete spatial and/or temporal locations within the system. Much research has been conducted on methods for efficient placement of sensors so

as to maximize the knowledge gained while satisfying practical constraints (see e.g., Guratzsch, 2006).

In the experimental cylinder example presented here, there are practical limitations on the number of strain gages that can be affixed to the outer surface of the cylinder. If too many gages are applied at once, the weight of the connecting wires will affect the manner in which the cylinder tumbles into the tank of water. Likewise, data-processing constraints limit the sampling rate and duration of measurement if too many gages are used at once. Therefore, it is useful to be able to extrapolate confidence in a validated predictive model from locations (both spatial and temporal) for which data has been observed to unmeasured locations.

The conceptual framework for this inference extrapolation is the same as for that discussed above for unmeasured quantities. The BN shown in Fig. 6.3 is identical except that the node labeled t_{max} is instead now labeled σ_{max_2021} to indicate peak stress at some unmeasured location (i.e. element 2021 in the LS-Dyna cylinder model). In this demonstration, a vector \mathbf{z} is the vector of observed values, taken at the midpoint between the two end caps. The location is labeled 15_CL in Fig. 4.4 and can be found in the appropriate column of Table 4.2. This location is represented in the LS-Dyna cylinder model by element 151. The target location will be 12" from the top end cap of the cylinder, and 90° off of the leading edge. Note in Fig. 4.4 that this location actually did have a strain gage (Labeled 12_+90), however, during the experimentation, that particular gage failed to return useful data due to an electrical short circuiting. This faulty-sensor scenario is frequently encountered in experimental research (see e.g. Fasanella et al. 2003), and therefore gives this example particular relevance.

As before, the WinBUGS package can be used to conduct the numerical integrations needed for the Bayesian inference procedure. Two chains (i.e. independent simulations

conducted simultaneously) are used with 100,000 iterations to help achieve a stable solution. The results are shown in Table 6.2.

Table 6.2 – Results of BN simulation for non-gaged location

Variable	Prior Density Parameters	Posterior Density Parameters	<i>B</i>
<i>V</i> (rad/sec)	$\mu = 4.36$ $\sigma = .218$	$\mu' = 4.125$ $\sigma' = .226$	0.562
<i>h</i> (in)	$\mu = 1.5''$ $\sigma = .05''$	$\mu' = 1.517''$ $\sigma' = .099''$	0.4976
$\sigma_{max_Elm_2021}$ (psi)	$\mu = 3493.3$ $\sigma = 284.1$	$\mu' = 2962$ $\sigma' = 284.1$	0.174

Note that in this case the *B* value for untested model prediction is lower than for the two input conditions *V_{imp}* and *h*. Additionally, the vector of observed data provides updated density functions that put the *B* value for all three parameters at less than 1.0, indicating reduced confidence. Using the model to extrapolate to the untested location is therefore not accepted based upon the observed data. Note also that in this example a vector of observed values from a location fairly close to the untested point of interest is used. Any vector of observed data (such as *D* from the previous example) could be used provided there is a corresponding output from the model.

6.3.3 Extrapolation to SRB Splashdown

The concept of confidence extrapolation with Bayesian networks is still an open research topic, and in this work there are many issues to be considered when attempting to extrapolate inferences from the simple aluminum cylinder experiments to the SRB forward skirt damage problem. The physical dimensions of the experimental cylinder discussed in Chapter 4 are of

course on a much smaller scale than those of the 130-ft-long SRB. Additionally, the impacts with the free water surface that occur in the laboratory experimentation take place at speeds much lower than the SRB impact velocities. Though the laboratory capabilities in this study are limited by practical constraints, investigation of extrapolation approaches and techniques can nonetheless provide for a general framework to be used in other similar work with fluid-structure impact investigations where testing facilities allow for models closer in scale to the real-world system.

It is worth noting that the field of scaled physical modeling for scientific study and engineering design is quite mature in many areas, particularly fluid mechanics and hydraulics. The scaling rules for translating laboratory experimental observations into the corresponding quantities in the actual system are known as similitude, and they are well-established for many areas of practical study. Recent advances in computing power have shifted many research activities into numerical modeling, but scaled physical modeling remains an active research area, particularly within hydraulics and hydraulic structures analysis. Recent work (Zanuttigh and Lamberti 2006) includes scaled physical modeling of low-crested, rubble-mound breakwater structures for comparison with 2D numerical predictions of velocity and flow fields. Lin and Demirbilek (2005) use scaled physical models to evaluate two numerical codes for wave prediction accuracy for a variety of inlet configurations. Within the structural analysis field, Bilello et al. (2004) used a small-scale bridge model to examine the dynamic response of the structure to a moving point load, with particular attention given to the issue of proper scaling of the mass quantity. Murphy et al. (1963) suggested that gravitational scaling effects may be ignored for dynamic analysis; however, Krauthammer (1991) lists these same effects as one of the primary sources of discrepancies between scaled models and actual systems. Dancygier

(1994) provides quantitative evidence of the distortional scaling effects for several types of problems at different scaling factors.

In a typical physical modeling study, the Buckingham- π theorem (Szűcs 1980; Baker et al. 1978) is invoked and the fundamental quantities governing the system are identified along with the basic units (comprised of the fundamental quantities) through dimensional analysis. Performing this exercise on the experimental cylinder example assuming free-fall conditions (i.e., no initial velocity) reveals three fundamental quantities: mass M , distance D , and time T . The basic units that define the structural properties of the aluminum cylinder can be given by length L , radius r , thickness h , elastic modulus E , and density ρ_c . The basic unit for water that is of interest in the cylinder impact problem is the density ρ_w . Lastly, given that the velocity of the cylinder at impact is a function of the free fall conditions, one dimensional approach could be to use the acceleration of gravity, g , as the basic governing unit.

As can be seen in Table 6.1, the basic units of the problem can be stated in terms of the fundamental quantities, with the numbers representing exponents, and sign denoting either a direct or inverse relationship. This results in, for example, the material density of the cylinder ρ_c , being represented by M^1D^{-3} , or M/D^3 .

Table 6.3 – Potential dimensional matrix for cylinder impact problem

	Cylinder Length, L	Cylinder Radius, r	Wall Thickness, h	Elastic Modulus, E	Material Density, ρ_c	Density of Water, ρ_w	Acceleration of Gravity, g
Mass, M	0	0	0	1	1	1	0
Distance, D	1	1	1	-1	-3	-3	1
Time, T	0	0	0	-2	0	0	-2

The 3×7 dimensional matrix shown in Table 6.1 is reduced into row echelon form using Gauss-Jordan elimination [Strang, 1988], resulting in the matrix $A =$

$$\begin{bmatrix} 1 & 1 & 1 & 0 & 0 & 0 & -1 \\ 0 & 0 & 0 & 1 & 0 & 0 & 1 \\ 0 & 0 & 0 & 0 & 1 & 1 & -1 \end{bmatrix}. \text{ Finding the set of null space vectors } \mathbf{x}_i \text{ for which } \mathbf{A}\mathbf{x}_i = 0$$

reveals the dimensionless parameters governing the system. The set of null space vectors for the matrix A is:

Table 6.4 – Null set vectors for potential cylinder impact formulation

	\mathbf{x}_1	\mathbf{x}_2	\mathbf{x}_3	\mathbf{x}_4
Cylinder Length, L	-1	-1	0	1
Cylinder Radius, r	1	0	0	0
Wall Thickness, h	0	1	0	0
Elastic Modulus, E	0	0	0	-1
Material Density, ρ_c	0	0	-1	1
Density of Water, ρ_w	0	0	1	0
Acceleration of Gravity, g	0	0	0	1

These vectors indicate the four dimensionless parameters for the cylinder-water impact problem to be r/L , h/L , ρ_w/ρ_c , and $L\rho_c g/E$. Regardless of the scaling factor being used, measured quantities in the model can be applied to the full-scale system provided these parameters are held constant. Note that the individual units (e.g., r , h , E , etc.) do not have to vary according to the scaling factor, so long as the dimensionless parameter remains constant. Dimensional analysis is

useful in physical modeling because it reveals the fundamental relationships that provide the link between the scaled experiments and the full-sized system. It has the added benefit of being able to identify units which might seem important from an intuitive standpoint but which are actually not needed for scaling purposes. However, the modeler must still determine which basic units are important to the problem formulation. Note that the final number of dimensionless parameters will be equal to the number of basic units minus the number of fundamental quantities.

The first three of the dimensionless parameters derived above are straightforward, and they concern the geometric properties of the cylinder and relative densities of the fluid and structure, respectively. It is the fourth dimensionless parameter, $L\rho_c g/E$ that presents some interesting considerations for scaled modeling. Consider the SRB splashdown scenario in the general sense of a thin-walled cylinder falling freely onto a free water surface. A scaled model of the SRB splashdown M that satisfies the similitude conditions will keep the same value of this fourth dimensionless parameter, as shown in Eq. 6.6:

$$\frac{L_{SRB} \rho_{SRB} g_{SRB}}{E_{SRB}} = \frac{L_M \rho_M g_M}{E_M} \quad (6.6)$$

If materials are available to the modeler that possess the same stiffness E and density ρ as the SRB (recall that in this study a common aluminum alloy was used to construct the small-scale cylinder), then the ρ/E ratio remains the same and cancels out of Eq. 6.6. Satisfying the similitude requirements therefore reduces to $L_{SRB} g_{SRB} = L_M g_M$, and it becomes clear that if the same material properties (E and ρ) are used in both the model and real-world system, then the physical dimension L of the SRB cannot be scaled down without also scaling up g by an equivalent amount. In scaled modeling studies where the gravitational effects must be increased in order to satisfy the dimensionless relational constraints, large centrifuges are often employed

to apply an increased acceleration field uniformly to the model. Situations such as this are often encountered in geotechnical engineering studies where scaling of properties such as soil density and cohesive parameters is not feasible. A large centrifuge was recently employed during forensic analysis of the 17th St. Canal levee I-wall failure in New Orleans during Hurricane Katrina (Sasanakul et al. 2008).

Returning to Eq. 6.6, if g is left constant between both the model and SRB (a necessary constraint in most physical model studies), then it follows that in order to scale down the physical dimension L_{SRB} , the density to stiffness ratio ρ_{SRB}/E_{SRB} must be scaled up by some equivalent amount. In the cylinder experiment undertaken in this study, there are several practical limitations concerning the experimental setup (these are discussed in Chapter 4). The decision to use aluminum is in keeping with the material type experiencing failure in the actual SRB; this results in model values for stiffness E_M and material density ρ_M that approximate (relative to other scalable quantities) those values for the actual structural system. Table 6.3 shows the scaling factors resulting between the actual SRB and the experimental cylinder used in this study.

Table 6.5 – Scaling ratios between SRB and experimental cylinder

Quantity	SRB	Cylinder Test	SRB/Cylinder
Length	130 ft	2.5 ft	52
Radius	13 ft	0.125 ft	52
Wall Thickness	0.25 - 0.75 in	0.025 in	10 - 30
Mass	148,000 lbs	0.875 lbs	169,143
Material Density	0.099 lbs/in ³	0.099 lbs/in ³	1.0
Density of Water	64.3 lbs/ft ³	62.4 lbs/ft ³	1.03
Impact Velocity	200 – 400 in/sec	90 – 130 in/sec	2.22 – 3.08

However, since use of a large centrifuge for scaling of g is not an option in this study, the proportional scaling constraints as defined using dimensional analysis are not fully satisfied in the strict context of the free-fall SRB problem.

An alternate dimensional formulation would be to include a single velocity term V for the SRB at impact, while considering the total mass, m_{SRB} , in place of the material density term. The elastic modulus, E is also considered in addition to the density of water ρ_w and the SRB radius and wall thickness. This new formulation results in three dimensionless parameters, which allows for a single dimensionless term ξ to be constructed for the generalized problem of a cylindrical structure experiencing blunt water impact:

$$\xi = \frac{V^2 m^2}{Et^2 \rho_w r^4} \quad (6.7)$$

This dimensionless parameter is important because it provides the mathematical linkage between the SRB and cylinder model for which validation has been performed. Note that the only variable treated as an initial condition for the finite element model runs in this study is the impact velocity, V . Using the results for peak stress in the cylinder and SRB models at several different values for V , the linking function for the two models can be approximated with a simple polynomial regression equation:

$$\sigma(\xi) = -5237.6\xi^2 + 65237\xi + 9248.1 \quad (6.8)$$

This expression has an R^2 value of .9993 when plotted through the available model predictions for different impact velocities. Fig. 6.5 shows the model predictions for peak stress plotted as a function of the dimensionless parameter ξ .

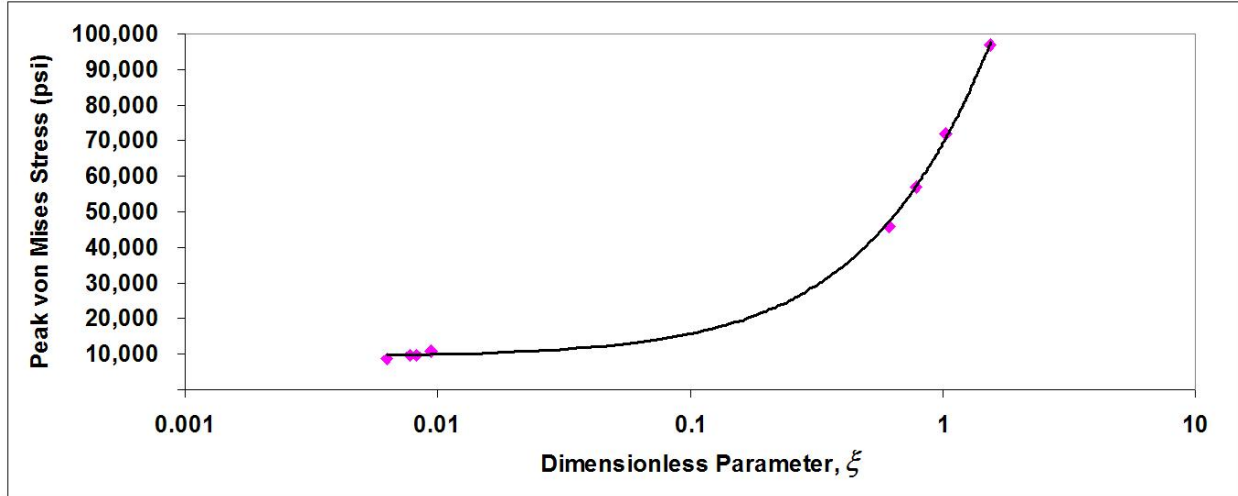


Fig. 6.5 – Linking function (Eq. 6.8) plotted through FE model predictions for peak stress

The higher stress values are taken for SRB drop tests taken at different impact velocities, while the lower stress values are from the cylinder model simulations. The scatter within each cluster of points is due to variation in the impact velocity, V . It can be seen that there is considerable difference between each cluster of points, and the x -axis in Fig. 6.5 is plotted in logarithmic scale for the sake of clarity. The separation between the ζ values for the cylinder and SRB predictions is due to the scaling ratios between the cylinder and SRB departing from 1.0.

Based on the experimental design performed thus far, a potential Bayesian network concerning this problem could be constructed with the aforementioned dimensionless parameter ζ used as a linking variable, as shown in Fig. 6.6. For the purposes of this exercise, the cylinder parameters across the top row of the BN (r , t , m , E , and ρ_w) are treated as constants, and the only variables considered to be random are the impact velocities for the cylinder and SRB problem domains, V_{cyl} and V_{SRB} , respectively. Due to the separation between the ζ values for the cylinder and SRB domains, a multiplier α is introduced to bring the cylinder values in line with the SRB values. Eq. 6.8 is then used to compute the peak stress based on the ζ value.

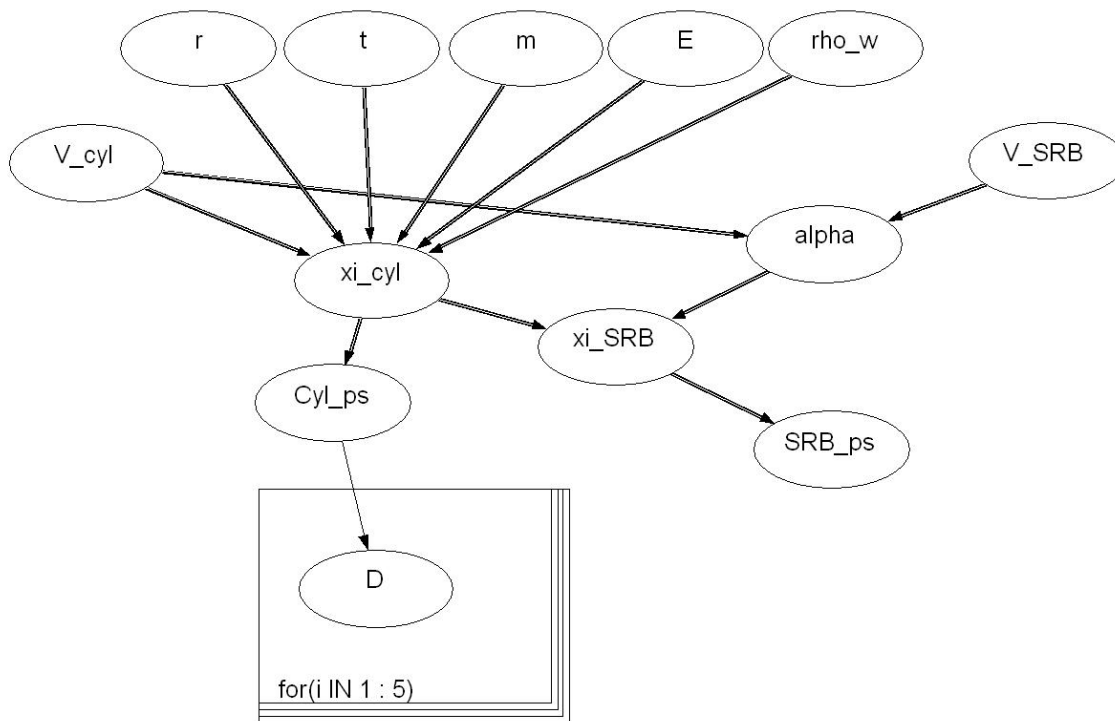


Fig. 6.6 – BN for extending confidence quantification to SRB splashdown

The BN provides a way to quantify the confidence in the peak stress prediction (and in turn, the risk prediction) for the SRB based upon the laboratory test, \mathbf{D} , data obtained for the cylinder. The dimensionless parameter ξ allows for the physics of the real-world system to be translated, via the laws of similitude and dimensional analysis, into a separate, though observable problem domain.

For the implementation of the BN shown in Fig. 6.6, the peak stress measurements for Sta9_CL from five cylinder drop tests are used such that $\mathbf{D} = \{8379.65, 8567.88, 8903.35, 9166.04, 8892.66\}$, with units in psi. Note that this location corresponds to that used to derive Eq. 6.8 using the LS-Dyna predictions. The BN is evaluated using the WinBUGS software, and

the probability density returned is treated as the posterior density for peak stress in the SRB. This density function is compared to the prior density for peak stress in the SRB, as computed from the Monte Carlo simulations used to determine p_f for the SRB in Chapter 5. Fig. 6.7 shows the prior and posterior densities for peak stress in the SRB forward skirt.

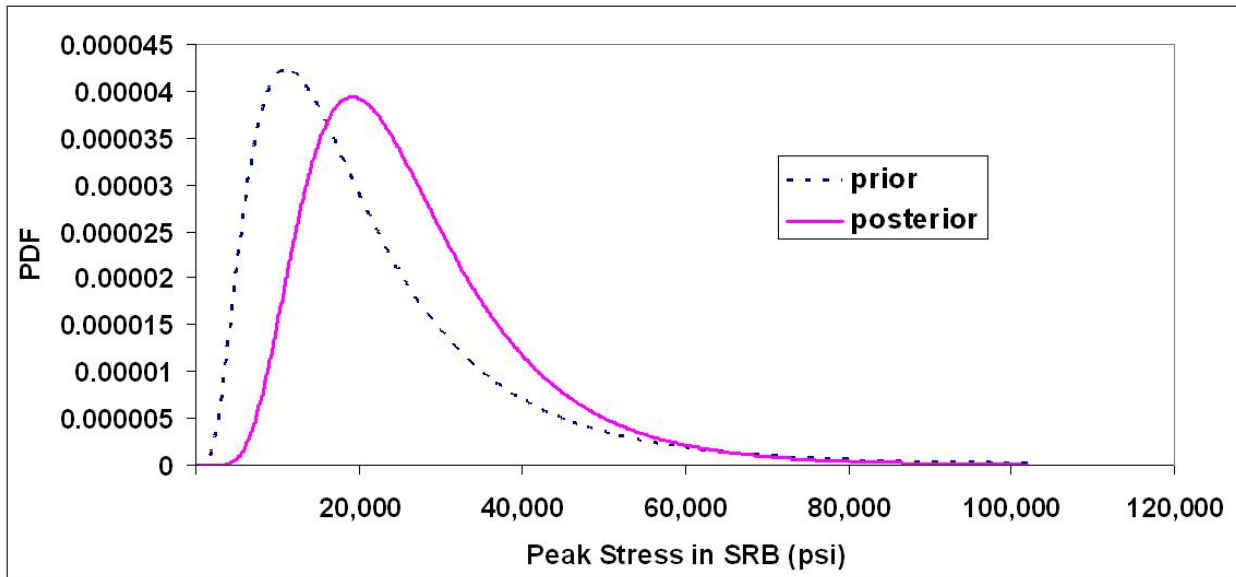


Fig. 6.7 – Prior and posterior density functions for peak stress in the SRB forward skirt

Evaluation of the Bayes factor B , at the mean value of the model prediction (prior), returns a value of 1.489, indicating a confidence in the SRB peak stress model of .5982. Therefore implementation of the BN results in a modest increase in confidence for the model.

6.4 Summary and Conclusions

In this chapter the concept of Bayesian networks for confidence extrapolation has been explored in the context of the experimental cylinder work conducted as part of the study of SRB splashdown. The concept is demonstrated using data collected with the experimental cylinder,

and inferences are applied to predictions made by the computational model constructed with LS-Dyna concerning both unmeasured quantities and locations on the cylinder for which no data was collected. The subject of similitude and dimensional analysis is discussed as part of an exploration of the concept of extrapolating inferences gained about a computational model of a scaled experimental model to the actual real-world system.

Bayesian networks are useful as a tool for fully utilizing scarce observational data towards quantifying confidence in a computational model for untested problem domains. In this study, a small-scale experiment is conducted using a simple aluminum cylinder in order to gain insight into the nature of general fluid-structure impact problems. However, the scaling rules of similitude are not fully observed due to several practical constraints, and the results of the experiment cannot be applied directly to the SRB splashdown problem. There does appear to be potential for application of the Bayesian network methodology to scaled experimental modeling, provided a suitable mathematical linking function can be found that allows for the model predictions in each domain to be expressed in terms of the same quantity.

The overarching purpose of the methodology presented here is to increase the confidence in the models used for risk assessment of the SRB splashdown event using measured laboratory data. To accomplish this, a mathematical link is established between the output of the SRB numerical model and the predictions of the numerical model of the laboratory cylinder. Such a link is proposed by deriving several dimensionless quantities and then combining in order to express output from both the SRB and cylinder models in terms of the same quantity. Application of this methodology to the SRB model and cylinder validation data results in a modest increase in confidence for the SRB peak stress prediction.

CHAPTER VII

CONCLUSIONS AND FUTURE WORK

7.1 Overview

Fluid-structure impact problems present many challenges for engineers and systems designers in the aerospace and naval architecture fields. Long-term forecasts for both space exploration and ship building indicate that analysis of structural impact onto free water surfaces will remain a relevant topic for the foreseeable future. As computational resources become more widely available, designers are likely to study these sorts of problems even more closely in order to further optimize structural designs.

Fluid-structure impact problems typically contain significant inherent variability due to environmental conditions and impact trajectories. Additionally, full-scale test data and/or field measurements are expensive to obtain, leading to informational uncertainty and presenting challenges for model validation and reduction of model uncertainty. Therefore system designers are presented with several forms of uncertainty that must be appropriately quantified if accurate and meaningful risk assessments for fluid-structure impact are to be conducted.

The SRB forward skirt problem is presented here as one real-world example of structural failure resulting from impact with a free fluid surface. The work described in each chapter is conducted in order to address challenges encountered in previous risk assessments conducted by the author for the SRB splashdown event. A review of available theory and literature pertaining to fluid-structure impact has shown that coupled Eulerian-Lagrangian finite element analysis offers a flexible, straightforward approach for modeling for the purposes of risk assessment for

practical structures. A systematic framework has been demonstrated for estimating the numerical error encountered in the finite element approach to fluid-structure impact analysis. Attention is given to the dual-mesh nature of these problems, in which the resolution of both the fluid and structural domains must be carefully considered when constructing models with manageable computational requirements. It has been shown that close attention must be given to the relative mesh resolutions within the fluid and structure problem domains, and that the iterative coupling scheme used to reconcile the two can have a significant influence on the model results. Since this work has been undertaken in tandem with a validation procedure, experimental data is available for use in quantifying the numerical error and establishing sufficient mesh resolution.

This experimental data is intended ultimately to increase the confidence in the predictions from the finite element models used to simulate SRB splashdown and to predict the probability of structural damage. Since full-scale SRB testing is not an option, a small-scale laboratory experimental assembly has been used to measure the dynamic stress response of a hinged, thin-walled cylinder allowed to fall over onto a free water surface. Results from this testing have been used within a validation framework for a corresponding finite element model constructed with LS-Dyna, with experimental uncertainty considerations included. A simple qualitative validation has shown promising agreement between the measured stress history curves and those predicted by the model. However, quantitative validation conducted via hypothesis testing with both classical and Bayesian metrics resulted in model rejection in most instances. Model tuning and calibration have been shown to improve the stress predictions at discrete locations on the cylinder, but the improvement is not seen for all locations.

The finite element approach to fluid-structure impact modeling has shown promising qualitative results for the simple laboratory cylinder, indicating that the approach should be applicable to the SRB problem domain as well. However, in order to truly capture the failure mechanism affecting the forward skirt, the buckling nature of the damage must be fully understood. In this work, the issue of buckling has been presented generally, with attention given to dynamic pulse buckling for its seeming applicability to the splashdown problem. A review of previous work has shown that although the dynamic nature of the splashdown loads contributes to the observed buckling, the loading durations, pressure pulse magnitudes, and deformation patterns appear to rule out true dynamic pulse buckling. A numerical approach has been undertaken using a refined finite element model of the forward skirt and the nonlinear LS-Dyna analysis code, and predictions from the model have been compared to classical buckling stability conditions. The results indicate that the term “buckling” is appropriate for describing the predicted damage, at least according to classical plate and cylinder stability theory. A qualitative assessment of the model predictions concerning deformed shape of the SRB and observed damage patterns has shown promising results. The refined finite element model has been used to update the critical forward skirt impact velocity, and the updated risk assessment has shown improved agreement with the observed failure rate.

This study has covered an array of topics pertinent to modeling of fluid-structure impact problems for the purposes of structural risk assessment. Experimental data has been gathered using a small aluminum cylinder in a laboratory setting, and yet the ultimate risk assessment has been applied to the much larger SRB problem. To address this issue, a methodology has been explored for extending the confidence in the cylinder model prediction obtained through validation exercise to the full-scale SRB problem domain. The proposed methodology employs

Bayesian networks to gage confidence in a model prediction for an untested problem domain. Dimensional analysis has been discussed for the purposes of deriving a linking function that predicts stress values in both the cylinder and SRB models. This linking function has been used within a Bayesian network formulation for quantifying confidence in the SRB model prediction based on the validated cylinder model. Results from the extrapolation methodology using cylinder test data have shown a modest, though not insignificant, increase in the confidence in the SRB model prediction for peak stress.

7.2 Future Work

Fluid-structure impact analysis, particularly involving large structural displacements such as the SRB forward skirt failures, remains a challenging field of engineering study. This research has explored several aspects of fluid-structure impact analysis in the context of a risk assessment framework for the SRB splashdown problem. Within each area, further study will improve upon the understanding and capabilities of researchers performing risk analysis for such problems.

Rapidly-developing numerical analysis techniques such as boundary element formulations and smooth particle hydrodynamics (SPH) have become recently available through commercial finite element packages such as LS-Dyna. Exploration of these methods could lead to improved accuracy and reduced analysis times for problems such as the SRB splashdown. Adaptive mesh-refinement techniques, in which the spatial and temporal discretizations are optimally controlled over the course of the analysis, present new problems for study in regards to numerical error in fluid-structure impact analysis.

The nonlinear finite element analysis of SRB forward skirt buckling indicates that the observed damage patterns can be produced as a result of water impact. Additional simulations

will reveal which portions of the SRB (around the circumference) are most vulnerable to buckling during slapdown, and at what impact velocities buckling leads to permanent deformation.

Results from the validation exercise indicate that additional model tuning and calibration is needed to provide model acceptance for multiple locations on the cylinder. A systematic framework needs to be implemented for carefully adjusting both global and local model parameters (within physically meaningful bounds) to achieve optimum agreement with observed data.

The confidence extrapolation methodology has been presented and explored for application to the SRB problem using the small-scale laboratory cylinder data. Additional work is needed to more fully establish a mathematical linking function between the cylinder and SRB model responses. In particular, additional experimental testing could be conducted with proper scaling of additional parameters such as elastic modulus, structural mass, and wall thickness.

REFERENCES

1. Abrahamson, G., and Goodier, J. (1962). "Dynamic plastic flow buckling of a cylindrical shell from uniform radial impulse." *Proceedings of the Fourth U.S. National Congress of Applied Mechanics*. Berkeley, CA, June, 939-950.
2. Ainsworth, M., and Oden, J. T. (2000). *A posteriori error estimation in finite element analysis*. John Wiley & Sons, Inc., New York.
3. Alvin, K. F., Oberkampf, W. L., Diegert, K. V., and Rutherford, B. M. (1998). "Uncertainty quantification in computational structural dynamics: A new paradigm for model validation." *Proceedings of the 16th International Modal Analysis Conference*. Santa Barbara, CA, February 2-5, 1,191-1,198.
4. Anderson, T. W. (1984). *An introduction to multivariate statistical analysis*. Second Edition. John Wiley & Sons, New York.
5. Anderson, D. L., and Lindberg, H. E. (1968). "Dynamic pulse buckling of cylindrical shells under transient lateral pressures." *AIAA Journal*, **6(4)**, April.
6. Ang, A. H-S., and Tang, W. H. (1975). *Probability concepts in engineering planning and design, Vol. I: Basic principles*. John Wiley & Sons, New York.
7. Ang, A. H-S., and Tang, W. H. (1984). *Probability concepts in engineering planning and design, Vol. I: Decision, risk, and reliability*. John Wiley & Sons, New York.
8. Aquelet, N., Souli, M., and Olovsson, L. (2006). "Euler-Lagrange coupling with damping effects: Application to slamming problems." *Computer Methods in Applied Mechanics and Engineering*, **195**, 110-132.
9. Armand, J. L., and Cointe, R. (1986). "Hydrodynamic impact analysis of a cylinder." In: *Proceedings Fifth International Offshore Mechanical and Arctic Engineering Symposium*. Tokyo, Japan. Vol. 1, 609-634. ASME.
10. Baker, W. E., Westine, P. S., and Dodge, F. T. (1978). *Similarity methods in engineering dynamics*. Hayden Book Co., Rochelle Park, NJ.
11. Barlag, S., and Rothert, H. (2002). "An idealization concept for the stability analysis of ring-reinforced cylindrical shells under external pressure." *Non-Linear Mechanics*, **37**, 745-756.
12. Bates, B. C., Kundzewicz, Z. W., Wu, S., and Palutikof, J. P.(Eds.). (2008). "Climate change and water." Technical Paper of the Intergovernmental Panel on Climate Change, IPCC Secretariat, Geneva.

13. Battistin, D. and Iafrati, A. (2003). "Hydrodynamic loads during water entry of two dimensional and axisymmetric bodies." *Journal of Fluids and Structures*, **17**, 643-664.
14. Bereznitski, A. (2001). "Slamming: The role of hydroelasticity." *International Shipbuilding Progress*, **4**, 333-351.
15. Bessette, G. C., Becker, E. B., Taylor, L. M., and Littlefield, D. L. (2003). "Modeling of impact problems using an h-adaptive, explicit Lagrangian finite element method in three dimensions." *Computer Methods in Applied Mechanics and Engineering*, **192**, 1,649-1,679, March.
16. Bilello, C., Bergman, L. A., and Kuchma, D. (2004). "Experimental investigation of a small-scale bridge model under a moving mass." *ASCE Journal of Structural Engineering*, **130(5)**, 799-804.
17. Billah, K. Y., and Scanlan, R. H. (1991). "Resonance, Tacoma Narrows Bridge failure, and undergraduate physics textbooks." *American Journal of Physics*, **59**, 118-124.
18. Blachut, J. (2002). "Buckling of externally pressurized barreled shells: A comparison of experiment and theory." *Pressure Vessels and Piping*, **79**, 507-517.
19. Broderick, L. L., Leonard, J. W. (1995). "Nonlinear response of membranes to ocean waves using boundary and finite elements." *Ocean Engineering*, **22**, 731-745.
20. Brush, D., and Almroth, B. (1975). *Buckling of bars, plates, and shells*. McGraw-Hill Book Company, New York.
21. Bushnell, D. (1985). *Computerized buckling analysis of shells*. Martinus Nijhoff Publishers, The Netherlands.
22. Campbell, I. M. C., and Weynberg, P. A. (1980). "Measurement of parameters affecting slamming." Report No. 440, Wolfson Unit of Marine Technology, Tech. Rep. Center No. OT-R-8042, Southampton, UK.
23. Carcaterra, A., and Ciappi, E. (2004). "Hydrodynamic shock of elastic structures impacting on the water: Theory and experiments." *Journal of Sound and Vibration*, **271**, 411-439.
24. Chajes, A. (1974). *Principles of structural stability theory*. Prentice-Hall, Englewood Cliffs, New Jersey.
25. Clarke, C. W., and Shen, Y. C. (1998). "The development of a rotorcraft water-impact analysis methodology." *AHS/SAFE Crashworthiness Specialists Meeting on Crash Safety*. Phoenix, AZ, September.
26. Clayton, J., and Craft, M. (1995). "SRB water impact loads." United Technologies USBI Analysis Memorandum. USBI-AM-95-0219, April 28.

27. Cointe, R. (1991). "Free surface flows close to a surface-piercing body." In: *Mathematical Approaches in Hydrodynamics*, T. Miloh (ed.), Soc. Ind. Appl. Maths, Philadelphia, PA, 319-334.
28. Dancygier, A. N. (1994). "Quantitative evaluation of effect of gravity on small-scale modeling." *ASCE Journal of Engineering Mechanics*, **121(7)**, 773-778.
29. Defense Modeling and Simulation Office (DMSO), Dept. of Defense. (1996). *Verification, validation, and accreditation (VV&A) recommended practices guide*. Office of the Director of Defense Research and Engr., www.dmsomil/docslib, Alexandria, VA, April.
30. Dobrovolskaya, Z. N. (1969). "On some problems of similarity flow of fluid with a free surface." *Journal of Fluid Mechanics*, **36**, 805-829.
31. Dobyns, A. (1998). "Bird strike analysis of S-92 vertical tail cover using DYTRAN." Presented at the *AHS Affordable Composite Structures Conference*. Bridgeport, CT, October 7-8.
32. Engle A., and Lewis, R. (2003). "A comparison of hydrodynamic impacts prediction methods with two dimensional drop test data." *Marine Structures*, **16**, 175-182.
33. Faltinsen, O., Kjaerland, O., and Nottveit, A. (1977). "Water impact loads and dynamic response of horizontal circular cylinders in offshore structures." *Offshore Technology Conference*. Paper No. OTC 2741, Vol. 1. Houston, TX, May 2-5.
34. Fasanella, E. L., Jackson, K. E., Sparks, Chad E., and Sareen, A. K. (2003). "Water impact test and simulation of a composite energy absorbing fuselage section." *American Helicopter Society 59th Annual Forum*, Phoenix, AZ, May 6-8.
35. Garrison, C. J. (1996). "Water impact loads on circular structural members." *Applied Ocean Research*, **18**, 45-54.
36. Gilkes, G. R., Richardson, S., and Spiegelhalter, D. J. (1996). *Markov Chain Monte Carlo in Practice: Interdisciplinary Statistics*. Chapman and Hall/CRC. London.
37. Gilmanov, T. G., Tieszen, L. L., Wylie, B. K., Flanagan, L. B., Frank, A. B., Haferkamp, M. R., Meyers, T. P., and Morgan, J. A. (2005). "Integration of CO₂ flux and remotely-sensed data for primary production and ecosystem respiration analyses in the Northern Great Plains: Potential for quantitative spatial extrapolation." *Global Ecology & Biogeography*, **14**, 271-292.
38. Guratzsch, R. (2006). "Sensor placement optimization under uncertainty for structural health monitoring of hot aerospace structures." Ph.D. Dissertation. Vanderbilt University, Nashville, TN.

39. Haldar, A., and Mahadevan, S. (2000). *Probability, reliability, and statistical methods in engineering design*. John Wiley & Sons, Inc., New York.
40. Hallquist, J. (2006). *LS-Dyna Theoretical Manual*. Livermore Software Technology Company.
41. Heckerman, D. (1996). "A tutorial on learning with Bayesian networks." Microsoft Corporation. Technical Report MSR-TR-95-06.
42. Hills, Richard G., and Leslie, I. H. (2003). "Statistical validation of engineering and scientific models: Validation experiments to application." Technical Report No. SAND2003-0706, Sandia National Laboratories, Albuquerque, NM, March.
43. Hills, R. G., and T. G. Trucano. (2001). "Statistical validation of engineering and scientific models: A maximum likelihood based metric." Technical Report No. SAND2001-1783, Sandia National Laboratories, Albuquerque, NM.
44. Howison, S. D., Ockendon, J. R., and Wilson, S. K. (1991). "Incompressible water-entry problems at small deadrise angles." *Journal of Fluid Mechanics*, **222**, 215-230.
45. Hughes, K., Campbell, J., and Vignjevic, R. (2008). "Application of the finite element method to predict the crashworthy response of a metallic helicopter under floor structure onto water." *International Journal of Impact Engineering*, **35**, 347-362.
46. Jackson, K., Fuchs, Y. "Comparison of ALE and SPH Simulations of Vertical Drop Tests of a Composite Fuselage Section into Water." *10th International LS-DYNA® Users Conference*. Dearborn, MI. June 8-10, 2008.
47. Jeffreys, H. (1961). *Theory of probability*. 3rd Edition. Clarendon Press, Oxford.
48. Jensen, F. V. (1996). *An introduction to Bayesian networks*. UCL Press, London.
49. Kaplan, P., and Silbert, M. H. (1976). "Impact forces on platform horizontal members in the splash zone." *Offshore Technology Conference*. Paper No. OTC 2498. Houston, TX. May, 3-6.
50. Karagiozova, D., and Jones, N. (2000). "Dynamic elastic-plastic buckling of circular cylindrical shells under axial impact." *International Journal of Solids and Structures*, **37**, 2005-2034.
51. Kirkpatrick, S., and Holmes, B. (1988). "Structural response of thin cylindrical shells subjected to impulsive external loads." *AIAA Journal*, **26**, 93-103.
52. Knapp, J., Altmann, E., Niemann, J., and Werner, K.-D. (1998). "Measurement of shock events by means of strain gauges and accelerometers." *Measurement*, **24**, 87-96.

53. Krauthammer, T. (1991). "Discussion of dynamic response of shallow buried cylindrical structures." *ASCE Journal of Engineering Mechanics*, **117(8)**, 1923-1927.
54. Kross, D. A., Keifling L. A., Murphy, N. C., and Rawls, E. A. (2005). "Space shuttle solid rocket booster initial water impact loads and dynamics—analysis, tests, and flight experience." AIAA Paper 83-0956. NASA Marshall Space Flight Center, Huntsville, AL. January.
55. Lin, L., and Demirbilek, Z. (2005). "Evaluation of two numerical wave models with inlet physical model." *ASCE Journal of Waterway, Port, Coastal, and Ocean Engineering*, **131(4)**, 149-161.
56. Lin, Ming-Chung, and Shieh, Li-Der. (1997). "Flow visualization and pressure characteristics of a cylinder for water impact." *Applied Ocean Research*, **19**, 101-112.
57. Lindberg, H. (1964). "Buckling of a very thin cylindrical shell due to an impulsive pressure." *ASME Journal of Applied Mechanics*, **31**, 267-272.
58. Lindberg, H. E., and Florence, A. L. (1987). *Dynamic pulse buckling: Theory and experiment*. Martinus Nijhoff Publishers, Dordrecht, The Netherlands.
59. Lindley, D. V. (1965). *Introduction to probability and statistics from a Bayesian viewpoint: Part I, Probability and Part 2, Inference*. University Press, Cambridge.
60. Lu, C. H., He, Y. S., and Wu, G. X. (2000). "Coupled analysis of nonlinear interaction between fluid and structure during impact." *Journal of Fluids and Structures*, **14**, 127-146.
61. Mahadevan, S., and Rebba, R., "Computational Model Validation under Uncertainty," *Proceedings of the 9th International Conference on Applications of Statistics and Probability in Civil Engineering*, San Francisco, California, USA, July 6-9, 2003.
62. Mahadevan, S., and Rebba, R. (2005). "Validation of reliability computational models using Bayes networks." Submitted to *J. of Reliability Engineering and System Safety*.
63. Maity, D., and Bhattacharyya, S. K. (2003). "A Parametric study on fluid-structure interaction problems." *Journal of Sound and Vibration*, **263**, 917-935.
64. Majamäki, Jyrki. (2002). "Impact simulations of a composite helicopter structure with MSC.Dytran." Eurocopter Deutschland, Germany.
65. Mathisen, K. M., Hopperstad, O. S., Okstad, K. M., and Berstad, T. (1999). "Error estimation and adaptivity in explicit nonlinear finite element simulation of quasi-static problems." *Computers and Structures*, **72**, 627-644, August.
66. Mathon, C., and Limam, A. (2006). "Experimental collapse of thin cylindrical shells submitted to internal pressure and pure bending." *Thin-Walled Structures*, **44**, 39-50.

67. McFadden, P. (1999). "Data Acquisition System (DAS) data evaluation with respect to SRB rotational behavior at water impact." United Technologies USBI Analysis Memorandum USBI-AM-99-0473, February 24.
68. Mei, X., Liu, Y., and Yue, D. K. P. (1999). "On the water impact of general two-dimensional sections." *Applied Ocean Research*, **21**, 1-15.
69. Michler, C., Hulshoff, S., van Brummelen, H., Bijl, H., and de Borst, R. (2002). "Space-time discretizations for fluid-structure interaction." *Fifth World Congress on Computational Mechanics*. Vienna, Austria.
70. Miller, J. R., Turner, M. G., Smitchwick, E. A., Dent, C. L., and Stanley, E. H. (2004). "Spatial extrapolation: The science of predicting ecological patterns and processes." *BioScience*, **54**, 310-320.
71. Mitchell, K. (2003). *Reliability analysis of solid rocket booster splashdown sequence and confidence bound formulation*. Master's Thesis. Vanderbilt University, Nashville, TN.
72. Mitchell, K. N., Mahadevan, S. "SRB Splashdown Analysis and Structural Damage Risk Assessment." *ASCE Earth and Space 2004: Engineering, Construction, and Operations in Challenging Environments*. Houston, TX. 2004.
73. Mitchell, K., Mahadevan, S., Peck, J., and Townsend, J. (2003). "Reliability analysis of solid rocket booster splashdown." AIAA 2003-1481. *5th AIAA Non-Deterministic Approaches Forum*. Norfolk, VA.
74. MSC Software. *MSC DYTRAN Theory Manual*. Version 2002. November 2001.
75. MSC Software. *MSC DYTRAN User's Guide*. Version 2002. November 2001.
76. Murphy, G., Young, D. F., and Martin, C. W. (1963). "Use of models to predict the dynamic response of dynamically loaded underground structures." *Technical Report RDT-TDR-63-3064*, Iowa State University, Ames, IA.
77. NASA. (2009). "NASA tests largest rocket parachutes ever for Ares I." *ScienceDaily*. May 20. <<http://www.sciencedaily.com/releases/2009/05/090520112439.htm>>.
78. National Research Council. (1987). *Responding to changes in sea level: Engineering implications*. National Academy Press.
79. Novozhilov, V. V. (1953). *Foundations of the nonlinear theory of elasticity*. Greylock Press, Rochester, NY.
80. Oberkampf, W. L., and Trucano, T. G. (2002). "Verification and validation in computational fluid dynamics." *Progress in Aerospace Sciences*, **38 (3)**, 209-272.

81. O'Daniel, J., Koudela, K., and Krauthammer, T. (2005). "Numerical simulation and validation of distributed impact events." *International Journal of Impact Engineering*, **31**, 1,013-1,038.
82. Olovsson, L., Simonsson, K., and Unosson, M. (2005). "Selective mass scaling for explicit finite element analysis." *International Journal for Numerical Methods in Engineering*, **63**, 1,436-1,445.
83. Ooi, J. T. L., Webb, J. R., and Zhou, D. (2007). "Extrapolation theory and the pricing of REIT stocks." *Journal of Real Estate Research*, **29**, 27-56.
84. Peeters, I., Van Oosta, K., Goversa, G., Verstraetena, G., Rommensa, T., and Poesena, J. (2008). "The compatibility of erosion data at different temporal scales." *Earth and Planetary Science Letters*, **265**, 138-152.
85. Pegg, N. G. (1994). "Dynamic pulse buckling of cylindrical structures." *Marine Structures*, **7**, 189-212.
86. Pegg, N. G. (1991). "Dynamic pulse buckling of cylinders of various a/h ratios." *Computers and Structures*, **39**(½), 173-183.
87. Pegg, N. G. (1992). "A numerical study of dynamic pulse buckling of ring-stiffened cylinders." *Computers and Structures*, **44**(6), 1,205-1,214.
88. Peseux, B., Gornet, L., and Donguy, B. (2005). "Hydrodynamic impact: Numerical and experimental investigations." *Journal of Fluids and Structures*, **21**, 277-303.
89. Pickle, L. W., Hao, Y., Jemal, A., Zou, Z., Tiwari, R. C., Ward, E., Hachey, M., Howe, H. L., and Feuer, E. J. (2007). "A new method of estimating United States and state-level cancer incidence counts for the current calendar year." *CA: A Cancer Journal for Clinicians*, **57**, 30-42.
90. Press, S. J. (1989). *Bayesian Statistics: Principles, Models, and Applications*. John Wiley & Sons, New York.
91. Radovitzky, R., and Ortiz, M. (1999). "Error estimation and adaptive meshing in strongly nonlinear dynamic problems." *Computer Methods in Applied Mechanics and Engineering*, **172**, 203-240, April.
92. Rebba, R. (2005). *Model validation and design under uncertainty*. PhD Dissertation. Vanderbilt University, Nashville, TN.
93. Rebba, R., and Mahadevan, S., "Verification and Validation of Simulation Models under Uncertainty," *Proceedings of the 7th U.S. National Congress on Computational Mechanics*, Albuquerque, New Mexico, USA, July 2003.

94. Roache, P. J. (1998). *Verification and validation in computational science and engineering*. Hermosa Publishers, Albuquerque, NM.
95. Roberson, J. A., and Crowe, C. T. (1997). *Engineering fluid mechanics*. Sixth Edition. John Wiley & Sons, Inc., New York.
96. Rodier, R. W., Moorg, R. D., and Kross, D. A. (1984). "136-foot main parachute for recovery of space shuttle solid rocket boosters." AIAA Paper 84-0804. NASA Marshall Space Flight Center, Huntsville, AL. April.
97. Rogers, W. P., et al. (1986). "Report of the Presidential Commission on the space shuttle Challenger accident." *Executive Order 12546*.
98. Roy, Christopher J. (2005). "Review of code and solution verification procedures for computational simulation." *Journal of Computational Physics*, **205**, 131-156. May.
99. Rust, W., and Schweizerhof, K. "Finite element limit load analysis of thin-walled structures by ANSYS (implicit), LS-DYNA (explicit), and in combination." *Thin-Walled Structures*, **41**, 227-244.
100. Sarpkaya, T., and Isaacson, M. (1981). *Mechanics of wave forces on offshore structures*. Van Nostrand Reinhold Company, New York.
101. Sasanakul, I., et al. (2008). "New Orleans levee system performance during Hurricane Katrina: 17th Street Canal and Orleans Canal North." *Journal of Geotechnical and Geoenvironmental Engineering*, **134(5)**, 657-667.
102. Seddon, C. M., Moatamedi, M. (2006). "Review of water entry with applications to aerospace structures." *International Journal of Impact Engineering*, **32**, 1,045-1,067. July.
103. Singer, J., Arbocz, J., and Tanchum, W. (1998). *Buckling experiments: Experimental methods in buckling of thin-walled structures. Vol. 1 – Basic concepts, columns, beams, and plates*. John Wiley and Sons, Inc., New York.
104. Singer, J., Arbocz, J., and Tanchum, W. (1998). *Buckling experiments: Experimental methods in buckling of thin-walled structures. Vol. 2 – Shells, built-up structures and additional topics*. John Wiley and Sons, Inc., New York.
105. Srivastava, M. S. (2002). *Methods of multivariate statistics*. John Wiley & Sons, Inc., New York.
106. Stewart, J. R., Gullerud, A. S., and Heinstein, M. W. (2006). "Solution verification for explicit transient dynamics problems in the presence of hourglass and contact forces." *Computer methods in applied mechanics and engineering*, **195**, 1,499-1,516. February.

107. Szucs, E. (1980). *Similitude and Modeling*. Elsevier Scientific Publishing Co., New York.
108. Stetter, H. J. (1973). "Analysis of discretization methods for ordinary differential equations." *Springer Tracts in Natural Philosophy*. Springer-Verlag. Berlin.
109. Thacker, B. H., and Huyse, L. J. (2002). "Role of non-determinism in validation of computational Mechanics Models." *Proceedings of the Fifth World Congress on Computational Mechanics (WCCM V)*, Vienna, Austria, July.
110. Timoshenko, S. (1953). *History of strength of materials*. McGraw-Hill Book Company, New York/London, 156-162.
111. Ueda, K., and Umeda, A. (1997). "Evaluation of frequency response of strain gauges using impact." *Proceedings of 14th IMEKO World Congress*. J Haltunen (ed.). Finnish Society of Automation, **14**, 104-109. June.
112. Ugural, A. C., and Fenster, S. K. (1995). *Advanced strength and applied elasticity*. Third Edition. Prentice Hall PTR, NJ.
113. United Technologies USBI. (1989). *Solid socket booster systems data book for space shuttle solid rocket booster assembly project, Volume I*. Prepared for National Aeronautics and Space Administration, Marshall Space Flight Center, AL.
114. von Karmen, T. (1929). "The impact on seaplane floats during landing." TN 321, NACA.
115. Wagner, H. (1932). "Über Stoß- und Gleitvorgänge an der Oberfläche von Flüssigkeiten." *Zeitschrift fuer Angewandte Mathematik und Mechanik*, **12**, 192-215.
116. Wei, Z., Yu, J., and Batra, R. (2005). "Dynamic buckling of thin cylindrical shells under axial impact." *International Journal of Impact Engineering*, **32**, 575-592.
117. Wu, G. X., Sun, H., and He, Y. S. (2004). "Numerical simulation and experimental study of water entry of a wedge in free fall motion." *Journal of Fluids and Structures*, **19**, 277-289.
118. Yaffe, R., Abramovich, H. (2003). "Dynamic buckling of cylindrical stringer stiffened shells." *Computers and Structures*, **81**, 1,031-1,039.
119. Yettou, E.-M., Desrochers, A., and Champoux, Y. "Experimental study on the water impact of a symmetrical edge." *Fluid Dynamics Research*, **38**, 47-66.
120. Zanuttigh, B., and Lamberti, A. (2006). "Experimental analysis and numerical simulations of waves and current flows around low-crested rubble-mound structures." *ASCE Journal of Waterway, Port, Coastal, and Ocean Engineering*, **132(1)**, 10-27.

121. Zhang, R., and Mahadevan, S. "Bayesian methodology for reliability model acceptance." *Reliability Engineering & System Safety*, **80(1)**, 95-103.
122. Zhao, R. and Faltinsen, O. (1993). "Water Entry of Two-Dimensional Bodies." *Journal of Fluid Mechanics*, **246**, 593-612.